Solid-Solid Phase Transitions in Iron Systems

Vom Fachbereich Maschinenbau und Verfahrenstechnik

der Technischen Universität Kaiserslautern zur

Verleihung des akademischen Grades

Doktor-Ingenieur (Dr.-Ing.)

genehmigte Dissertation

von

Diplom Ingenieur

Binjun Wang

aus Shanghai, v.R. China

Datum der mündlichen Prüfung: 30.01.2014

Promotionskommission:

Vorsitzender: Prof. Dr.-Ing. Ralf Müller

1. Berichterstatter: Prof. Dr.-Ing. Eberhard Kerscher

2. Berichterstatter: Prof. Dr. rer. nat. Herbert M. Urbassek

Kaiserslautern, Februar 2014

D 386

Declaration of academic honesty

I declare that I have
- authored this thesis independently, that I have not used other than the declared sources or resources, and that I have explicitly marked all material which has been quoted either literally or by content from the used sources.
- not submitted this thesis or one part thereof for evaluation to another scientific or national examination authority.
- not submitted the same or another dissertation to another department or another university as a doctoral thesis.

_____ _____

date signature

Ich erkläre an Eides statt, dass ich
- die vorliegende Arbeit selbstständig verfasst, andere als die angegebenen Quellen oder Hilfsmittel nicht benutzt, und die den benutzten Quellen wörtlich und inhaltlich entnommenen Stellen als solche kenntlich gemacht habe.
- die Dissertation oder Teils hiervon noch nicht als Prüfungsarbeit für eine staatliche oder andere wissenschaftliche Prüfung eingereicht habe.
- die gleiche oder andere Abhandlung bei einem anderen Fachbereich oder einer anderen Universität als Dissertation nicht eingereicht habe.

_____ _____

Datum Unterschrift

Acknowledgements

I would like to express my gratitude to my principal supervisor, Prof. Dr. Eberhard Kerscher for his good advice and kind estimate of my thesis.

I cannot find words to express my gratitude to my second supervisor, Prof. Dr. Herbert M. Urbassek, who allowed me to work in his research group. I also would like to thank him for the valuable guidance and advice on both academic and personal matters. This thesis would not have been possible without the support of him. It is really my lucky to have him as my “Doktorvater”.

I would like to thank Prof. Dr. Ralf Müller for his kind support as the chairman of my Promotions Committee.

I would like to thank my past and present colleagues, Sineng Sun, Yudi Rosandi, Christian Anders, Christian Mücksch, Yaroslav Cherednikov, Yu Gao, Riser Fahdiran, Maureen Linggarsari Nietiadi, Emilia Sak-Saracino, Nina Gunkelmann, Gerolf Ziegenhain, Christian Ringl and Luis Sandoval, who made these past four years in Kaiserslautern more pleasant. I am specially thankful to Dr. Yudi Rosandi, Dipl. Christian Mücksch and Dr. Sinneng Sun for their excellent technical support. Many thanks to Mrs Esther Paul-Greß, who helped me to deal with the organizational affairs.

I would like to thank my mother Ruqin Shang for her love, trust and encouragement for these years.

Thanks to my wife Yingxun Min for her love and huge support in the daily life. Many many thanks for the accompany in my darkest time in the year 2007.

Thanks to my daughter Yirui Erika Wang, who was born in the year 2011. Your presence brings me a lot of happiness and force.

The allowance of the Deutsche Forschungsgemeinschaft (DFG)-Graduiertenkolleg 814, Fachbereich Physik TU Kaiserslautern and Sonderforschungsbereich (SFB) 926 is gratefully acknowledged.

Abstract

In the present work, the phase transitions in different Fe/FeC systems were studied by using the molecular dynamics simulation and the Meyer-Entel interaction potential (in Chapter 8 and 9 also the Johnson potential for describing the Fe-C interaction). In the first chapter, the motivation and the construction of this work were explained. Chapter 2 and 3, the fundamentals of material science and molecular dynamics simulation were presented, respectively. In the main part of this work, different Fe systems under different conditions were investigated to study the behavior of the phase transition.

The energetics and dynamics of the phase transition in an Fe bicrystal containing a bcc/fcc interface were investigated in Chapter 4. The interface obeys the Nishiyama-Wassermann (N-W) orientation relationship. The emergence of threading dislocations, which grow into the bcc phase, was observed after relaxation at the phase boundary. The spontaneous temperature-induced phase transitions in the Fe bicrystal were investigated at temperatures of 100 K and 1300 K. Both homogeneous and heterogeneous transformations could be observed at low temperature. In this case, the propagation velocity of the phase boundary amounts to 24 m/s; at high temperature, it is one order of magnitude larger. The dynamics of the phase transition and of the propagating interface were discussed and compared to the previous results.

In Chapter 5, the phase transitions were studied in the same system that had been used in Chapter 4 under applied shear strains. The results show a strong temperature dependence. At low temperatures, both homogeneous and heterogeneous nucleations of the bcc phase were observed. At high temperatures, but still below the equilibrium transition temperature, the bcc phase only grows by interface motion. Above the transition temperature, the bcc phase transforms homogeneously to the close-packed (cp) phase. In all cases studied, the unstrained system is stable and does not transform.

Chapter 6 focused on the dependence of the phase growth dynamics on the available volume by using biphasic crystal systems containing fcc/bcc interfaces with different sizes. The results show that in larger volumes, homogeneous phase nucleation is favored at the cost of heterogeneous growth. In addition, the influence of the interface geometry on the phase transition behavior was studied. While the interfaces roughen in both cases,

a Kurdjumov-Sachs (K-S) interface geometry leads to a dendritic interface growth, while the N-W interface geometry remains globally planar.

The response of thin Fe films to tensile in-plane strain was studied in Chapter 7. For the four surface orientations studied, the following sequence of transform was found in the strained films: (i) a bcc $\rightarrow$ hcp transition; (ii) the partial back transition to the bcc phase; (iii) grain refinement; (iv) finally, intergranular fracture occurs. The bcc $\rightarrow$ hcp transformations follow the Burgers path in all cases. Film thickness does not play a major role in the sequence of film transformations occurring. However, thinner films allow for a faster nucleation of the new phase.

Chapter 8 treated the austenitic and the martensitic solid-solid phase transition in Fe-C bulk system. Random alloys with C contents up to 1 at% were subjected to a heating/cooling cycle. The martensite and austenite phase transition temperatures could be determined from the hysteresis of the system volume with the temperature. Both the martensite temperature and austenite temperature decrease with increasing C content, as in experiment. The influence of the C atom position on the phase transition and the pathways of the transition were analyzed. The transformed austenite phase shows strong twinning.

In Chapter 9, the austenitic and martensitic phase transition was studied in Fe-C nanowires with C contents up to 1.2 at%. The transformation temperatures decrease with increasing C content. The martensite temperature decreases with increasing wire diameter towards the bulk value. During the transformation, the bcc and fcc phases obey the K-S orientation relationship. For ultrathin wires (diameter $D \leq 2.8$ nm), wire buckling as well as shape-memory effects could be observed. Under axial tensile stress, the martensitic transformation is partially suppressed, leading to strong plastic deformation. Under the highest loads, the austenite transforms only partially back while the crystalline phases in the wire reorient; this reorientation gives the multiphasic mixture a high tensile strength.

Übersicht

In der vorliegenden Arbeit sind die Phasenumwandlungen in verschiedenen Fe/FeC Systemen mit Hilfe von Molekular Dynamik Simulationen und dem Meyer-Entel Potential (in Kapital 8 und 9 auch das Johnson Potential für Fe-C Wechselwirkung) untersucht worden. Im ersten Kapital sind die Motivation und die Konstruktion dieser Arbeit erklärt worden. In Kapital 2 und 3 sind die Grundlagen von Werkstoffwissenschaft beziehungsweise Molekular Dynamik Simulation vorgestellt worden. Im Hauptteil dieser Arbeit sind verschiedene Fe Systeme unter verschiedenen Bedingungen eingeführt worden, um das Verhalten der Phasenumwandlung zu studieren.

In Kapital 4 wurden die Energetik und Dynamik der Phasenumwandlung in einem Fe Bikristall untersucht. Das System beinhaltet eine bcc/fcc Phasengrenze in Nishiyama-Wassermann (N-W) Geometrie. Bildung von Fehlpassungsversetzungen, die in die bcc-Phase hineinwachsen, wurden beobachtet nach der Relaxation an der Phasengrenzen. Bei Temperaturen von 100 K und 1300 K sind die Temperatur-induzierten Phasenumwandlungen untersucht worden. Beide homogene und heterogene Phasenumwandlungen wurden beobachtet bei niedrigen Temperatur. In diesem Fall beträgt die Grenzflächengeschwindigkeit 24 m/s; bei hohen Temperatur ist sie um eine Ordnung höher. Die Dynamik der Phasenumwandlung und der bewegenden Grenzfläche wurden diskutiert und verglichen mit den vorherigen Ergebnissen.

In Kapital 5 sind die Phasenumwandlungen in zweiphasischen System unter angelegter Scherspannung untersucht worden. Die Ergebnisse zeigen eine starke Temperaturabhängigkeit. Bei niedrigen Temperaturen konnten homogene und heterogene Keimbildungen beobachtet werden. Bei hohen Temperaturen, die noch unter der Umwandlungstemperatur liegen, wächst die bcc Phase nur durch Grenzflächenbewegung. Oberhalb der Umwandlungstemperatur transformiert sich die bcc Phase homogen zur dichtgepackten (cp) Phase. In allen untersuchten Fällen ist das System stabil und nicht transformiert ohne Scherung.

Kapital 6 konzentrierte sich auf die Abhängigkeit der Phasenwachstumsdynamik vom verfügbaren Volumen. Zweiphasische kristalline Systeme mit bcc/fcc Grenzflächen in verschiedenen Systemgrößen sind eingeführt worden für die Simulationen. Die Ergebnisse zeigen, dass im größerem Volumen homogene Keimbildung auf Kosten von hetero-

genem Wachstum begünstigt ist. Außerdem wurde der Einfluss der Grenzflächengeometrie auf das Umwandlungsverhalten untersucht. In beiden Fällen werden die Phasengrenzen grob während des Wachstums; eine Kurdjumov-Sachs Grenzflächengeometrie führt zu einem dendritischen Wachstum, während die N-W Grenzflächengeometrie global eben bleibt.

Die Reaktion der Fe Dünnschichten auf die Zugspannung ist in Kapital 7 untersucht worden. Für die vier untersuchten Oberflächenorientierungen wurde die folgende Reihenfolge der Umwandlungen gefunden: (i) ein bcc $\rightarrow$ hcp Übergang; (ii) die teilweise Rückwandlung in die bcc Phase; (iii) Kornmodifikation; (iv) schließlich findet interkristalliner Bruch statt. In allen untersuchten Fällen gehorcht die Umwandlung dem Burgers Mechanismus. Schichtdicke spielt keine wichtige Rolle in der Reihenfolge der Umwandlungsvorgänge. Allerdings ermöglichen dünnere Schichten eine schnellere Keimbildung der neuen Phase.

Kapital 8 betrachtete die austenitische und martensitische Phasenumwandlung in Fe-C Bulk-System. Ein Aufheizungs/Abkühlungszyklus wurde auf zufällige Legierungen mit C-Gehalt bis zu 1 at% angewendet. Die Martensit- und Austenit Temperaturen konnten aus der Hysterese des Systemvolumens bei Temperaturänderung bestimmt werden. In Übereinstimmung mit dem experimentellen Befund nehmen die Martensit- und Austenit-Temperatur mit zunehmendem C-Gehalt ab. Der Einfluss der Position von C Atomen auf die Phasenumwandlung und den Umwandlungspfad wurden analysiert. Die umgewandelte Austenite Phase zeigt starke Zwillingsstruktur.

In Kapital 9 wurde die austenitische und martensitische Umwandlung in Fe-C Nanodrähten mit C-Gehalt bis zu 1.2 at% untersucht. Die Umwandlungstemperaturen nehmen mit zunehmendem C-Gehalt ab. Mit zunehmendem Drahtdurchmesser fällt die Martensit-Temperatur zu ihrem Bulkwert (Abnahme). Während der Umwandlung folgen die fcc und bcc Phasen der K-S Orientierungsbeziehung. Bei ultradünnen Drähten (Durchmesser $\leq$ 2.8 nm) konnten Drahtverformung und Formgedächtnis-Effekt beobachtet werden. Unter axialer Zugspannung ist die martensitische Umwandlung teilweise unterdrückt. Dies führt zu starker plastischer Formänderung. Unter den höchsten Belastungen transformiert sich die austenitische Phase nur zum Teil zurück, während sich die kristallinen Phasen im Draht umorientieren und der mehrphasigen Mischung eine hohe Zugfestigkeit geben.

Contents

List of Figures

List of Tables

Chapter 1

Introduction

The mechanism and kinetics of the α-γ phase transition in iron (Fe) systems, i.e., the transition between the low-temperature body-centered cubic (bcc) and the high-temperature face-centered cubic (fcc) phase have been studied for many years [1, 2, 3]. This phase transition is relevant for controlling the microstructure of steel and thus plays a central role in materials properties such as the yield strength and hardness. On the other hand, interest in nanoscale and surface-dominated systems gives a new impetus in studying phase transitions in such systems [4, 5]. Their small size causes an increased fraction of surface atoms as compared to bulk systems; nanoscale systems may exhibit drastically changed properties, for instance with respect to their mechanical and magnetic behavior [6, 7, 8, 9]. Thus, the most atomistic simulation studies are devoted to pure Fe, and investigated the phase transition in the bulk [3, 10, 11], in thin films [12, 13, 14, 15] or in nanoclusters and nanowires [16, 17, 18, 19]. Studies of iron alloys concentrate on metallic alloying elements like Cu or Ni [20, 21, 22].

Among the iron-based alloys, the Fe-C system is one of the special importance as it forms the basis of steels. Many important issues have been investigated for this system, such as the position of the C atoms in Fe lattice [23, 24, 25] and the diffusivity of C atoms [26, 27, 28, 29] or elastic properties [24, 28, 30]. Up to now, however, few if any atomistic studies have been published on the solid-solid phase transformations of the Fe-C system.

In this work, the solid-solid phase transitions in different Fe systems are studied by means of classical molecular dynamics simulations. The interatomic potential employed, Meyer-Entel [31], has been shown to be capable of describing both the $\alpha \rightarrow \gamma$ and $\gamma \rightarrow \alpha$ phase transition. The work is organized as following:

In Chapter 2, fundamentals of material science are presented. The basic properties of Fe, the phase transition in Fe systems and the effect of C atoms in Fe lattice are described in detail.

The molecular dynamics method is presented in Chapter 3. The basic ideas of this method and the algorithms are explained. In addition, the detectors and the interatomic potentials, which are used for calculations in this work are introduced.

A biphasic pure Fe system, which contains a bcc/fcc interface with Nishiyama-Wassermann (N-W) [32, 33] relationship is introduced in Chapter 4. The properties of the constructed interface are analyzed. Two temperatures (100 K and 1300 K) are investigated to study both austenite and martensite phase transitions. The propagation velocities of the phase boundary at both low and high temperatures are calculated.

Chapter 5 and 6 are two extensions of Chapter 4. In Chapter 5, shear strains, whose direction is chosen such as to favor the $\alpha \rightarrow \gamma$ transition are applied to the biphasic system. The phase transitions in temperature range from 300 to 700 K, in which the systems are stable when no strain is applied, are studied. Based on the results of Chapter 4 and 5, the dependence of the phase growth dynamics on the available volume is treated in Chapter 6. In addition, the influence of the interface geometry on the phase transition behavior is studied in the same chapter; a biphasic pure Fe system containing fcc/bcc interface with the Kurdjumov-Sachs (K-S) [34] orientation relationship is introduced and the results are compared with the N-W relationship.

In Chapter 7, the response of thin Fe films (thickness < 10 nm) to tensile in-plane strain is represented. The $\alpha \rightarrow \epsilon$ phase transitions in the strained films are studied in dependency on the film thickness and surface orientation. Beyond that, the kinetics and the pathway of the phase transitions are analyzed.

In Chapter 8 and 9, the phase transitions in Fe-C systems are treated. The C content dependency on the transition temperature is analyzed and compared with the experimental and free energy calculation results. Bulk systems and nanowire systems are introduced in Chapter 8 and 9, respectively. Beside that, the heating/cooling rate dependence on the phase transition is studied in the bulk system. In the nanowire system, the wire diameter and axial load dependency are investigated. For both systems, the pathway of the transformation is analyzed.

A summary is given in the last chapter.

Chapter 4-9 correspond to the publication (1)-(6) of the author, see publication list.

Chapter 2

General of phase transformation in Fe system

2.1 Metal iron

Iron (Fe) is one of the most important materials in the world. It is the fourth most common element in the Earths crust, and has been used since ancient times for about 5000 years. Pure iron is a silver-colored and odorless metal that conducts heat and electricity well. In additional, pure iron is very soft (Mohs hardness 4). Due to this reason, pure iron is rarely used in industry. Instead, the mechanical properties are dramatically improved, for example, increase in hardness and tensile strength, when additives, essentially carbon, are added. Other additives can be nickel, chromium, molybdenum, boron, etc. Such iron alloy is called steel, which is used widely in utensils, architectures and in industrial applications such as automotive.

There are four known allotropes of solid iron. Fig. 2.1 shows the phase diagram of pure iron. At room temperature and atmospheric pressure, α-iron (ferrite), which has a body-centered cubic (bcc) crystal structure is stable. When the temperature is increased, α-iron changes its crystal structure to a face-centered cubic (fcc) structure at 1184 K. In this form it is called γ-iron (austenite). Under non-equilibrium conditions, e.g., rapid change of temperature, the phase transition does not take place at the equilibrium temperature; By heating it takes place above the transition temperature (overheating) and by cooling under it (undercooling). This phenomenon is called thermal hysteresis. Thus, the higher the heating/cooling rate, the bigger is the variance. With further increase of temperature, γ-iron transforms back to the bcc structure, called δ-iron, at 1665 K before it melts at 1811 K. At pressures above 13 GPA, α-iron changes into a hexagonal close-packed (hcp) structure, which is known as ϵ -iron. In additional, at 1043 K (curie point), iron transforms from the ferromagnetic (spin ordered) state to the paramagnetic (spin disordered) state.

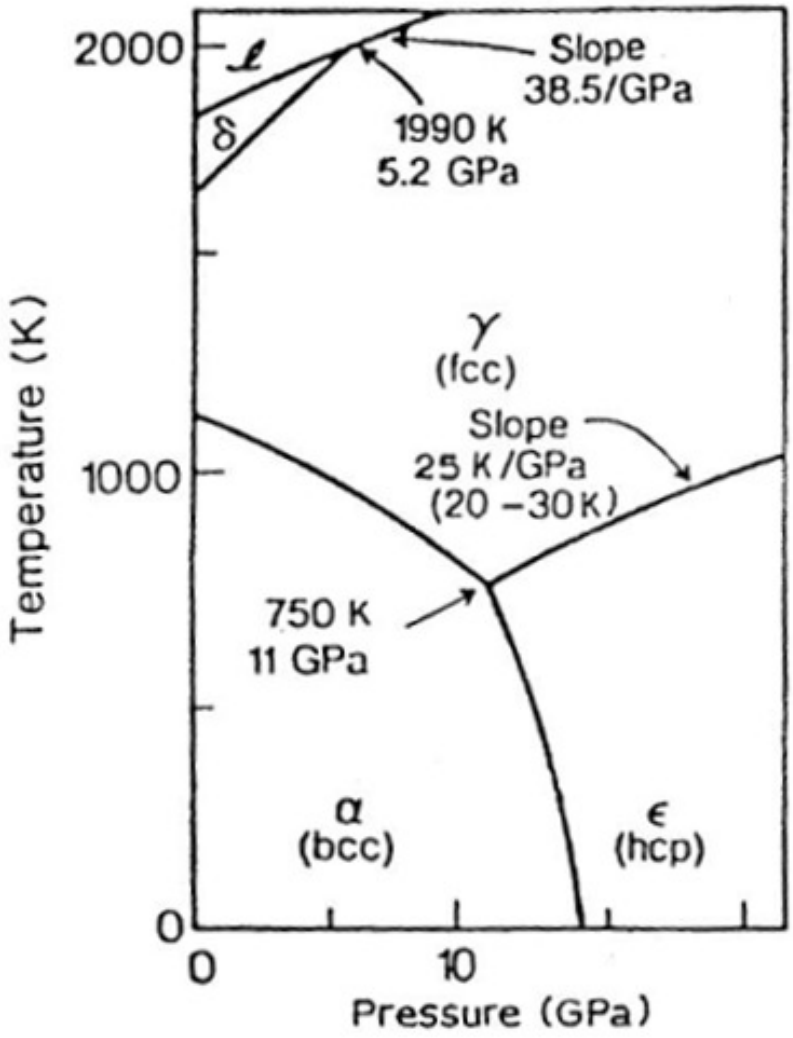

Figure 2.1: Phase diagram for pure iron, figure taken from Ref [35]

During the curie transition there is no change in the crystalline structure, but a change in domain structure.

Richness in transformation behavior of iron has great valuable significance. It will be introduced in next section.

2.2 Phase transition

A phase transition is defined as the transformation of thermodynamic system from one phase (or more phases) to another. When parent phase and product phase keep their solid states, it is called solid-solid phase transition. A change in external conditions, such as temperature, pressure and magnetic or electric fields may induce a phase transition. The

value of the temperature, pressure or other physical quantity at which parent phase(s) and new phase(s) coexist is called a transition point. Phase transitions are generally classified according to the Ehrenfest classification (1933) based on the singular behavior of the derivatives of free energy. If some of the first derivatives are discontinuous, the phase transition is of first order. First order phase transitions include the various solid/liquid/gas transitions and certain structural transformations in solids, e.g., the formation of martensite in iron. If all the first derivatives are continuous, but the second order derivatives are discontinuous, the phase transition is classified to the second order. These include the ferromagnetic phase transition in materials such as iron. In the context of this work, the solid-solid phase transitions in iron systems are very important because they are relevant for controlling the microstrucutre of steel and thus play a central role in materials properties such as the yield strength and hardness.

2.2.1 Phase boundary

A phase boundary is an interface between two or more separate phases, which may have different composition, crystal structure and lattice constant. Depending on the atomic structure, phase boundaries can be divided into three types, see Fig. 2.2.

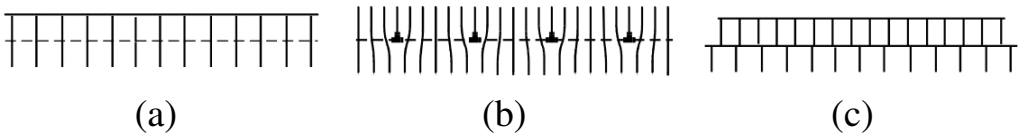

Figure 2.2: Three types of phase boundaries (a) coherent (b) semicoherent (c) incoherent, figure taken from Ref. [36]

When two crystallites match perfectly, or almost perfectly, at the interface plane, it is referred as to a coherent phase boundary. The small lattice misfit is accommodated by elastic strain. In this case the atomic positions on either side of the boundary are correlated, see Fig. 2.2(a). When the misfit at the interface plane becomes bigger, the lattice mismatch is accommodated by periodic array of misfit dislocations; a semicoherent phase boundary is maintained, see Fig. 2.2(b). Incoherent phase boundary can be formed only by very different structure of the two phases or large lattice mismatch, see Fig. 2.2(c). This structure is very similar to random large-angle grain boundary. Among the three types of phase boundaries, the incoherent phase boundary has the highest interface energy, which involves both chemical and structural contributions (also for semicoherent phase boundary), while the coherent phase boundary has the lowest. Typical interface energy values for the three types of phase boundaries are listed in Table 2.1.

Interface	γ (mJ/m^2)
Coherent	5-200
Semicoherent	200-800
Incoherent	800-2500

Table 2.1: Ranges of solid-solid interphase boundary energies γ for three types of phase boundaries, taken from Ref. [37]

2.2.2 Martensitic transition

Martensite is named after the German metallurgist Adolf Martens, who found firstly this very hard but brittle form of steel crystalline structure. Depending on the C content in steel, the martensite has appearance of lath (C content less than 0.6 %) or plate (C content greater than 1 %). Martensitic phase transition is a first order solid-solid phase transition, by which the high-temperature austenitic phase transforms to the low-temperature martensitic phase. This phase transition is induced by rapid cooling (quenching) of the austenitic phase (can be also induced by deformation or ion bombardment). The carbon atoms have no time to diffuse at such a high cooling rate to form the equilibrium Fe_3C (cementite) phase. For this reason, martensite is metastable and not shown in the equilibrium phase diagram of the Fe-C alloy. The change of crystal structure takes place by small cooperative movements of the atoms (shear distortion of the lattice structure), keeping the same chemical composition and atomic order of the austenitic phase. The interface between the parent phase (austenite) and the product phase (martensite) is referred as to the habit plane (lattice invariant plane), which does not rotate or deform during the course of the transformation. The martensitic phase transition proceeds by the movement of the habit plane. In order to keep the habit plane invariant, an additional lattice shear, which occurs by slip or by twinning of the lattice, is necessary. Note the two mechanisms lead no or only very small volume change during the phase transition.

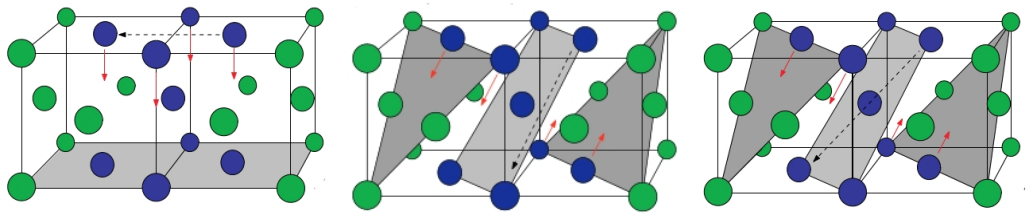

Figure 2.3: Orientation relationship between the γ and α phases for the Bain (a), the N-W (b) and the K-S (c) paths. The blue atoms indicate a bcc unit cell. The red arrows indicate part of the motion initiating the transformation. The dashed arrows indicate the invariant direction which is shared by the γ and α phase. Figures taken from Ref. [38].

As mentioned in Section 2.1, the lattice structure changes from fcc (γ phase) to bcc (α phase) by decreasing the temperature in pure iron. In Fe-C systems, the crystal lattice is tetragonal distorted because of the presence of C atoms. Note that the C atoms are located in the octahedral sites (edge and face centers of the unit cell) in bcc lattice. For this reason, the martensite has a body-centered tetragonal (bct) structure. Bain [39] suggested a possible path of the martensitic transition in 1924. In his model, the bcc structure can be obtained from the fcc structure by a simple mechanical process consisting of compression in one direction and expansion in remaining two directions, Fig. 2.3(a). Although the Bain model has been widely accepted, it has several major drawbacks: (i) The experimentally observed orientation relationship between the fcc and the bcc phase is often not in agreement with this path; (ii) shear, which is a characteristic feature of the martensitic phase transformation, is not involved in the Bain model; (iii) it cannot explain some phenomena such as the existence of conjugate habit planes in the martensitic phase transformation. Nishiyama [32] and Wassermann [33], Kurdjumov and Sachs [34] proposed new orientation relationships on the base of Bain model. Fig. 2.3 displays the orientation relationship between the γ and α phases for the Bain, the Nishiyama-Wassermann (N-W) and Kurdjumov-Sachs (K-S) paths. The N-W orientation relations can be written as

$$(111)_{\mathrm{fcc}} \parallel (011)_{\mathrm{bcc}} \qquad \text{and} \qquad [11\bar{2}]_{\mathrm{fcc}} \parallel [01\bar{1}]_{\mathrm{bcc}},$$

and the K-S orientation relations are described by

$$(111)_{\mathrm{fcc}} \parallel (011)_{\mathrm{bcc}} \qquad \text{and} \qquad [10\bar{1}]_{\mathrm{fcc}} \parallel [11\bar{1}]_{\mathrm{bcc}}.$$

The K-S relationship indicates that the close-packed planes (directions) of α and γ phases are parallel each other. When the α phase deviates slightly from having close-packed parallel directions [rotation along the $(011)_{\mathrm{bcc}}$ axis of 5.26°], the N-W path is obtained. Low-carbon steels transform according to the K-S relationship, while high-carbon steels obey the N-W relationship [40]. Note about 90 % of all $\alpha \leftrightarrow \gamma$ phase transitions obey either a N-W or a K-S relationship [41].

Chapter 3

Molecular dynamics method

3.1 General of molecular dynamics

Molecular dynamics (MD) is a computer simulation where the trajectories of a set of interacting molecules/atoms is followed by numerical integration of the Newton's equation of motion. This method is widely used in a large variety of research areas. In material science, specially in crystal systems, MD is used to examine the dynamics of atomic phenomena that cannot be observed directly, such as motion of the atoms during a phase transition and thin film growth. It is also used for exploring the structure of nanosystems, such as nanowire and thin film, that have not or cannot yet be created in experiment. In addition, this method makes it possible to study the material behavior under extreme conditions, which is hard to reach in reality, such as shock wave and extreme high heating/cooling rate. Figure 3.1 displaces a simplified description of the molecular dynamics simulation algorithm.

For each atom i in a system constituted by N atoms, it holds the Newton's law

$$m\ddot{r}_i = F_i \tag{3.1}$$

where m is the atom mass, r_i its position and F_i the force acting upon it due to the interaction with other atoms. In another way, the force F_i can be also written as the first derivative of the potential energy $E_{pot}(\{x_1, ..., x_N\})$ with respect to the atom position r_i

$$F_i = -\frac{\partial E_{pot}}{\partial x_i} \tag{3.2}$$

where the potential energy $E_{pot}(\{x_1, ..., x_N\})$ is composed of the interactions of atom i with each other atom j (equation 3.3).

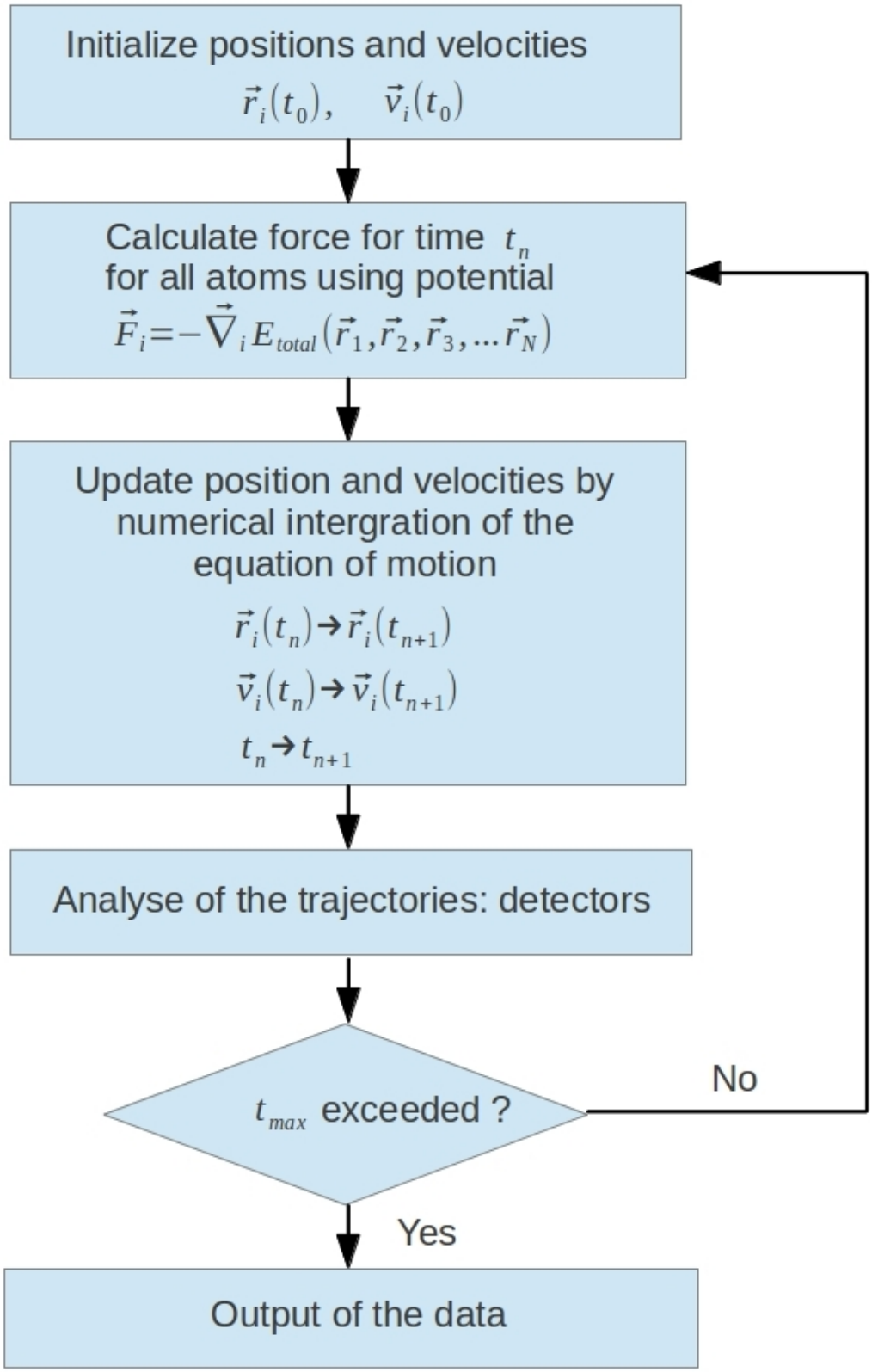

Figure 3.1: Simplified description of the molecular dynamics simulation algorithm

$$E_{pot}(\{x_1, ..., x_N\}) = \sum_{ij} \phi(x_{ij}) \tag{3.3}$$

Knowing of the initial positions and velocities of the atoms and interaction between them, one can compute the position and the velocity of each atom for each defined time step. An essential problem in molecular dynamics is the time integration. An algorithm, which is used to solve an ordinary differential equation, is called integrator. In the numerical time integration, the equations of motion are only evaluated at discrete time points, the time step Δt being the distance between consecutive time points. Knowing the positions and velocities at time t, the integrator gives the same quantities at later time $t + \Delta t$. By iterating the procedure, the time evolution of the system can be followed for long times. The Verlet algorithm [42], which is probably the most commonly used time algorithm in MD, is used for calculations in this study. More detailed informations on time integration algorithms are described in Ref. [43, 44].

In this chapter, the basic concepts of molecular dynamics for understanding of the calculations in this work will be presented.

3.2 Boundary conditions

It is very often that simulated system has a high particle number. But only a small part of the particles can be taken into account in the simulation. In order to set the simulation conditions as close as possible to experiment, choice of the boundary conditions is very important.

3.2.1 Periodic boundary condition

Molecular dynamics is commonly applied to small systems. A large fraction of the atoms is on the surface or interact with the surface atoms. Unless the behavior near/at the surfaces are of interest, this situation is not realistic. A solution to this problem is to use periodic boundary conditions (PBC). In this case, the simulation volume is replicated throughout the space to form an infinite lattice by rigid translation in all the three cartesian directions, Fig. 3.2.

When a particle passes through one face of the original box (blue box in Fig. 3.2), it reappears on the opposite face with the same velocity. Thus the total number of the particles keeps constant in the original box. Note that each particle in the original box is interacting not only with the particles in its own box, but also with their images in the adjacent boxes. The periodic boundary conditions are useful to simulate a part of bulk system without surface effect.

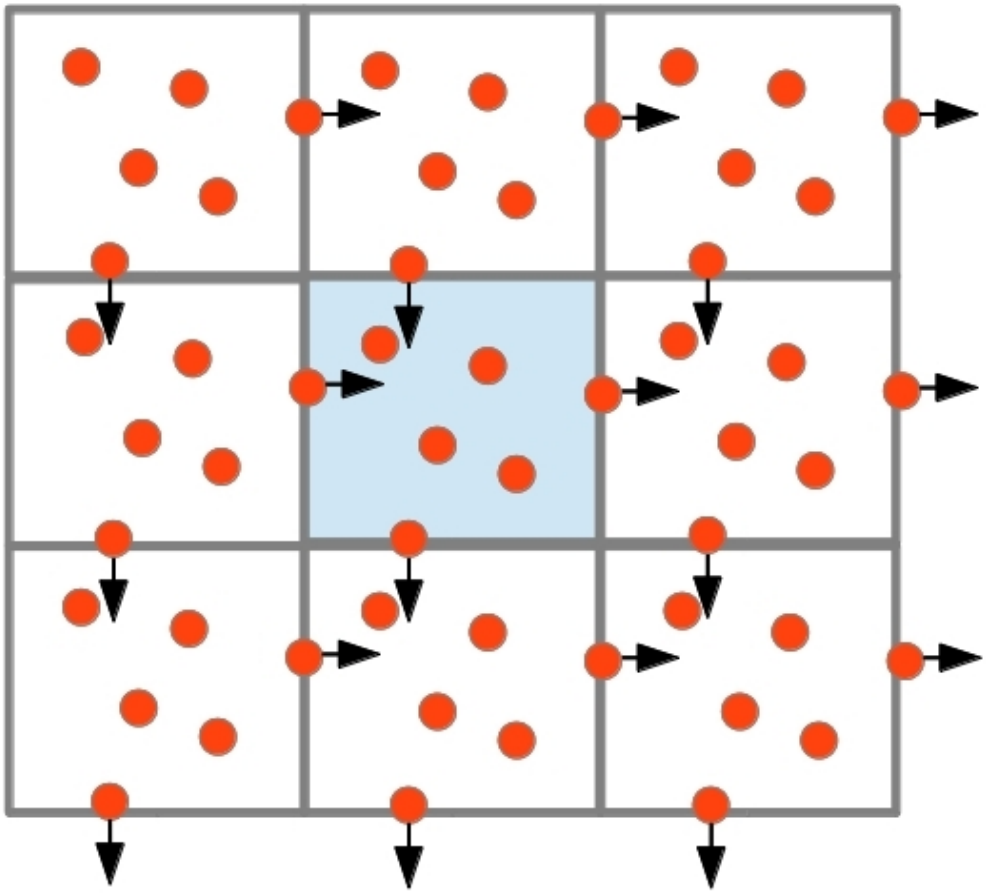

Figure 3.2: Illustration of periodic boundary conditions in 2D

3.2.2 Alternative boundary conditions

As opposed of periodic boundary conditions, free and rigid boundaries are used sometimes. In the case of free boundaries, the conditions of simulation is accordance with a cluster in vacuum. Free boundary conditions are appropriate for simulating systems with high fraction of free surfaces, such as nanowire and thin film system. For rigid boundary conditions, the surface particles are fixed. In the most case, the rigid boundaries are unphysical and rarely used.

3.3 Energy minimization

Energy minimization methods are used to find a minimum on the potential energy surface, i.e., the equilibrium configuration of the system. The method of steepest descents is a first order optimization algorithm. Start from a randomly selected point, the first search direction is opposite to the direction in which the gradient is largest. This search continues until the potential energy along the gradient rises. Once the potential energy along the

gradient rises, i.e., minimum finding in this direction, the search direction changes to the steepest remaining direction. The next local minimum is found by such a path. The search stops by reaching a minimum in all directions to within a sufficient tolerance, see Fig. 3.3. The conjugate gradient method is a variation of the steepest descents method. The first portion of the search is identical to the steepest descent method, but for the next search the negative gradient is not chosen any more, but a so called conjugate gradient h_k. The current iteration and next iteration are interconnected with a matrix A, which satisfies $h_i^T A h_k = 0$ for $i \neq k$. In this work, the method of conjugate gradient is used, because it is more efficient than the method of steepest descents, specially in the last stage of the simulation steps.

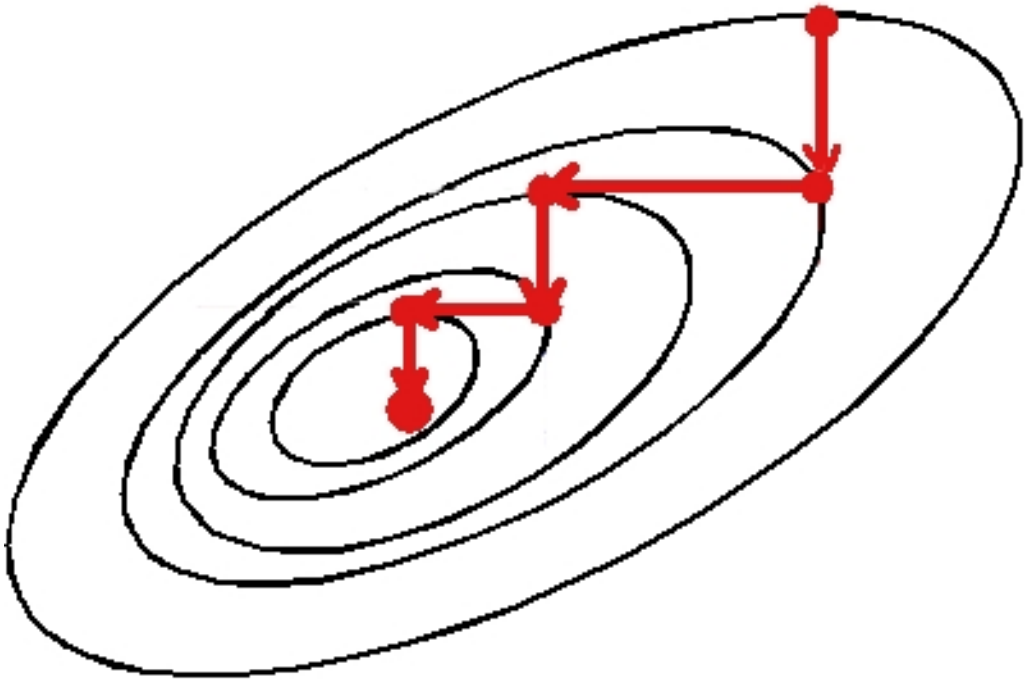

Figure 3.3: Illustration of the steepest descent method.

3.4 Ensembles

In language of statistical physics, an ensemble is defined as a collection of identically prepared microstates of system of particles in thermodynamic equilibrium. If the total number and the volume are kept constant and the system has no exchange of energy with the environment, then the MD simulations are said to be performed in the microcanonical (NVE) ensemble. However, temperature is often kept constant in experiment. This

requires MD to reproduce other ensembles, such as canonical NVT ensemble, in which the particle number, volume and temperature are fixed.

Another important ensemble in the range of this work is the isothermal-isobaric (NpT) ensemble, in which particle number, temperature and pressure are conserved. The volume is increased or decreased to adjust the proper pressure by rescaling the atomic coordinates. This ensemble corresponds most closely to experiment conditions with control of pressure and temperature simultaneously.

There are different kinds of thermostats/barostats to control the temperature/pressure. The Berendsen [45] thermostat rescales the velocities of the particles, so that the aim temperature is reached in a certain time. The Andersen thermostat [46] couples the system to a imaginary heat bath with the desired temperature via stochastic impulsive forces that act occasionally on randomly selected particles. The Nosé-Hoover thermostat, which was originally introduced by Nosé [47] and developed further by Hoover [48], is the most commonly used method for the NpT-implementation. The authors considered the heat bath as an integral part of the system by adding an artificial variable associated with an artificial mass. This variable can be considered as "fiction" in the system. Many of the methods used for the pressure control are analogous to the temperature control, e.g., the Berendsen barostat is very similar to the Berendsen thermostat; an additional term is added to the equations of motion that effects a pressure change. Details for temperature/pressure controls see Ref. [43, 44].

3.5 Detectors

Algorithms, which are used for determination of a certain measurand, e.g., temperature or pressure, from the trajectories of particles, are called detectors. More informations on standard temperature/pressure detectors in MD see Ref. [44]. In this section, two detectors for atomic structure identification, which are used for the calculations in this work, will be presented.

3.5.1 Centrosymmetry parameter

Centrosymmetry parameter (CSP) is an useful measure of crystal defects, where the symmetry of the lattice is broken. This parameter is computed by using the following formula from Ref. [49]

$$CSP = \sum_{i=1}^{N/2} |r_i + r_{i+N/2}|^2 \tag{3.4}$$

where N is the number of nearest neighbors, r_i and $r_{i+N/2}$ are vectors from the central atom to a particular pair of nearest neighbors. For an atom in perfect lattice, its CSP is 0, because the r vectors cancel out each other. The values of other configurations depend on the material chosen. For example, for aluminum, CSPs are 32.8 for surface atoms, 8.2 for atoms in an intrinsic stacking fault and 2.05 for atoms in a partial dislocation (data taken from Ref. [50]). This method is almost not affected by elastic distortion of the crystal, but very sensitive to random thermal displacement of atoms. In addition, its capacity of distinguishing between defects types is rather weak.

3.5.2 Common neighbor analysis (CNA)

The common neighbor analysis (CNA) [51, 52] method assigns a structure type (fcc, bcc, hcp, etc.) to each atom. Unlike the CSP method, the CNA does not set the spatial vectors pointing from the central atom to its neighbor directly. Instead, the topology of the bonds that connect the surrounding neighbor atoms is analyzed. Firstly, if two atoms are within a specified cutoff distance r_{cut}, they are considered as nearest neighbors, or bonded. For fcc or hcp structure, r_{cut}^{fcc} must be chosen such that it lies midway between the first and second neighbor shell, one has

$$r_{cut}^{fcc} = \frac{1}{2}(\sqrt{1/2+1}+1)a_{fcc} \approx 0.8536 a_{fcc} \tag{3.5}$$

where a_{fcc} is the lattice constant for the crystal structure. For bcc structure, the cut-off distance is defined as

$$r_{cut}^{bcc} = \frac{1}{2}(1+\sqrt{2})a_{bcc} \approx 1.2076 a_{bcc} \tag{3.6}$$

where r_{cut}^{bcc} lies between the second and the third neighbor shell. In multiphasic systems, the cut-off distance cannot be chosen well defined. Several CNA-detectors with different r_{cut} should be used for determination of the corresponded phase. Recently, an adaptive version of CNA has been developed, which works without the cut-off distance [53].

Three characteristic numbers, i, j and k, are computed for each of the N neighbor bonds of the central atom: the number of common neighbor atoms of the central atom and its bonded neighbor, i; the number of bonds between these common neighbor atoms, j; and the number of bonds in the longest chain of bonds connecting the common neighbors, k. These three numbers make the discriminating between different crystal structures possible, e.g., a bcc coordinated atom has 8 bonds of (666) type and six bonds of (444) type. CNA signatures of bcc, fcc and hcp crystal structures are listed in Tab. 3.1 and Fig. 3.4 shows the difference between (421) bond type in fcc structure and (422) bond type in hcp structure.

bcc (N=14)	fcc (N=12)	hcp (N=12)
8×(666)	12×(421)	6×(421)
6×(444)		6×(422)

Table 3.1: CNA signatures of bcc, fcc and hcp crystal structures.

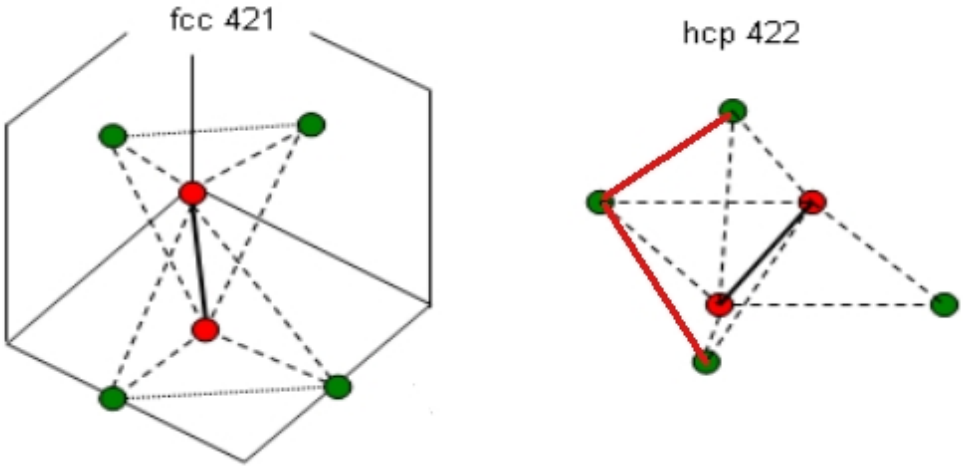

Figure 3.4: Illustration of (421) bond type in fcc structure and (422) bond type in hcp structure. Red lines remake the two bonds in the longest chain of bonds connecting the common neighbors in hcp structure

The CNA detector does not work so efficiently at high temperature, since distance plays an important role in this method and this will be smeared out by strong atomic vibrations at high temperature. This problem can be solved partly by quenching the system from high temperature, details see Appendix A.

More informations about other structure detectors see Ref. [53].

3.6 Interatomic potential

The most important thing in MD simulations is the potential, from which the forces are computed. Pair potentials, such as hard sphere, Morse- and Lennard-Jones-potential, were used early in MD simulations because of their simplicity. But they are not suitable to describe metallic systems. This is due to two reasons: firstly, electrons can move freely in metal lattice. The interaction between two atoms depends not only on the distance between them, but also on the local environment. Secondly, surface atoms are handled identically to the bulk atoms in pair potentials. In order to overcome this inaccessibility, the embedded-atom-method (EAM) [54, 55] was established. In this

section, the fundamentals of the EAM method and the potentials used for calculation in this work will be recommended.

3.6.1 Embedded-atom-method (EAM)

The basic idea of the embedded-atom-method (EAM) is that positive charged atom nuclei are embedded in negative charged electron cloud. The potential energy of an atom i is given by

$$E_i = F_i(\rho_i) + \sum_{j(i \neq j)} \phi_{ij}(r_{ij}) \tag{3.7}$$

with

$$\rho_i = \sum_{j(i \neq j)} \rho_j^{at}(r_{ij}) \tag{3.8}$$

and

$$\phi_{ij} = \sum_{j(i \neq j)} \frac{Z_i(r_{ij}) Z_j(r_{ij})}{r_{ij}} \tag{3.9}$$

where the first term in equation 3.7 is the embedded energy, which is a function of electron density ρ. The simplest approximation of the electron density at point i is the sum of the single electron densities of its neighbor atoms. The second part is the pair potential term (the Coulomb core-core repulsion energy), which depends on the effective charge Z and the distance between atom i and j.

Thus the system energy is given by

$$E_{total} = \sum_i E_i = \sum_i F_i(\rho_i) + \frac{1}{2} \sum_i \sum_{j(i \neq j)} \phi_{ij}(r_{ij}) \tag{3.10}$$

For example, seven functions are needed to describe a binary alloy such as Fe-C: 3 pair potentials (Fe-Fe, Fe-C and C-C), 2 embedding functions and 2 electron density functions.

3.6.2 Potentials for Fe systems

Due to the importance of iron, many interatomic potentials are established to describe its properties. Engin *et al.* [56] analyzed available potentials for iron and concluded that only few potentials are suitable for describing both the martensitic ($\gamma \rightarrow \alpha$) and the austenitic ($\alpha \rightarrow \gamma$) phase transition. In the most available potentials, e.g., the Finnis-Sinclair potential [57, 58] and the Johnson-Oh potential [59], the free enthalpy of the bcc phase is lower than that of the fcc phase for all temperatures below the melting point.

Among the analyzed potentials, the Meyer-Entel potential [31], which was created for describing the Fe-Ni alloy system, is the only one in the class of EAM potentials, which can model the phase transition in both directions. Earlier, Yang and Johnson [60] set up an *ad-hoc* EAM potential, which is able to describe both the α and γ phases of Fe and to construct a stable interface; the transition temperature is found to be at 364 K by these authors. Müller *et al.* [61] proposed a bond-order potential, which, due to their carefully fitting, describes not only the α-γ transition, but also the γ-δ transition. Recently, Lee *et al.* [62] set up a modified embedded-atom method (MEAM) potential, which incorporates the α-γ transition. Clearly, the electronic and magnetic structure of Fe has a decisive influence on the atomic lattice structure and the α-γ phase transition. In particular, it is the ferromagnetism of the electronic system which stabilizes the bcc structure at low temperatures [63, 64, 65, 66, 67, 68]. Nevertheless, classical empirical interatomic interaction potentials have been used extensively to model Fe. The assumption behind this strategy is that these potentials have been fitted to experimental and *ab initio* data and hence "incorporate" in an effective way the underlying electronic and magnetic effects.

3.6.3 Meyer-Entel-potential

The Meyer-Entel-potential [31], which belongs to the EAM class is chosen for describing the Fe-Fe interactions in this work. This is due to several reasons:

(i) The free enthalpies of the bcc and the fcc phase cross at a transition temperature predicting the fcc phase to be stable above this temperature and the bcc phase to be stable below this temperature. The Meyer-Entel potential predicts [17, 38, 69] a transition temperature of around 550 $\pm$ 50 K rather than the experiment value of 1184 K.

(ii) Due to its simple EAM form, the Meyer-Entel potential can be calculated a factor of 10 times faster than the other potentials by Müller *et. al.* [61] and Lee *et al.* [62] mentioned above.

(iii) This potential has been used successfully in the past to study the phase transition in Fe. Bulk Fe [69, 70, 71] was investigated as well as Fe thin films [14, 15], nanoclusters [16] and nanowires [17, 18, 19].

(iv) Finally, the dynamics of the N-W transformation was analyzed in detail for this potential [19, 38].

More details for fitting the Meyer-Entel potential see Ref. [31, 72] and Appendix B.

3.6.4 Fe-C potentials

Several empirical interatomic potentials have been published to describe the Fe-C interaction. Johnson *et al.* [73] developed a pair potential for Fe-C but excluded the C-C interaction. With this potential, the authors reproduced the migration energy of C in the Fe lattice, the activation volume of the migration and the binding energy of the C atom to a vacancy. Rosato [74] improved the Johnson potential by including a Finnis-Sinclair [57] embedded-atom model (EAM) potential for the bcc phase and a Rosato-Guillope-Legrand potential [75] for the fcc phase. By using this potential, the energy of a C atom in an octahedral site and the elastic properties were well reproduced. More recently, several EAM-based Fe-C potentials have been published [25, 28, 76]. Among them, the potential of Becquart *et al.* [28], which was developed for Fe-C systems with low carbon concentrations, has been fitted to *ab initio* data on the energetics of C interstitial atoms and C-vacancy binding energies. The Hepburn-Ackland [76] potential is based on density function theory and includes the short-ranged covalent bonding between C atoms. Both the Becquart *et al.* potential and Hepburn-Ackland potential were successfully used in reproduction of the Snoek effect [77], the interactions between C atoms and lattice defects [78, 79], ordering in supersaturated Fe-C alloys [80] and the effect of defects on C diffusion [81, 82]. These, however, only describe the low-temperature α phase.

Chapter 4

Temperature-induced phase transitions in a biphasic Fe system

In recent years, interest is rising to study systems containing an α-γ interface. Several simulation studies have been performed, which employ MD simulation. Bos *et al.* [83] reported that no phase boundary motion could be observed in MD simulations when periodic boundary conditions in the two directions parallel to the phase boundary were applied. In this study, phase boundaries obeying Bain and K-S orientations were employed. Song and Hoyt [84] used MD simulation to study the mobility of the phase boundary which obeyed a "quasi" N-W relationship: the fcc crystal is tilted by 4.04 ° from the N-W relationship in order to create a step structure on the interface. The authors noted that this structure increases the fraction of coherent atoms at the phase boundary; thus the huge misfit stress is released and the motion of the interface in the $\gamma \rightarrow \alpha$ phase transition is facilitated. In summary, it is hard to model an interface with rational orientation relationship, which will move under conventional conditions, i.e., periodic boundary conditions.

In this chapter, the energetics and dynamics of the phase transition in an Fe bicrystal containing a bcc/fcc interface will be studied by using MD simulation and the Meyer-Entel interaction potential. The phase boundary energy of a phase boundary obeying N-W orientation relationship will be computed. Two temperatures (100 K and 1300 K) will be investigated to study both austenitic and martensitic phase transition. The propagation velocities at both of the two temperatures will be calculated and compared to previous results.

4.1 Methodology

Because of the metastability of the fcc phase at low temperatures (the free-enthalpy difference between the fcc and the bcc phase amounts to only ∼0.04 eV/atom. [56]) and the sensitivity to the boundaries of the simulation box, the size of the system and the method of relaxation must be selected with care. A simulation box with dimensions of $100.74 \times 284.93 \times 99.72$ Å^3 is constructed. The simulation box and the orientation of the bcc crystallite, are depicted in Fig. 4.1. The box size corresponds to 35 (70, 25) atom layers in the x (y, z) direction. Then the bcc atoms, whose y coordinates (perpendicular to the phase boundary plane) are larger than 142.5 Å (i.e., half of the simulation cell), are deleted. The empty space is filled with fcc Fe-atoms. There are 38 (67, 22) atom layers in the fcc cell in the x (y, z) direction. The total number of atoms is 241 784. The bcc and fcc atoms are positioned such as to satisfy the N-W relation. In all simulations, periodic boundary conditions are employed at all sides of the simulation box.

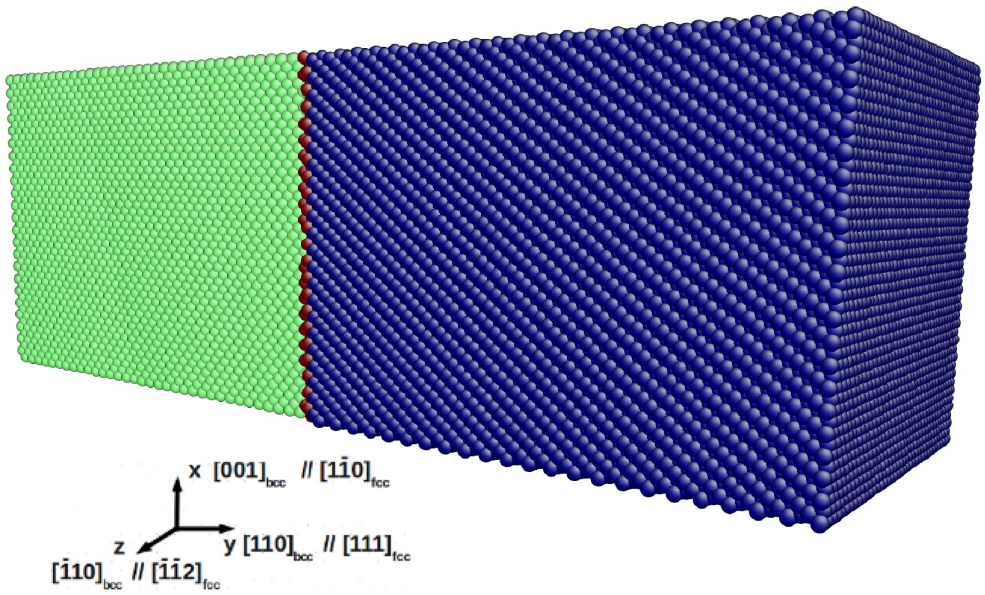

Figure 4.1: Setup of the simulation bicrystal consisting of an fcc and a bcc crystallite. The crystallographic orientations (according to the N-W relationship) at the interface are indicated. The colors denote the local crystal structure. Green: bcc; dark blue: fcc; red: unknown.

To relax the system, and in particular to equilibrate the interface, the method of energy minimization by conjugate gradients at 0 K is used, more details for this method see Section 3.3. It is performed twice: The first time, the phase boundary is fixed and the potential energy of the system (apart from the interface atoms) is minimized. The second time, also the phase boundary atoms are allowed to move perpendicular to the interface plane. Thus the simulation box may expand/contract perpendicular to the phase boundary,

so that the high stress caused by the phase misfit at the phase boundary is also reduced. The box is not allowed to change its dimensions in the x and z direction. Note that it would have been desirable to allow complete relaxation of the interface atoms, also in x and z direction, parallel to the interface; however, it is found that the interface collapses and the system starts phase transition already during the relaxation process. After relaxation, the potential energy per atom far away from the boundary converges to the cohesive energies of the bcc and fcc iron crystallites, which amount to E_{bcc} = 4.27 eV and E_{fcc} = 4.24 eV at 0 K, respectively. The pressure perpendicular to the interface relaxes to < 20 MPa.

The specific phase boundary energy E is calculated by using the following equation:

$$E = \frac{E_{total} - (E_{bcc}N_{bcc} + E_{fcc}N_{fcc})}{2A} \tag{4.1}$$

where E_{total} is the total potential energy of the simulation volume. The factor of 2 in the denominator takes into account that due to the periodic boundary conditions, there are effectively two interfaces in the system.

After constructing the interface, the dynamic simulations are performed in an NPT ensemble with vanishing pressure. The pressure decreases to < 20 MPa in all cartesian directions within 4 ps and fluctuats at this level. The temperature is controlled via a Nosé-Hoover thermostat. The simulations are performed at the temperature of 100 K and 1300 K, which are considerably below and above, respectively, the α-γ transition temperature.

The local lattice structure is determined by the common neighbor analysis (CNA) [52] and using the centrosymmetry parameter [49]. For the determination of the interface velocity the roughness of the interface is taken into account by performing both spatial and temporal averaging; for five different time steps the ten maximum and minimum positions of the interface atoms (based on their local lattice structure) are determined and averaged. All calculations are performed with the open-source LAMMPS code [85].

4.2 Results and discussion

4.2.1 The bcc/fcc interface

Firstly, the properties of the interface as created will be discussed. Fig. 4.2 demonstrates the good quality of the created interface. It has a width of ∼2 monolayers, in the sense that the first monolayer on the bcc and on the fcc side cannot be identified.

However, the misfit between the lattice constants of the bcc phase necessitates that misfit dislocations are generated. This already happens in the 0 K relaxation procedure. The generation of misfit dislocations at the bcc/fcc interface of Fe has been observed early

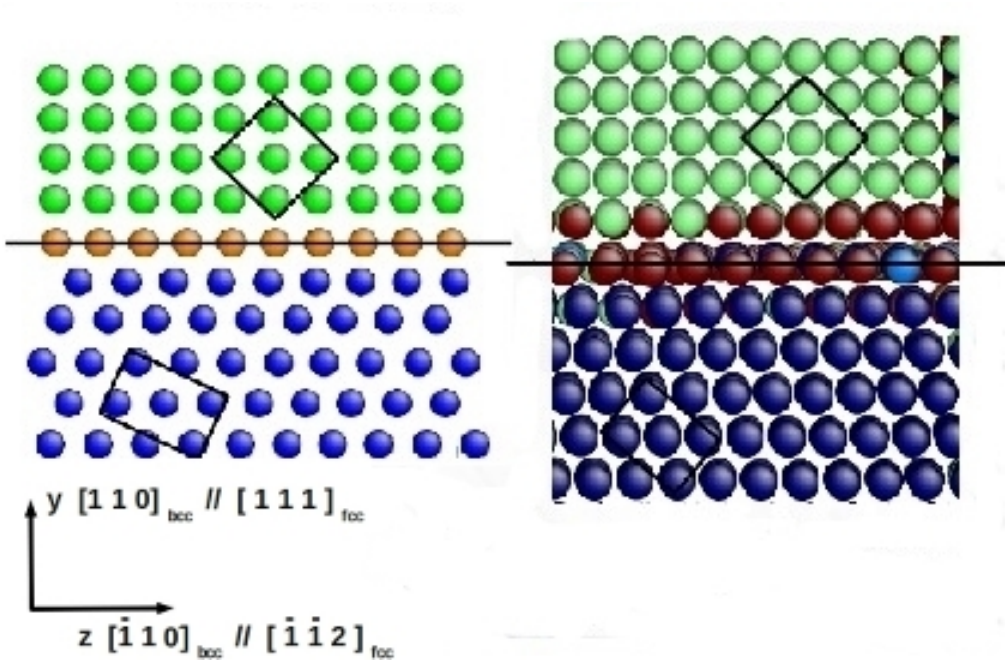

Figure 4.2: Cross-sectional view (in the y-z plane, cf. Fig. 4.1 of the fcc-bcc interface. The picture on the left shows an ideal interface according to the N-W relationship; the picture on the right is the simulation result of a relaxed interface at 0 K. The square and rectangle show a bcc (bct) unit cell in the bcc and fcc phase, respectively. Colors denote the local crystal structure. Green: bcc; dark blue: fcc; light blue: hcp; red: unknown. Note that the structure of the phase boundary has not been destroyed during the relaxation process

in experiment [86] and has been used for modeling the interface [86]. In these studies, the occurrence of so-called "structural ledges", usually triatomic jumps of the interface plane, has also been observed. These ledges correspond to a tilt of the interface plane around the $[\bar{1}01]_{\mathrm{bcc}} \parallel [001]_{\mathrm{fcc}}$ direction by an angle θ. Since by this rotation the N-W interface is no longer the $(111)_{\mathrm{fcc}} \parallel (011)_{\mathrm{bcc}}$ plane, these structural ledges were not realized in the present model. In addition, Fig. 4.3 displays a threading dislocation generated on the bcc side of the specimen. Its Burgers vector is in the $[1\bar{1}\bar{1}]$ direction. Note that Fig. 4.2 presents a part of Fig. 4.3 in which there is no dislocation.

The fcc and bcc lattices are not in complete registry along their conjugate habit planes; as consequence misfit dislocations are generated to build a semicoherent phase boundary. Using the lattice constant of bcc Fe (2.869 Å) and fcc (3.686 Å) as implemented in the Meyer-Entel potential at 0 K, the atom distances parallel to the interface can be quantified. In the x direction ($[001]_{\mathrm{bcc}} \parallel [1\bar{1}0]_{\mathrm{fcc}}$) atoms are 2.87 (2.61) Å apart on the bcc (fcc) side. In the z direction ($[01\bar{1}]_{\mathrm{bcc}} \parallel [11\bar{2}]_{\mathrm{fcc}}$) the distance is 4.06 (4.51) Å on the bcc (fcc) side. Thus the areal atomic density in the habit plane is slightly higher (by 1.1 %) on the bcc than on the fcc side, hence the misfit dislocations.

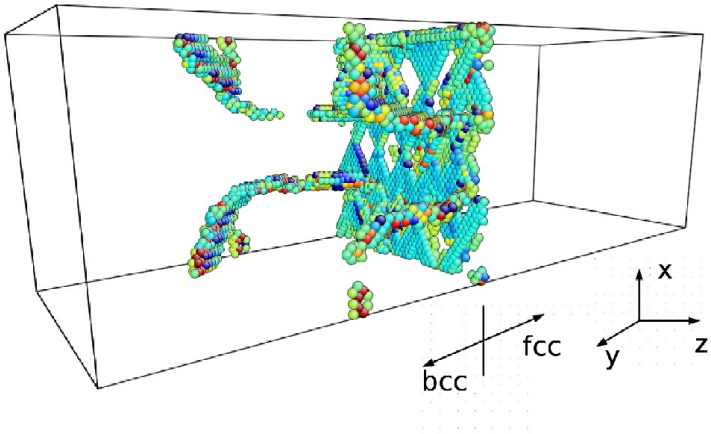

Figure 4.3: Three-dimensional snapshot of "irregular" atoms (with centrosymmetry parameter from 1 to 8) on the bcc-side of the relaxed interface. These atoms from the core of a dislocation starting and ending at the interface.

Figure 4.4 shows the disregistry of atoms in the interface, highlighted by the potential energy of the interface atoms. This disregistry corresponds to the network of the dislocations generated. Note that the periodic structure of the interface is strongly disturbed. This is due to the relaxation process, which allows atoms to relax in the direction perpendicular to the interface; this leads to a nonplanar interface geometry. The area of a unit mesh in the perturbed periodic structure amounts to 521 Å^2; the rhombi have a horizontal length of 48.5 Å and a vertical height of 48.5 Å. Note that bcc/fcc heterointerfaces have been studied with great detail. For instance Ref. [87] analyzed the misfit dislocation structure of the Cu-Nb interface, while the geometry and energetics of the Cu-Ta interface were invesitgated in the Ref. [88]; the microstructure of the latter interface was investigated by Ref. [89], which also demonstrated the effect of the total (simulated) interface area on its structure.

The phase boundary energy amounts to 3.84 Jm^{-2}. This value however, calculated using the equation 4.1, includes the energy of the misfit dislocations. The energy of the pure interface is separated off by using a smaller detector box within which the equation 4.1 is applied; in this box, atoms of the dislocation core can be avoided. The detector box has a square form with edge length of 3 Å. This gives a value of E = 0.96 Jm^{-2}. This value is insensitive with respect to the size and shape of the detector box, as long as it is well inside the low-energy valley of the dislocation network structure seen in Fig. 4.4.

Previously the bcc/fcc interface energy was determined by Yang and Johnson [60], using an *ad-hoc* constructed interatomic interaction potential. They obtained a value of 0.33 Jm^{-2}, which is, however, a factor of around 2.5 smaller than the experimental value of 0.8 Jm^{-2} [60, 90]. Note, however, that the experimental value was determined as an

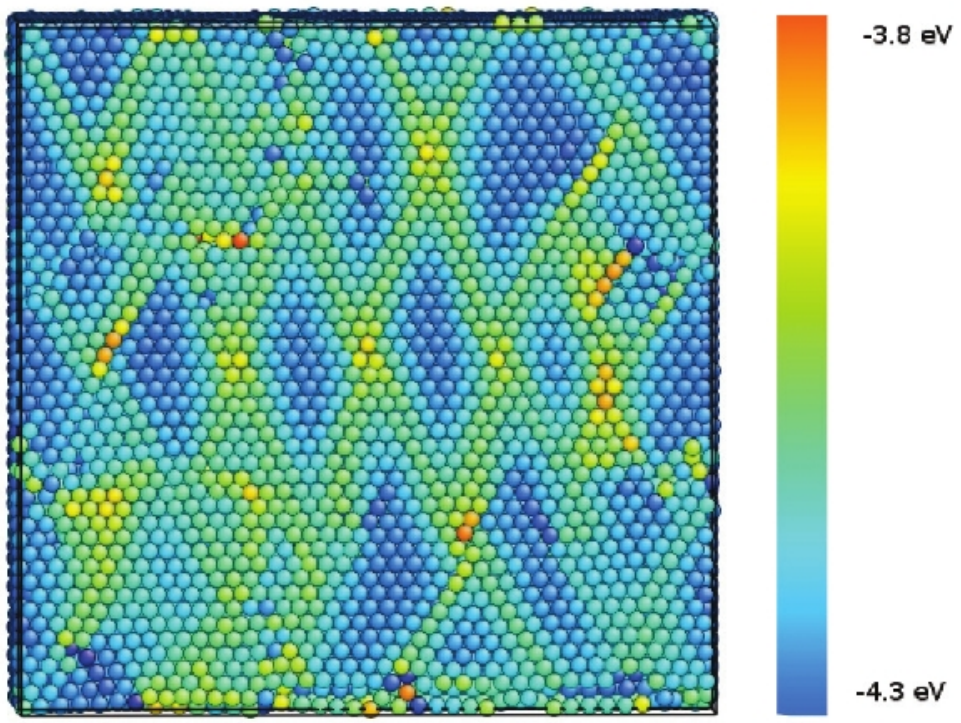

Figure 4.4: View on the interface plane. Atoms have been colored according to their potential energy, see color bar.

average over all (unspecified) interface geometries present in the experiments. Yang and Johnson [60] determined the interface energy without including the misfit dislocations, which they also found for their potential; they achieved this by using a movable detector box and averaging over many box positions. Yang and Johnson also calculated the interface energy for phase boundaries which incorporate structural ledges. They found that these ledges generally decrease the interface energy (down to values of 0.24 Jm^{-2}); however, for the experimentally relevant case of triatomic ledges [86], they found an increased energy of 0.46 Jm^{-2}. The result of E = 0.96 Jm^{-2} (excluding the misfit dislocation energy) agrees satisfactorily with the experimental value, but is larger than the previous simulation date of Ref. [86].

The reliability of the Meyer-Entel potential may be discussed with the help of the surface energies of differently oriented crystal surfaces. Table 4.1 summarizes the surface energies as calculated for the Meyer-Entel potential. The values for the bcc $\{110\}$ and the fcc $\{111\}$ surface are of particular importance for the N-W geometry and have also been calculated by Yang and Johnson [60] for their *ad-hoc* constructed EAM potential; their values of 1.362 and 1.309 Jm^{-2} are in satisfactory agreement with the present results. Experimental data are available for the fcc surface at 1623 K, averaged over surface orientation [90]; the value of 1.35 Jm^{-2} is compatible with the theoretical data. However, more recent experiments obtain a value of 2.41 Jm^{-2} from an extrapolation of liquid-state

	Experiment		*Ab initio*	Ref. [86]		Present Work	
	bcc (0K)	fcc (1623K)	bcc	bcc	fcc	bcc	fcc
{100}			2.29			1.727	0.956
{110}			2.27	1.362		1.375	1.663
{111}			2.52		1.309	1.844	1.266
average	2.41	1.35					

Table 4.1: Surface energies (in Jm^{-2}) of bcc and fcc Fe at 0 K. The present results are calculated at 0K for Meyer-Entel potential. *Ab initio* data from Ref. [91]. Experimental data are from Ref. [92] for bcc at 0 K and from Ref. [90] for fcc at 1623 K.

surface tensions to the bcc phase at 0 K [92]; these are in rough agreement with more recent *ab initio* data, which give 2.29 (2.27, 2.52) Jm^{-2} for the $\{100\}$ ($\{110\}$, $\{111\}$) bcc surface [91].

4.2.2 Martensitic (fcc $\rightarrow$ bcc) transformation

The dynamics of the biphasic crystal at a temperature below and above the transformation temperature were studied to reveal the phase transition dynamics. In this subsection, the results for a temperature of 100 K will be discussed, where the bcc phase is stable. Fig. 4.5 presents snapshots which demonstrate the ongoing phase transition. Both homogeneous and heterogeneous growth of the bcc phase are observed.

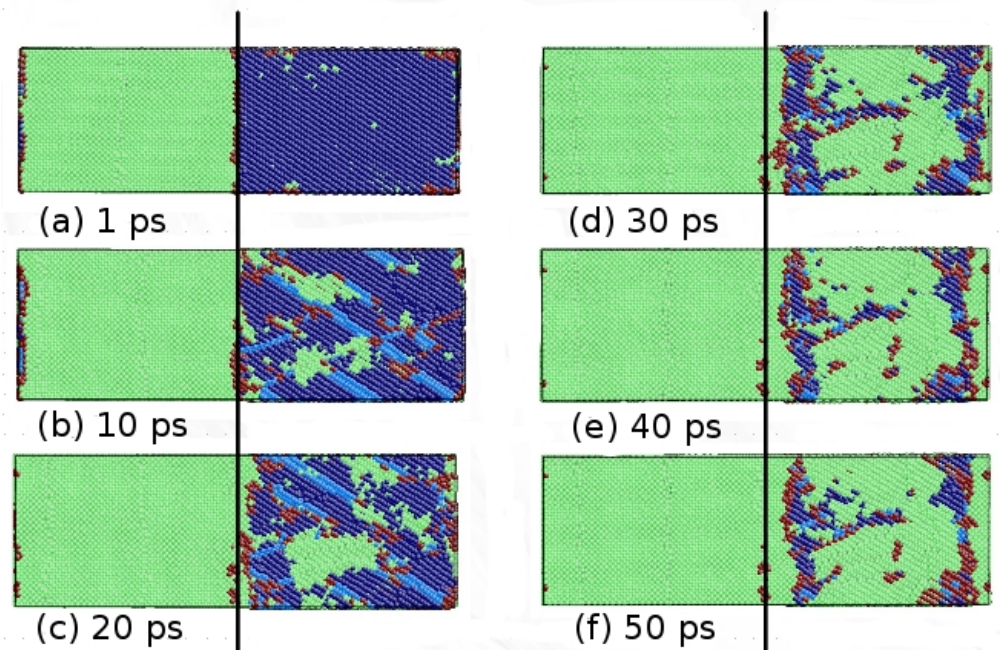

Figure 4.5: Snapshots (y-z plane) showing the time evolution of the local structure of the fcc-bcc biphasic system at a temperature of 100 K within the first 50 ps. The colors denote the local crystal structure. Green: bcc; dark blue: fcc; light blue: hcp; red: unknown. The original position of the interface has been marked by a black line.

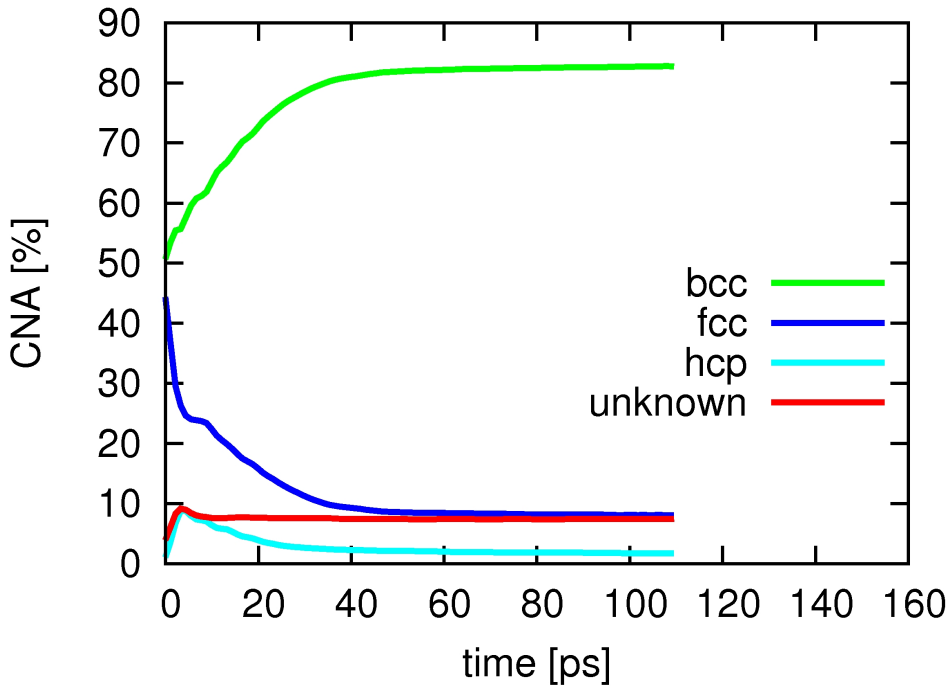

Figure 4.6: Temporal evolution of the fractional phase content, as evaluated by common neighbor analysis (CNA), of the bicrystal at a temperature of 100 K

Heterogeneous growth occurs at the phase boundaries and involves the motion of the interface. Due to the periodic boundary conditions, the system exhibits two interfaces, one in the middle (marked by the black vertical line) and one at the left/right boundaries. The recession of the interfaces towards the shrinking fcc grain are clearly observed; their motion towards the fcc side is clearly discernible already at 20 ps and continues until the last snapshot at 50 ps. The velocity of the interface motion will be discussed in Subsection 4.2.4.

In addition, the stable bcc phase nucleates within the fcc grain (homogeneous nucleation). The homogeneously created bcc patches have different orientation than the initial bcc phase (cf. the discussion of Fig. 4.7 below); already at 30 ps the various homogeneously nucleated patches have joined and form one connected bcc region.

Homogeneous and heterogeneous growth occur simultaneously and concurrently. Note that the homogeneously nucleated bcc phase remains separated from the initial bcc material; this is caused by the different orientations of these two phases, see discussion Fig. 4.7 below. Thus grain boundaries remain between the virgin bcc grain and the transformed bcc grain.

Figure 4.6 displays the time evolution of the fractions of each phase in the system. The bcc fraction steadily increases until, at $\sim$40 ps, it saturates. At the end of the simulation, over 90 % of the system has been transformed (disregarding the unidentified atoms). Analogously, the fraction of fcc atoms decreases. During the transformation process some

hcp material is also formed with a maximum early after the start of the transformation; it soon decreases again. This phase must be interpreted as being formed by stacking faults in the transforming fcc phase, see also Fig. 4.7 below.

The amount of atoms not identified by the CNA detector increases slightly during the first few picoseconds; this is due to the buildup of roughness of the interface, as discussed below. After that time the percentage of unidentified atoms stays constant at around 15 %. Fig. 4.5 demonstrates that these unidentified atoms are situated at the ragged boundaries between the fcc and bcc phases. They also form a large part of the grain boundaries which separate the growing initial bcc region and the homogeneously nucleated new grain. Since this grain boundary persists until the end of the simulation, the fraction of unidentified atoms does not decline.

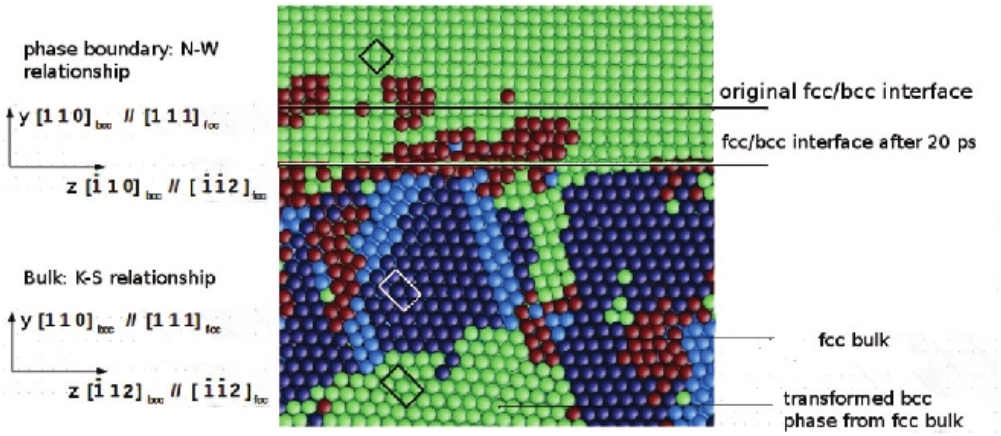

Figure 4.7: Side view of a slice (y-z plane) in the phase transforming system at 100 K at the time of 20 ps. The black square on the upper (bcc) side shows a bcc unit cell. The white and black rectangles on the lower side show bct lattice cells in the transforming fcc and bcc phase. The colors denote the local crystal structure as in Fig. 4.5. The original and the actual positions of the interface are indicated.

Figure 4.7 shows the local structure in detail at 20 ps. This figure shows clearly that the bcc phase, which grew from the phase boundary, and the bcc phase, which nucleated homogeneously in the bulk fcc phase, have different orientations. Both the initial fcc and the nucleated bcc phase can be described by the same lattice cell in the plotted plane. A closer inspection shows that the homogeneously nucleated bcc phase is oriented towards the initial fcc phase as in a K-S relationship; in the plotted y-z plane, it is $[110]_{\mathrm{bcc}} \parallel [111]_{\mathrm{fcc}}$ and $[\bar{1}12]_{\mathrm{bcc}} \parallel [\bar{1}\bar{1}2]_{\mathrm{fcc}}$. Such a transformation occurs by atom motion along the z direction and thus parallel to the interface (cf. Fig. 4.1 and Fig. 4.2). Note that, in the Meyer-Entel potential, the bcc-fcc interface in K-S geometry has an interface energy of only 2.88 Jm^{-2}, which is distinctly lower than the N-W value of 3.84 Jm^{-2}.

4.2.3 Austenitic (bcc → fcc) phase transition

The phase transition was studied at a temperature of 1300 K in a second simulation, where the fcc phase is stable. Fig. 4.8 displays the dynamics of the transformation. Fluctuation in the local structure are more frequent than in the low-temperature case of Fig. 4.5; these are evidently due to the increased temperature. As a consequence, it is not so easy to distinguish interface roughening from the fluctuations occurring in particular in the bcc phase. However, by comparing the snapshot at 20 ps with the original one, the interface has not moved up to this time; only after this time, the left interface moves quickly and transforms the bcc to fcc material. The facts that only one of the interfaces moves and that interface motion is inhibited for 20 ps suggests that the phase transition requires an activation energy to be surpassed; i.e., it is kinetically hindered. Note furthermore that no homogeneous nucleation of the fcc phase occurs; indeed at 10 ps, a close-packed nucleus appears to have been formed, see Fig. 4.8(b), but it vanishes again since it is subcritical.

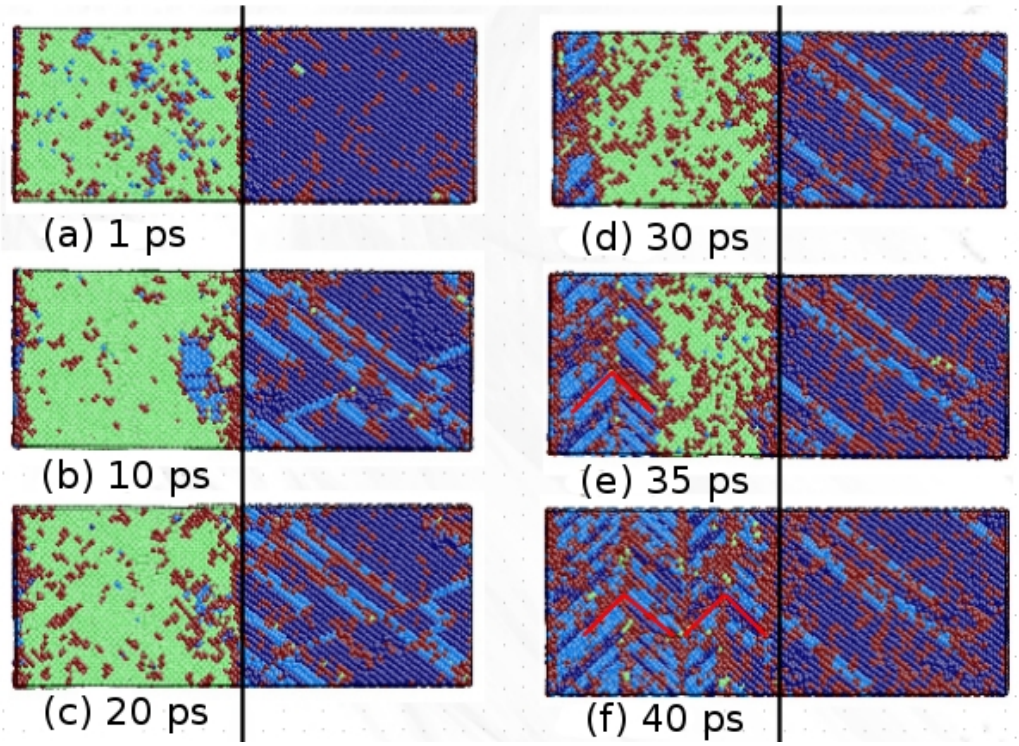

Figure 4.8: Snapshots (y-z plane) showing the time evolution of the local structure of the fcc-bcc biphasic system at at temperature of 1300 K within the first 40 ps. The colors denote the local crystal structure as in Fig. 4.5. The original position of the interface has been marked by a black line. The red lines in (e) and (f) indicate the twin structure in the transformed cp phase.

Figure 4.9 shows how the free-energy difference between the fcc and the bcc phase evolves along the Bain path as a function of temperature. Previously, Sandoval and Urbassek [38] showed that the energetics along the Bain path closely follows that of the

N-W path; hence for simplicity the Bain path is used here. The data have been calculated for the Meyer-Entel potential used in this work using the technique of metric scaling [93]; for details see Ref. [56]; Note that this technique leads to somewhat lower transition temperature (around 500 K) than the technique of thermodynamic integration (around 600 K), see Ref. [56]; due to the small slope of the free-energy curves, this difference is, however, minor and a value of 550 $\pm$ 50 K for the transition temperature can be assumed.

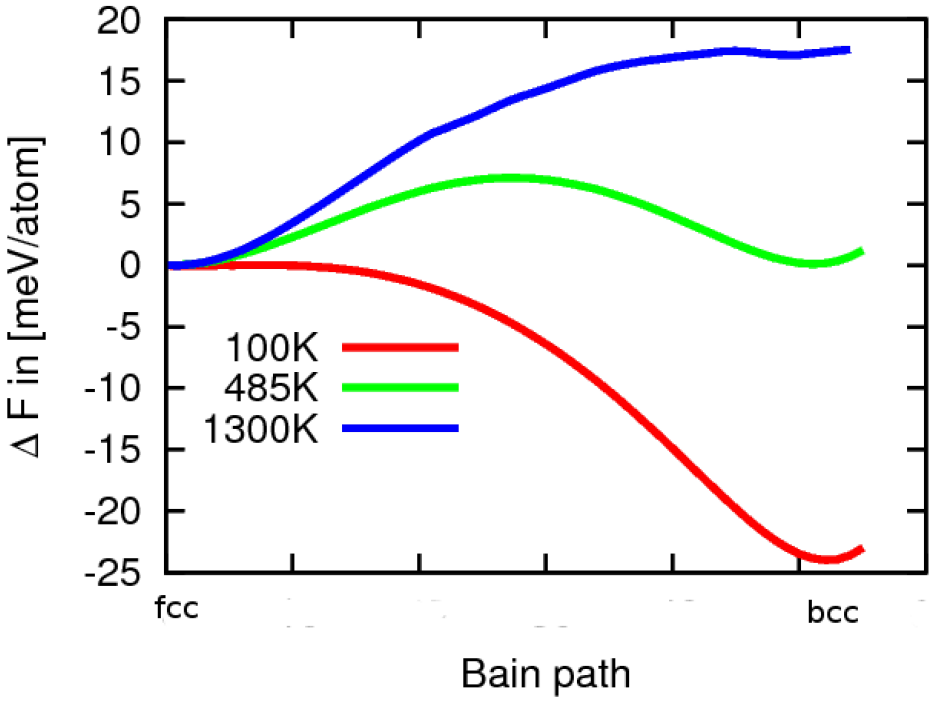

Figure 4.9: Evolution of the free-energy difference ΔF along the Bain path from the fcc to the bcc phase for serval temperatures.

The main feature seen in Fig. 4.9 is how the free energy difference of the bcc phase (right-hand side of the plot) changes with temperature from negative to positive values. For temperatures around the phase-transition temperature $\sim$550 $\pm$ 50 K, in addition a clear activation energy (maximum in the free-energy curve) is visible with a value of 7 meV/atom. However, for the other temperatures plotted also, such activation energies exist ever though they are barely visible in the plot. At 100 K, the barrier is towards the fcc part of the transformation path; it has a height of only 0.016 meV/atom. At 1300 K, the activation energy is found at the bcc side of the path with a value of 0.28 meV/atom. This temperature dependence is in agreement with the finding of an inhibition of the bcc $\rightarrow$ fcc transition. Furthermore, simulations were performed at 300 K (kinetic barrier height of 2.5 meV) and at 1000 K; at both temperatures the interface was metastable and the simulations showed no phase transformations within the simulation time of 500 ps.

It is well known that the interface velocity depends in an Arrhenius-type of law on the activation energy, which separates the two phases [94, 95]. During the transition, part of the fcc material appears to transform to hcp. Since the transformed hcp material shows up in the form of narrow bands, they should be considered as stacking fault planes in the fcc material produced by the high temperature. Also in the transformed region, a high amount of hcp material is formed. Note that the fcc and hcp phase have similar energies; for the Meyer-Entel potential the energy difference between the two phases is only 4.6 meV/atom. In this context, it is hence more appropriate to talk about a bcc $\rightarrow$ cp (close-packed) transformation. Interestingly, the transformed material shows a twinned structure. This is not unexpected and has been observed previously, for instance in a study of the martensite phase transition in iron by using the Finnis-Sinclair potential [96].

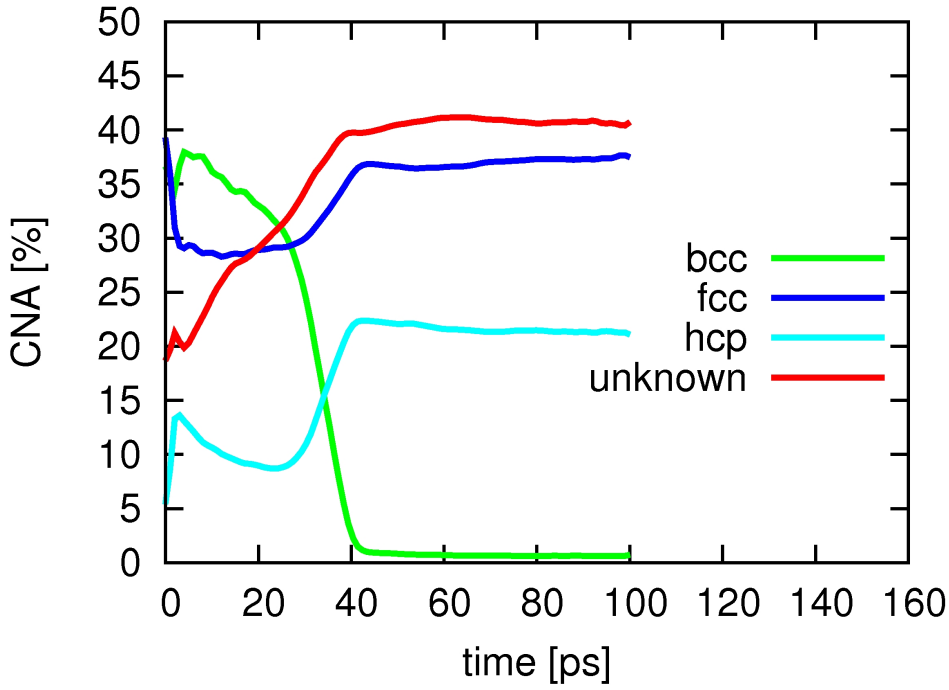

Figure 4.10: Temporal evolution of the fractional phase content, as evaluated by common neighbor analysis (CNA), of the bicrystal at a temperature of 1300 K.

Figure 4.10 shows the time evolution of the fractions of each phase in the system. After $\sim$40 ps, the bcc phase has been completely destroyed, and has been transformed to the cp phase (hcp and fcc). As was already observed in the snapshots of Fig. 4.8, the fraction of hcp material increases strongly (to 13 %) in the first ps; this is caused by stacking-fault formation. During the inhibition period described above, mainly the amount of unidentified atoms increases. The phase transformation is then achieved quite quickly in the time period of 20-40 ps. The high percentage of unidentified atoms (about 40 % at the end of the simulation) is mainly due to the high temperature; the thermal vibrations are

strong and the CNA detector does no longer work so satisfactorily. This problem can be solved by quenching of the system, see Appendix A.

4.2.4 Interface velocity

The propagation velocity of the phase boundary at 100 K has been found in our simulation to be quite constant in time. A value of 24 m/s for each of the two interfaces was determined during the time interval of 0-50 ps. The austenitic phase transformation at 1300 K, in contrast, showed an inhibition period of 20 ps, and the velocity of the two interfaces is strongly different, such that no unique value for the interface velocity can be given. The transformation proceeds an average velocity of 284 (81) m/s for the left (right) interface during the time interval of 0-40 ps. However, for the time of 25-40 ps, where the transformation rate is highest (cf. Fig. 4.10), the left interface moves with 454 m/s. Thus the interface velocity is almost an order of magnitude larger than at 100 K; note that at the low temperature also homogeneous nucleation helps the phase transformation such that overall transformation rates displayed in Fig. 4.6 and 4.10 are comparable at the two temperatures. The competition of homo- and heterogeneous phase growth will be discussed detailedly in Chapter 6.

Bos *et al.* [83] investigated the dynamics of the martensitic transformation using the Johnson-Oh potential [59], and found velocities of 200-700 m/s; these are almost one order of magnitude higher than the velocities in this work for the martensitic transformation. More recently, Tateyama *et al.* [97] employed the Finnis-Sinclair potential [57, 58] to calculate the propagation velocities of the bcc/fcc phase boundary in the vicinity of the transition temperature, which is at 1516 K for this potential. They found velocities of about 25 m/s and 15 m/s for the bcc $\rightarrow$ fcc and the fcc $\rightarrow$ bcc phase transition, respectively; these values are in satisfactory agreement with the values in this work for the martensitic phase transition. Recently, Song and Hoyt [84] studied the dynamics of the interface in an unusual geometry, 4.04 $^\circ$ rotated from the N-W orientation. They reported velocities as low as 1 m/s.

The notion of an interface velocity as a constant describing the process of phase transformation has to be used with care. (i) The transformation proceeds both by interface motion and by the homogeneous nucleation of the new phase inside the grains of the metastable phase; this is a competing process and may hinder the interface motion, see Chapter 6. (ii) In the simulations, the interface does not move smoothly; rather an incubation time before the interface starts moving is found, and the interface motion is not continuous. Experiments find that the mobility of the fcc/bcc interface in Fe follows an Arrhenius behavior with an activation energy comparable to that of self-diffusion in ferrite [98].

Finally, the numbers stated here for the interface velocity also have to be taken with caution. When performing simulations with varying shape and size of the simulation volume, the competition of heterogeneous and homogeneous phase growth processes described here are always observed, but the quantitative growth kinetics and hence also the interface velocity show a dependence on system size, see Chapter 6.

4.3 Conclusions

This chapter treated the temperature-induced phase transformation of an Fe bicrystal containing a bcc/fcc interface in N-W geometry. At the interface the system adjusts to the different lattice structures by forming the misfit and threading dislocations. The interface energy without the energetic contribution of the dislocations amounts to 0.96 Jm^{-2}, which is in fair agreement with experiment.

The transformation does not proceed during affordable simulation time scales when the temperature is chosen too close to the transition temperature; here the kinetic is slow and the activation energy between the two phases is high. Only two temperatures were found where the transformation could be studied.

The martensitic (fcc $\rightarrow$ bcc) transformation was studied at a temperature of 100 K. At this temperature, the interface slightly roughens, then proceeds with an approximately constant velocity of 24 m/s. Simultaneously, homogeneous nucleation of the bcc phase in the bulk fcc grain occurs. At the high temperature of 1300 K, the austenitic (fcc $\rightarrow$ bcc) phase transition was observed. Here the grain growth is inhibited for about 20 ps and no homogeneous nucleation can be observed. Both features can be explained by a kinetic barrier between the two phases, which is larger at higher than at the lower temperature. The interface velocity after the incubation period amounts on average to 180 m/s, but assumes maximum values of 450 m/s.

Chapter 5

Shear-deformation-induced phase transitions in a biphasic Fe system

While the original interest in studying the martensite phase transformation focused on its dependence on temperature and quench rate, its dependence on external stress also became a major issue. Such stresses develop invariably in realistic situations, either by external influences or by the developing microstructure itself. The martensitic transformation itself leads to stresses due to the change in lattice structure and volume of the new phases. Recently, a new class of steels, the TRIP (transformation-induced plasticity) steels, have been introduced. Due to the transformation-induced strain, TRIP steels have not only higher hardness, but also improved ductility compared to traditional steels [99, 100, 101, 102]. It is therefore interesting to study the mechanisms by which external strains influence the α-γ phase transition in iron [103]. The influence of an applied uniaxial stress on the energetics of the nucleation of a bcc grain near a bcc/fcc interface was studied in Ref. [104].

About 90 % of all α-γ phase transitions obey either a N-W [32, 33] or a K-S [34] relationship [41]. It is well known the N-W and K-S models explain the existence of conjugate habit planes in the martensitic phase transition, which can not be explained by the Bain model [39]. In addition, they emphasize that the martensitic phase transition is connected to a shear deformation on the habit plane, see Subsection 2.2.2 for detail.

In the last chapter, the temperature-induced fcc $\leftrightarrow$ bcc phase transformation in a biphasic fcc/bcc crystal was studied. The phase boundary with N-W orientation moves only at temperatures far away from the α-γ transition temperature. The simulations up to now have demonstrated that it is non-trivial to model an fcc/bcc interface in Fe with a rational orientation relationship that will move under conventional conditions, i.e., periodic boundary conditions.

In this chapter, the influence of shear deformation on the α-γ phase transition in Fe will be investigated. In preliminary simulations, the shear deformation of homogeneous fcc or bcc single crystals, without including a phase boundary, was studied. Depending on the boundary conditions and the simulation ensemble (NVT or NPT) used, the metastable crystals either transform spontaneously during the relaxation process, before a strain can be applied; or remain stable during the relaxation and the entire shear deformation simulation. In either case, these results demonstrate that the study of the shear of a homogeneous crystal is not particularly interesting. The only exception is that the shear of a bcc crystal at 700 K induced a homogeneous transformation to the fcc phase, analogous to the results described in Subsection 5.2.3 below. Therefore it is necessary to study a more complex system. A biphasic crystallite composed of a bcc and an fcc crystallite with the interface set in N-W geometry will be used. In the last chapter, it is found that such a phase boundary stabilizes the metastable phase in the temperature range considered here (300-700 K). Shear strain whose direction is chosen such as to favor the $\alpha \rightarrow \gamma$ transition will be applied to the biphasic system. The dependency on the ambient temperature, both above and below the transition temperature, will be studied.

5.1 Methodology

The setup and relaxation of the bicrystal system containing an N-W interface are identical to the system that was used in the last chapter, details see Section 4.1. The Fe atoms interact with each other by the Meyer-Entel potential [31]. For the N-W relationship, the fcc $\rightarrow$ bcc phase transition as occurring in two steps, see Fig. 5.1(a).

(i) One of the $\{111\}_{\text{fcc}}$ planes (habit plane) is fixed and the two neighboring $\{111\}_{\text{fcc}}$ planes are shifted in opposite directions with a common uniform shear in the $[11\bar{2}]_{\text{fcc}}$ direction, which corresponds the z-direction in the simulation. This corresponds to a shear strain with an angle of 19°28'.

(ii) An orthogonal expansion/contraction is applied in order to achieve the desired atomic density.

According to step (i), shear should be applied externally in order to trigger an fcc $\rightarrow$ bcc transformation. Shear deformation is applied in the x-z plane for the biphasic system, Fig. 5.1(b), by controlling the shear angle. Note that the shear deformation ϵ_{xz} is connected to the shear angle ϑ via

$$\epsilon_{xz} = \tan \vartheta.$$

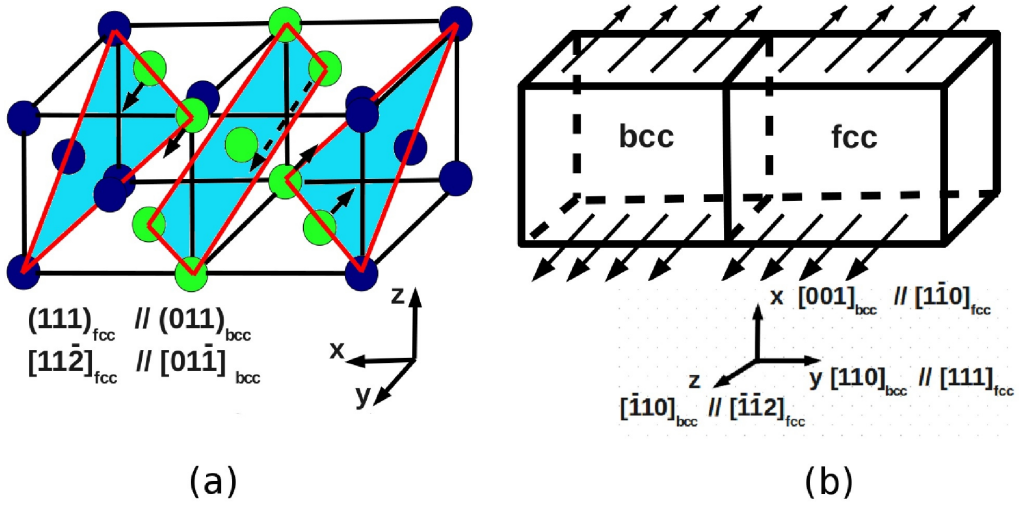

Figure 5.1: (a) N-W relationship during the martensitic transition. The blue atoms are fcc and the green atoms are bcc. The blue planes indicate the $\{111\}_{\text{fcc}}$ planes. The arrows indicate the first motion of the atoms (shear deformation of the $\{111\}_{\text{fcc}}$ planes in the $[11\bar{2}]_{\text{fcc}}$ direction), which initiates the phase transition and the dashed arrow indicates the invariant direction, which is shared by the bcc and fcc phases. (b) The shear deformation that is applied to the biphasic system. The orientations are indicated.

ϵ_{xz} is varied in steps of 1.74 % up to a maximum deformation of 50 %. After each step, the system is equilibrated in an NVT ensemble for 20 ps; here temperature is controlled by a Nosé-Hoover thermostat. The total deformation thus requires a simulation time of around 600 ps. The maximum shear angle amounts to 26.5°; this is beyond the angle of 19.5° needed for the fcc $\rightarrow$ bcc transformation in the N-W path. The shear deformation is realized by changing the shape of the simulation box. The volume is kept constant throughout the deformation; that means that the system cannot accomplish step (ii) above globally. This is consistent with rapid martensitic phase transformations in reality which will occur under (approximately) constant volume, while pressures ("residual stresses") may develop.

Temperatures from 300 K to 700 K are studied. This encompasses the range both below and above the transition temperature of the Meyer-Entel potential. Note that, all the temperatures studied here, the system is stable when no strain is applied; the interface is stable and does not move, nor does the stable phase nucleate spontaneously at the time scale of around 100 ps studied here (chapter 4).

All calculations are performed with the open-source LAMMPS code [85], and the local lattice structure is determined by the common neighbor analysis (CNA) [52].

5.2 Results and discussion

5.2.1 Deformation at 300 K

The interface is stable at a temperature of 300 K without shear deformation; the interface does not move and the bcc phase does not grow, see Chapter 4. Fig. 5.2 presents snapshots of the transition process up to the shear angle of 20°. Note that, due to the periodic boundary conditions applied, the system has effectively 2 phase boundaries (one in the middle and one at the left/right edge). Both homogeneous and heterogeneous growth of the bcc phase are observed. The homogeneous nucleation of the bcc phase takes place within the fcc bulk at a strain angle of 1.5°. The homogeneous growth of the bcc phase establishes new phase boundaries, [Fig. 5.2(c) and (d) left], while the motion of the original interfaces lets the fcc phase shrink. Homogeneous and heterogeneous growth are competitive processes. The original phase boundary with N-W relationship cannot propagate further because the homogeneously nucleated bcc phase occupies around 70 % of the space within the fcc grain. Note that the homogeneously nucleated bcc phase has a different orientation than the bcc phase, which grew from the phase boundary, see discussion of Fig. 5.3(b) below. This is the reason why grain boundaries survive in Fig. 5.2(e) and (f), which separate the original bcc grain from the homogeneously nucleated bcc grain. Note that, for further simulation time of 200 ps starting from the final strain, no reorientation of the bcc phases could be observed.

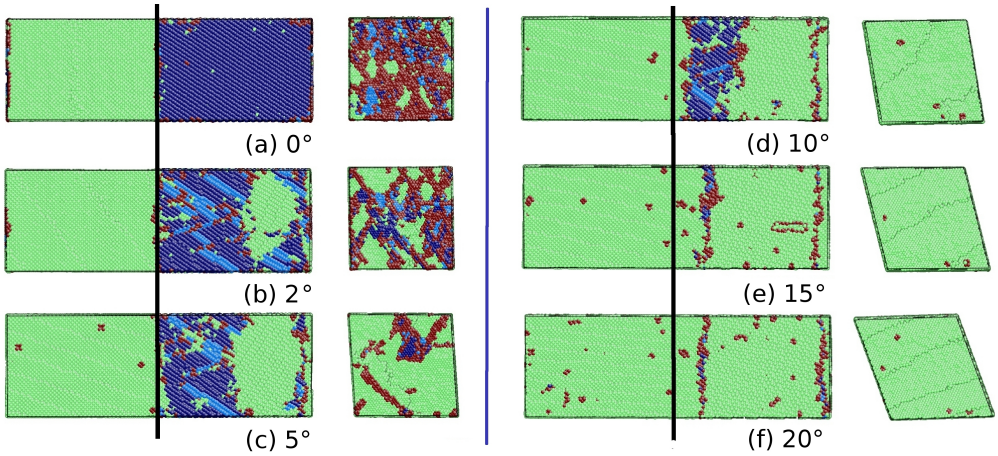

Figure 5.2: Snapshots showing the local structure of the fcc-bcc biphasic system at a temperature of 300 K for shear angles of up to 20°. The pictures on the left show the phase evolution in the y-z plane; those on the right show the original interface plane (x-z plane) in the middle of the system. The colors denote the local crystal structure. Green: bcc; dark blue: fcc; light blue: hcp; red: unknown. The original interface position is marked by a black line.

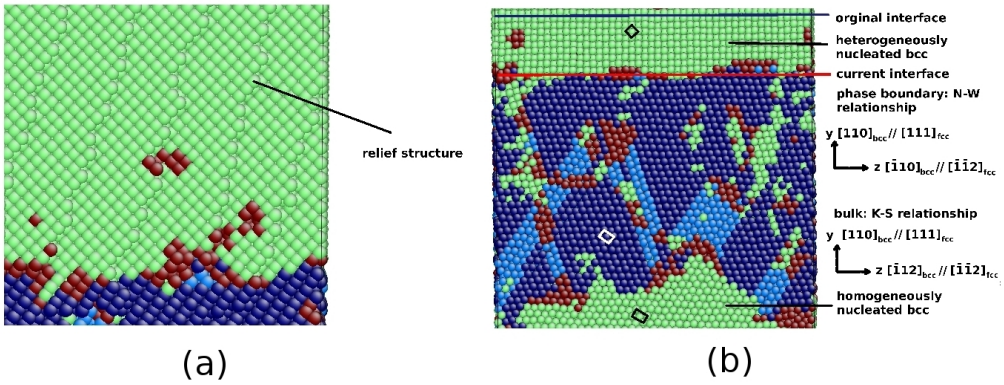

Figure 5.3: Detailed view on the transforming system at 300 K at a shear angle of $5°$, see Fig. 5.2(c). (a) Evolving topography on the y-z surface plane; only part of the system is shown. (b) Close-up of the y-z-plane; it has been rotated by $90°$ with respect to Fig. 5.2(c). The black square on the upper side shows a bcc unit cell. The white and black rectangles on the lower side show bct lattice cells in the original fcc phase and in the homogeneously nucleated bcc phase. The colors denote the local atomic structure as in Fig. 5.2. The blue line denotes the original interface position and the red line the actual position. The orientation relationships of the two differently oriented bcc phases are indicated.

Figure 5.3(a) shows a part of the surface of the biphasic system at a shear of 5°. The relief structure (occurrence of steps) that evolved during shearing can be seen clearly. Note that such relief structure is also well observed in experiment [105, 106]. This is due to the applied shear deformation on the system. The considerable lattice distortion and the high residual stress during the diffusionless martensitic phase transition cause the surface relief. The emergence of such structures is characteristic of the martensitic phase transition.

Figure 5.3(b) displays a close-up snapshot during the phase transition at a shear angle of 5°. It demonstrates that the homogeneously nucleated bcc phase has a different orientation towards the fcc phase than the original bcc phase, which grew from the N-W interface. In particular, the homogeneously nucleated phase is oriented towards the initial fcc phase as in a K-S relationship. The homogeneously nucleated bcc phase (K-S) grows faster than the initial bcc phase (N-W).

Figure 5.4 displays the fraction of each phase during the transition as a function of the shear deformation angle. The bcc phase increases steadily at the cost of the fcc phase and reaches a maximum fraction at shear angles between 15° to 20°. Here, more that 90 % of the material has been transformed to bcc. Note that this maximum coincides well with the "magic" shear angel of 19°28' needed for transforming the fcc into the bcc lattice along the N-W path. The hcp phase, which is present with a fraction of less than 10 % exists mainly in the form of stacking faults in the fcc lattice; note that most of the hcp material is present in the form of narrow stripes in the surrounding fcc lattice. The fraction of

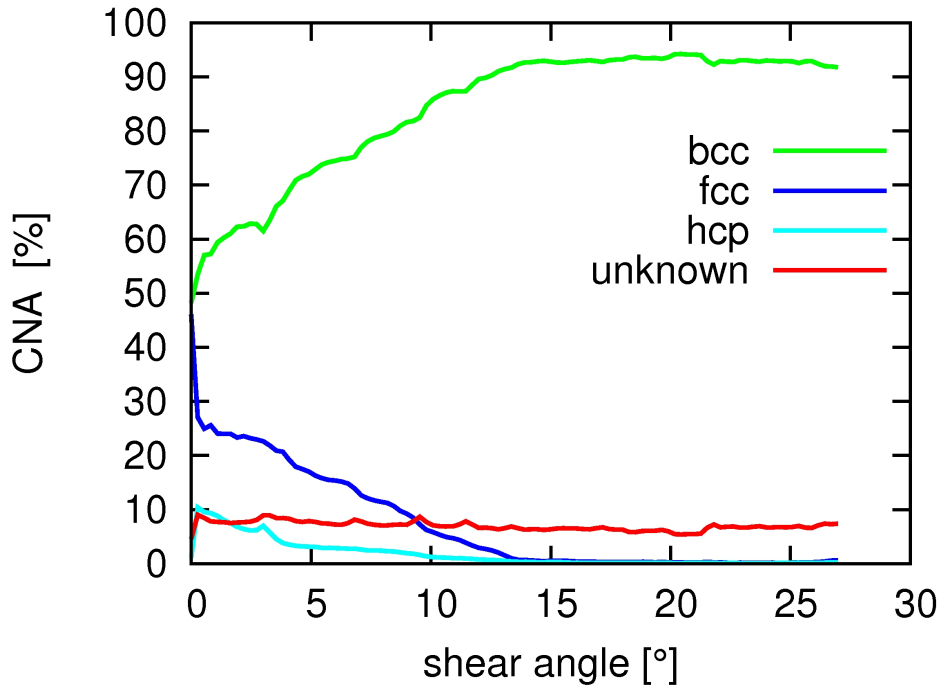

Figure 5.4: Evolution of the fractional phase content with shear angle, as detected by CNA, at a temperature of 300 K.

unidentified atoms amounts to roughly 10 %. This fraction increases initially due to the roughening of the moving interface.

5.2.2 Deformation at 400 K and 500 K

Figure 5.5 displays snapshots featuring the phase transition at a temperature of 400 K for shears up to the maximum shear angle. At small shear angles the phase boundary has already started to propagate; it continues its motion throughout the deformation, see Fig. 5.5(c)-(g). Simultaneously, an hcp grain nucleates in the bcc grain, see Fig. 5.5(b). With increasing shear deformation, the hcp grain transforms back to bcc. This intermittent emergence of the hcp phase within bcc can be explained by the action of two competitive mechanisms. (i) An increase of (hydrostatic) pressure favors the hcp phase, since it brings the system closer to the hcp phase in the equilibrium phase diagram of Fe, see Fig. 2.1. Since, in the NVT simulation, the pressure was not controlled during the shear deformation, high pressures appear in the simulation volume; a value of around 16 GPa is measured during the whole process. (ii) The shear deformation, which promotes the heterogeneous growth of the bcc phase, eventually predominates at large shear deformations. This explains why an hcp grain is temporarily formed which later transforms back to bcc.

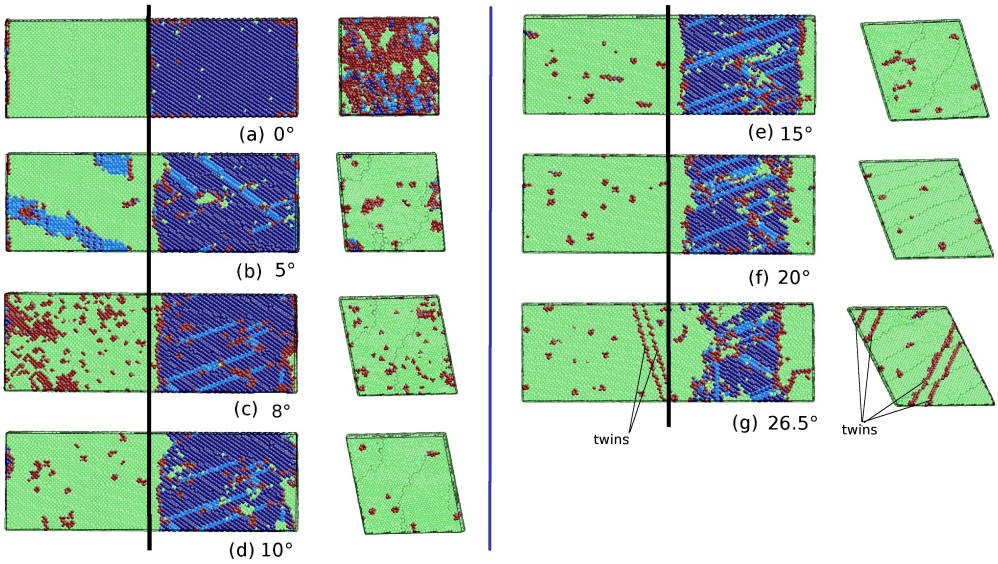

Figure 5.5: Snapshots showing the local structure of the fcc-bcc biphasic system at a temperature of 400 K for shear angles of up to 26.5°. The pictures on the left show the phase evolution in the y-z plane; The pictures on the right show the original interface plane (x-z plane) in the middle of the system. The colors denote the local atomic structure as in Fig. 5.2. The original interface position is marked by a black line. In (g), the twin boundaries are emphasized.

When the maximum shear angle is reached, the transition to bcc is not complete; there is still a rest austenite phase. This highly sheared sample is simulated for another 200 ps. The bcc phase increases by about 10 %. This suggests that the sample may transform completely after time long compared to the simulation time.

At 400 K, no homogeneous nucleation of the bcc phase is observed, in contrast to the above finding for the shear-induced phase transformation at 300 K. This may be explained by the fact that, at 400 K, the sample is already quite close to the transition temperature, hence the driving force for the homogeneous nucleation is smaller. Heterogeneous phase growth still proceeds, since heterogeneous nucleation is energetically more favorable than homogeneous nucleation, in which first a critical nucleus of the new phase must first be formed.

In the final sample, Fig. 5.5(g), twin structures are found. These do not form at any of other temperatures studied. They appear here because at this temperature the system transforms exclusively by interface motion; thus the largest bcc crystallite is created. Consequently, the strongest homogeneous stress state builds up at this temperature, and twin bands form, which are known to be an efficient means to relieve the high stress.

The fraction of each phase as a function of the shear angle was plotted in Fig. 5.6. The initial sharp decrease in the fcc phase is connected to a corresponding increase in the hcp phase, and is due to the formation of stacking faults in the fcc phase. As described in

detail above, the bcc phase transforms to hcp at a shear angle of about 5 °, and recovers at 10°. The concomitant slight increase in the fcc phase at these shear angles is due to the formation of fcc stacking faults in the hcp grain, cf. Fig. 5.5(b). Beyond a shear of 10°, the bcc phase increases steadily at the cost of the fcc phase; this is due to the steady propagation of the phase boundary. At maximum shear angle, a transformation degree of about 70 % is reached; As mentioned above, there is still a residual austenite phase in the system, which is composed of about 20 % fcc phase and 10 % hcp phase.

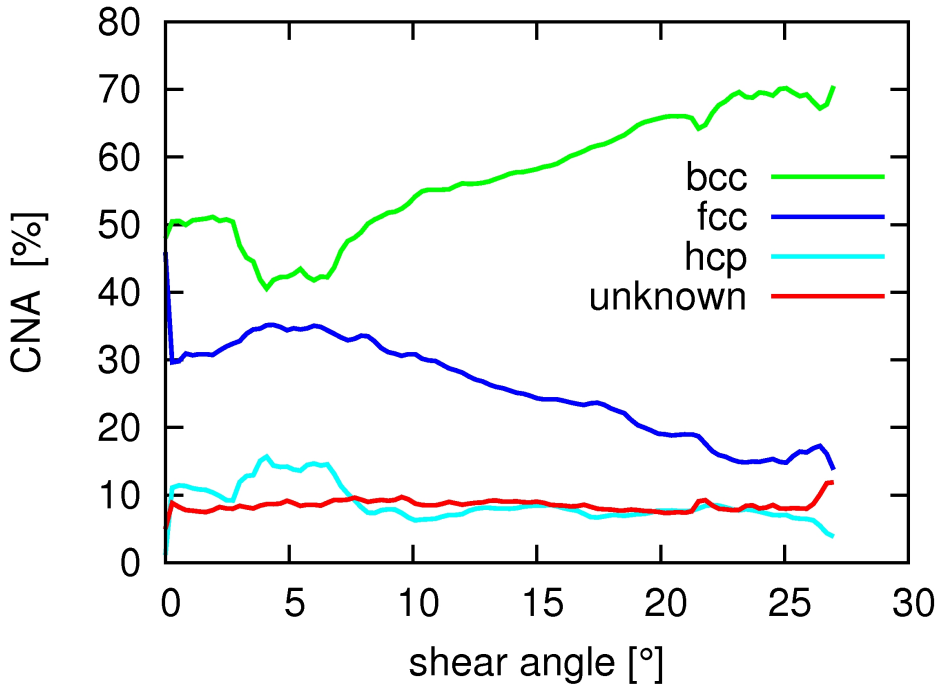

Figure 5.6: Evolution of the fraction phase content with shear angle, as detected by CNA, at a temperature of 400 K

Simulations were also performed at 500 K, close to the equilibrium transition temperature. No phase transition can be observed; neither homogeneous nor heterogeneous nucleation of the bcc phase occurred. The system remains stable. As mentioned in Section 3.6.3, the Meyer-Entel potential predicts a transition temperature of 550 $\pm$ 50 K at zero pressure. It is well known that the martensitic phase transition temperature decreases slightly with increasing pressure. Due to the build-up of hydrostatic pressure in the sample during shear deformation, the transition temperature decreases and assumes values of < 550 K.

5.2.3 Deformation at 600 K and 700 K

At a temperature of 600 K, which is above the transition temperature of the Meyer-Entel potential, a phase transition from the bcc phase to the close-packed (cp) phase is obtained;

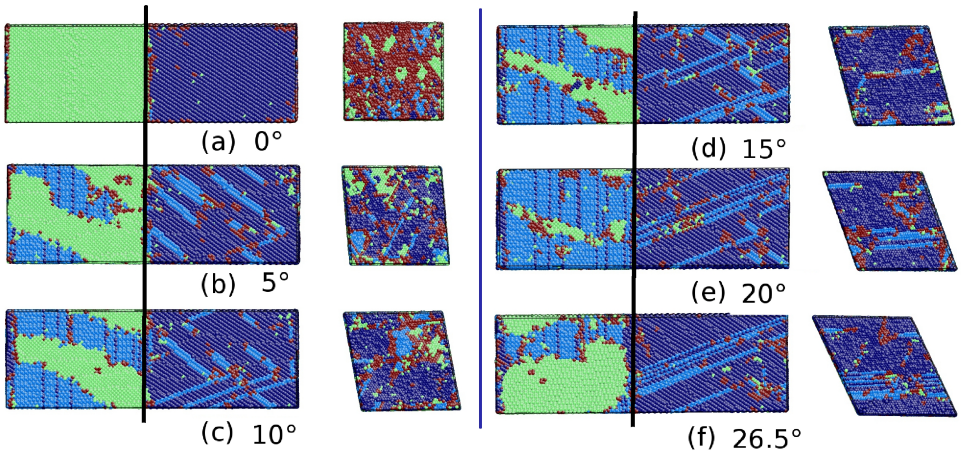

Figure 5.7: Snapshots showing the local structure of the fcc-bcc biphasic system at a temperature of 600 K for shear angles of up to $26.5°$. The pictures on the left show the phase evolution in the y-z plane; those on the right show the original interface plane (x-z plane) in the middle of the system. The colors denote the local atomic structure as in Fig. 4.2. The original interface position is marked by a black line.

due to the small difference in energies between the fcc and hcp phase, the austenitic phase transition at high temperatures usually results in a mix of both fcc and hcp structures (See subsection 4.2.2). Fig. 5.7 shows the local structure of the system as it evolves during the shear deformation. This interface remains immobile during the deformation. This is not surprising, as the applied shear deformation, see Fig. 5.1, drives the fcc $\rightarrow$ bcc transition but not the bcc $\rightarrow$ fcc transition. However, the process occurring in the homogeneous grains under shear are interesting. Already at shear angles of $< 5°$, the hcp phase has already nucleated in the bcc grain. It grows steadily up to shear angle of $20°$. The new phase contains stacking faults, which are detected as fcc layer. This bcc $\rightarrow$ hcp transition follows the Burgers orientation relations [107], which satisfy

$$(110)_{\mathrm{bcc}} \parallel (001)_{\mathrm{hcp}} \qquad \text{and} \qquad [110]_{\mathrm{bcc}} \parallel [110]_{\mathrm{hcp}}$$

see Fig. 5.9. Interestingly, for strains beyond $20°$, when the bcc grain has been almost entirely transformed, a back transition from the hcp to bcc phase takes place, see Fig. 5.7(f). The back-transformed bcc phase has the same orientation as the original one; this means that the back transition also satisfies the Burgers orientation relations. Sandoval *et al.* reported a similar back transition of the partly transformed bcc phase in a nanowire system under high tensile uniaxial stress [17].

In Fig. 5.8, the evolution of the fraction of each phase with increasing shear angle for the 600 K simulation is displayed. In contrast to the low temperatures studied above, the metastable phase (here bcc) does not start transforming immediately for small shear

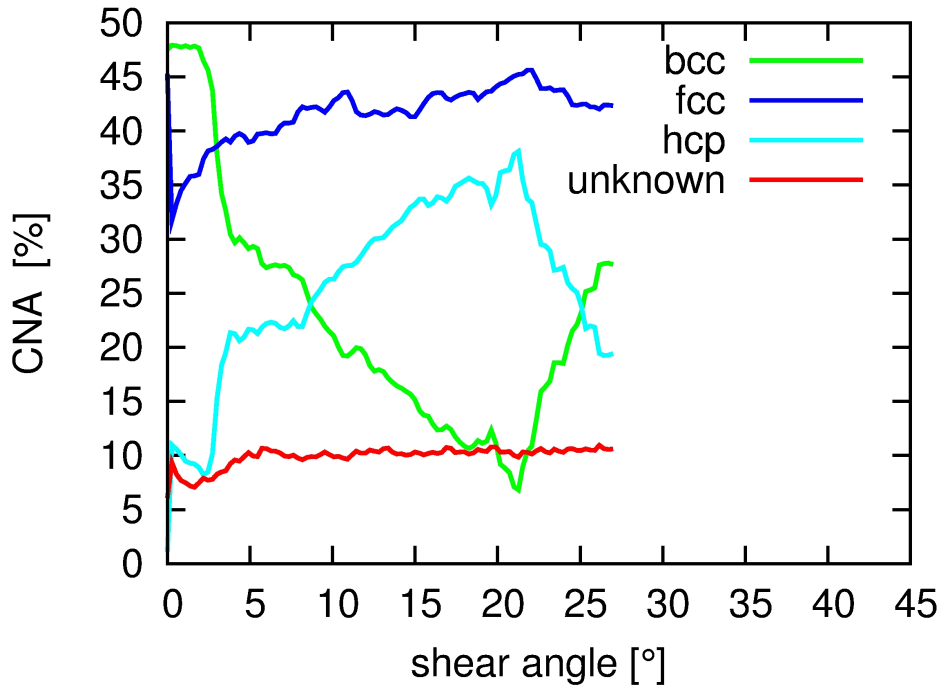

Figure 5.8: Evolution of the fractional phase content with shear angle, as detected by CNA, at a temperature of 600 K.

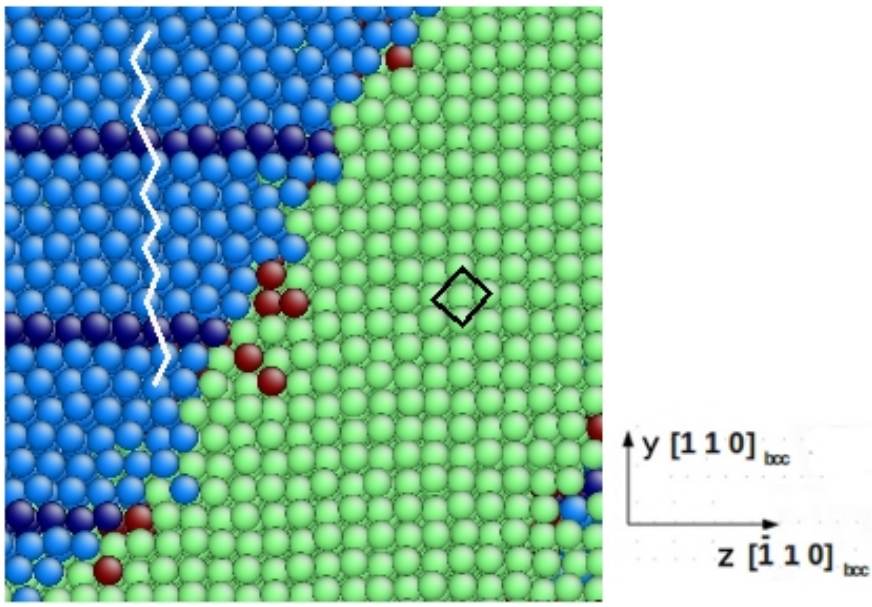

Figure 5.9: Close-up of the transforming area of Fig. 5.7(c), rotated by 90°. The slice shows the y-z plane of the transforming bcc area, which corresponds to a (001) bcc plane. The solid square denotes one unit cell in the bcc phase. The white line shows a stacking fault in the transformed hcp phase, which is detected as a single layer of fcc phase. The transformation obeys the Burgers orientation relationship: The hcp phase is obtained through opposite displacement of the (110) bcc planes, which are perpendicular to the y direction of the slice, plus a shear deformation in the [001] bcc direction.

strains; rather an incubation period is visible up to an angle of 2°. Such a behavior is characteristic for the relatively high energy barrier between the bcc and hcp phases; an analogous behavior of phase transition at temperatures above the phase transition temperature was found in the last chapter, see Subsection 4.2.3.

After the incubation stage, the bcc phase transforms steadily into cp phase up to a shear angle of 21°; the fractions of the fcc phase and in particular the hcp phase grow correspondingly. Beyond that shear angle of 21°, a back transformation from the cp phase (in particular hcp) to bcc is observed. This feature again emphasizes the role of the "magic" angle of 19.5°; a shear by this angle is characteristic of the N-W path for the fcc $\rightarrow$ bcc transition, see Fig. 5.1(a).

The shear-induced transformation was also simulated at 700 K. It turns out that the transformation process at this temperature is very similar to that at 600 K discussed above; featuring an incubation period, a steady bcc $\rightarrow$ cp phase transition up to angles of around of 21°, and the back transformation at larger angles. No motion of the phase boundary could be observed.

5.3 Conclusions

In this chapter, external shear strains were applied to the biphasic fcc/bcc system in the temperature range, where the system is (meta-) stable.

A strong temperature dependence of the strain-induced phase transformation was found. At low temperature, far below the equilibrium transition temperature of the Meyer-Entel potential [31], both heterogeneous and homogeneous growth of the stable bcc phase could be observed. Approaching the transition temperature, only heterogeneous growth was found at 400 K. This is in agreement with the reduced driving force for nucleating the stable phase. Above the transition temperature, the bcc phase transforms homogeneously to the cp phase. The interface does not move. Note that, in the absence of strain, the bicrystal is stable, at least in the time scales accessible in simulation.

These results thus exemplify how external strain acts as a driving force to trigger the bcc $\leftrightarrow$ fcc transformation and give detailed atomistic insight into the transformation dynamics and geometry. In addition, the results demonstrate how ambient temperature changes the response to the applied strain in a complex way and affects in particular the interplay between homogeneous and heterogeneous transformation paths.

Chapter 6

Competition of homo- and heterogeneous phase growth

It is well known that the growth of a new phase may proceed along two paths: by homogeneous phase nucleation, which starts inside the bulk material, and by heterogeneous growth, which starts from preexisting defects such as surfaces, grain boundaries or phase boundaries. The relationship and interplay between the homogeneous and heterogeneous growth processes are still under investigation. Huang and Browne [108] used a phase field modeling to describe the martensitic transformation in steel; they reported an increasing contribution of homogeneous nucleation away from the grain boundaries for high cooling rates. Jägle and Mittemeijer set up a kinetic model of random nucleation and grain-boundary nucleation [109] and studied the interface-controlled phase transformation [110].

In Chapter 4, the temperature-induced transformation in an Fe crystal containing an fcc/bcc N-W phase boundary was studied. In this chapter, this subject will be expanded by investigating the dependence of the transformation on the size of the transforming volume. In addition, the influence of the interface geometry on the phase transformation behavior will be studied; the N-W and K-S interface geometries will be investigated.

6.1 Methodology

Bicrystals with various sizes are employed in order to study the effect of crystal size. Setup of the bicrystal systems was described in Section 4.1. Bicrystals with an interface geometry either in N-W or in K-S geometry are used in order to study the effect of interface geometry. The biphasic system is depicted in Fig. 6.1 and detailed formations on the systems studied in this chapter are listed in Table 6.1.

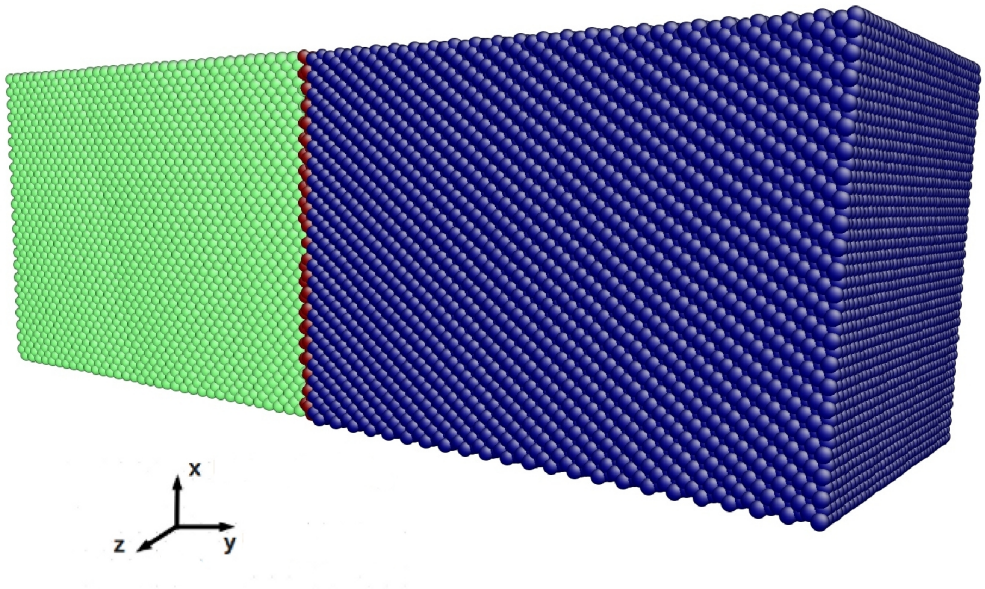

Figure 6.1: Setup of the biphasic system consisting of an fcc and a bcc crystallite. The dimensions of the picture correspond to system 2. The cartesian directions used in this study are indicated.

For the N-W geometry, 4 different systems are studied; these differ systematically in size and thus in the volume available for the transformation by a factor of up to 16. Note that only the interface area is changed; the width of the system normal to the interface is kept constant. In Chapter 4, the system 2 was used. Note that system 4 is exactly twice the system size of system 2 in x and z direction; for system 1 and 3, the exact proportions can only be kept on the fcc side, while the bcc side shows small deviations. As a consequence the strains and stresses at the interface show slight, but unsystematic, differences for the 4 systems. The total number of the atoms depends on the system size and is between 60 000 and 1 000 000.

Sys.	x (Å)	y (Å)	z (Å)	x^*_{bcc}	y^*_{bcc}	z^*_{bcc}	x^*_{fcc}	y^*_{fcc}	z^*_{fcc}	geo.	Rs.
1	50.37	284.93	49.86	17	35	12	19	67	11	N-W	1
2	100.74	284.93	99.72	35	35	25	38	67	22	N-W	4
3	151.11	284.93	149.58	52	35	37	57	67	33	N-W	9
4	201.48	284.93	199.44	70	35	50	76	67	44	N-W	16
5	104.69	284.93	98.70	21	35	28	25	22	22	K-S	1

Table 6.1: Systems (Sys.) studied in this chapter. x, y, z denote the length of the systems in the three cartesian directions, cf. Fig. 6.1. Lengths are indicated in Å and monolayers(*). Relative size (Rs.) gives the system volume and number of atoms relative to system 1. The crystal orientations are for fcc: x: $[1\bar{1}0]$, y :$[111]$, z :$[\bar{1}\bar{1}2]$; for bcc in N-W orientation: x: $[001]$, y: $[110]$, z: $[\bar{1}10]$; and for bcc in K-S orientation: x: $[1\bar{1}1]$, y: $[110]$, z: $[\bar{1}12]$.

Periodic boundary conditions should be employed in the simulations, the system has effectively two phase boundaries in the simulation volume (Fig. 6.1): the interface in the middle of the simulation system and an interface at the right-hand end, which is continued on the left-hand border due to periodicity.

The method of energy minimization by conjugate gradients is used (twice) to relax the system, details see Section 4.1. Note that the pressure perpendicular to the phase boundary drops from its initial high value and relaxes to < 20 MPa and the phase boundary structure has not been destroyed during the relaxation process. The interface structure after minimization for the N-W and K-S orientation relationship is displayed in Fig. 6.2.

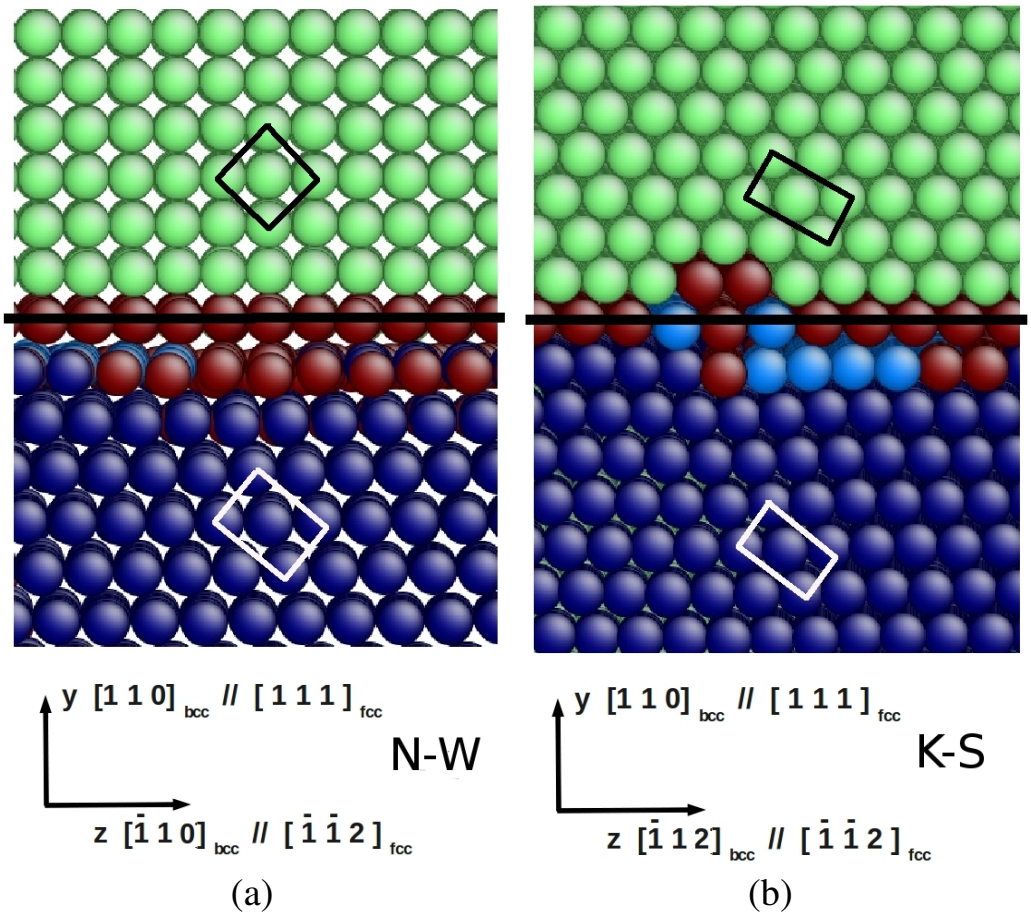

Figure 6.2: Cross-sectional view onto the y-z plane of the fcc-bcc interface. Colors denote the local crystal structure. Green: bcc; dark blue: fcc; light blue: hcp; red: unknown. (a) N-W phase boundary for system 2 (b) K-S phase boundary for system 5.

After the systems have been constructed, the simulations are performed in NPT ensembles with periodic boundary conditions. The pressure is controlled via a Nosé-Hoover barostat which is set to zero pressure. Indeed, it is found that the pressure decreases within the first 5 ps of the simulation in all three directions to the values in the MPa region. The temperature is controlled via a Nosé-Hoover thermostat. The

simulations are performed at two temperatures as in Chapter 4: at a low temperature of 100 K and at a high temperature of 1300 K; these values are considerably below and above the transition temperature of the Meyer-Entel potential, which is used for the simulations, respectively.

The local structure identification is performed through the common neighbor analysis (CNA) [52]. The interface velocity is determined as the average from 5 different time steps during the interface motion. It is calculated as the quotient of the current interface position and time. Due to the roughness of the phase boundary, 10 maximum and 10 minimum positions of the interface atoms (based on their local lattice structure) are determined and used for averaging.

6.2 Results and discussion

6.2.1 N-W geometry: martensitic transformation

At temperature of 100 K, the biphasic system transforms spontaneously to the bcc phase. Details of the transformation process of the smallest (system 1) and the largest (system 4) are shown here. Note that the transformation of system 2 has been discussed in detail in chapter 4; it is characterized by the simultaneous homogeneous and heterogeneous phase growth of the bcc phase. When interface motion is discussed, here and in the following, the motion of the interface in the middle of the displayed simulation cell should be focused on, unless otherwise noted.

Figure 6.3(a) shows the state of the biphasic crystal immediately after relaxation. The relaxation process has already created a number of defects, primarily on the fcc side, but also on the bcc side. This is due to the high stress and strain exerted by the interface and demonstrates the difficulty of preparing this interface system.

The evolution of system 1, Fig. 6.3, features the homogeneous phase nucleation in the original fcc crystal, see Fig. 6.3(b), followed by a rapid transformation of the right hand part of the fcc grain, which is completed at around 20 ps. The formed bcc material exhibits still a high number of defects, which however gradually anneal out. Note the red lines in the transformed bcc material appearing in Fig. 6.3(c)-(f), which delineate stacking faults; the material at both sides of these defect planes has the same crystallographic orientation. Simultaneously, also the phase boundary displayed in the middle of the snapshots starts roughening and then moving into the original fcc grain. Finally, at 35 ps, a narrow stripe of residual austenite remains as a stable grain boundary between the original and the newly formed bcc grains, since their orientations are different.

In system 2 and 3, the mechanism of the phase transition is similar as in system 1: They exhibit both heterogeneous and homogeneous phase growth. The snapshots for these

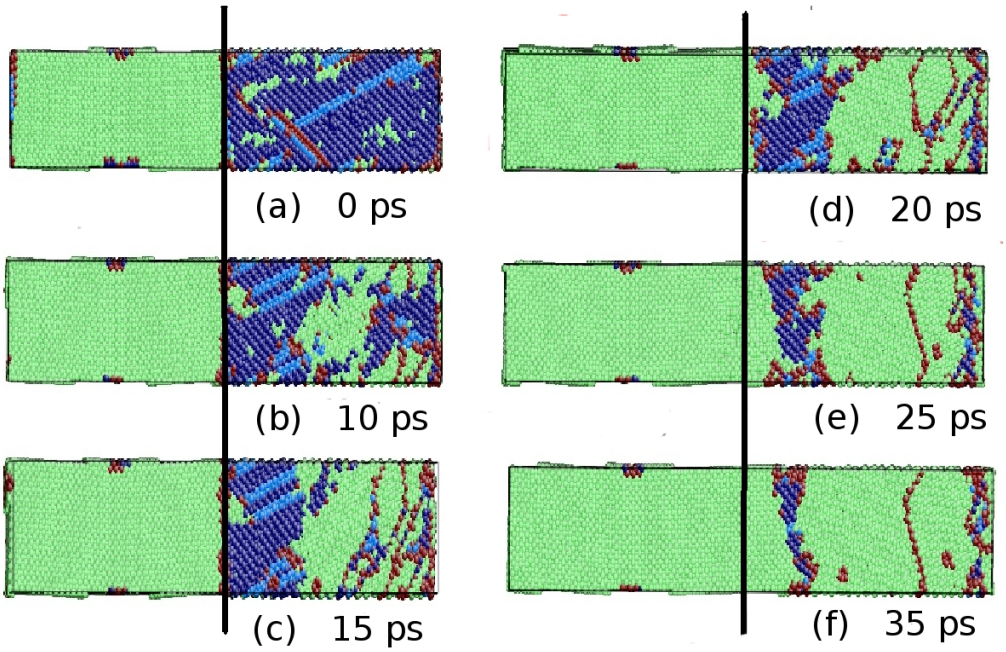

Figure 6.3: Snapshots showing the time evolution of the fcc → bcc transition in system 1 (N-W interface) at 100 K. The original position of the interface is marked by a black line. Colors denote the local crystal structure as in Fig. 6.2

two systems are not presented. Detailed information on system 2 has been described in Chapter 4.

Figure 6.4 displays the snapshots of the phase transition in system 4, the biggest system. The transformation of this system is dominated by the homogeneous nucleation of the new phase; the original phase boundaries stay rather immobile. Heterogeneous phase transformation does not take place. The bcc phase nucleates homogeneously in the fcc grain in a statistical way, see Fig. 6.4(a) and (b). Almost the whole fcc grain has transformed into bcc phase within 50 ps.

In Fig. 6.5, the interface motion is analyzed. Fig. 6.5(a) presents the position of the phase boundary in the first 35 ps for system 1-4; Note that the data base on the phase boundary shown in the middle of the snapshots. The interfaces in the first three systems move continuously towards the fcc side, while the interface in system 4 (biggest system) fluctuates around the original position. The interface moves most for the smallest systems. The interface velocity over the first 35 ps is averaged and presented as a function of system size in Fig. 6.5(b). The interface velocity shows a distinct dependence on system size: It decreases with increasing size of the system. These results quantify the finding that heterogeneous phase growth loses its importance for larger systems. The physical reason hereto is that the larger available volume for homogeneous phase growth makes this growth channel more important, as new nuclei have a higher chance to form and grow in larger volumes. Note that the length in y direction (i.e., the thickness of the

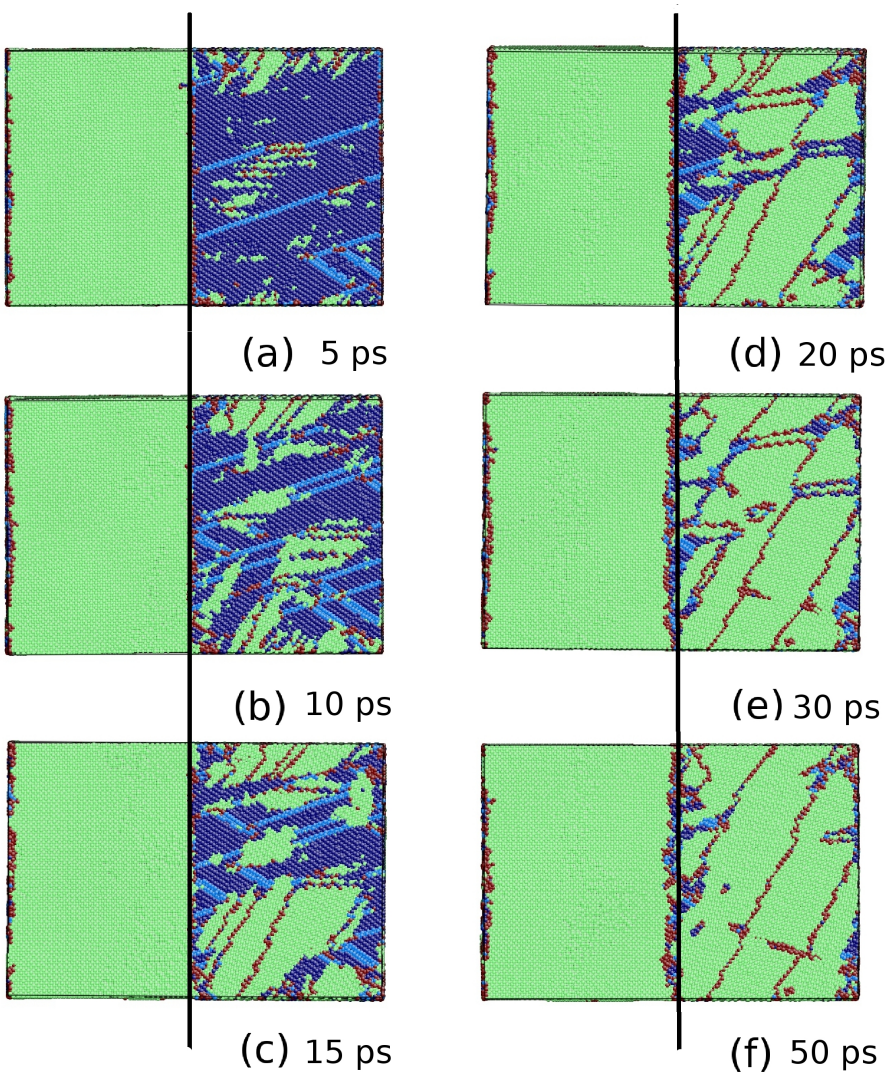

Figure 6.4: Snapshots showing the time evolution of the fcc → bcc transition in system 4 (N-W interface) at 100 K. The original position of the interface is marked by a black line. Colors denote the local crystal structure as in Fig. 6.2

phases) remains the same in the systems; only the lengths parallel to the interface change. However, system size makes a difference even in periodic boundary conditions: Larger nuclei can form independently only in a sufficiently large volume. This is a typical finite-size effect of first-order phase transformations. The formation of large nuclei is illustrated in Fig. 6.9(c) in Subsection 6.2.2 - such a nucleus cannot exist in a small system.

The data on the interface velocity have to be used with care. Firstly, the considerable roughness of the interface allows one only to determine the spatial average over the interface position. Secondly, the interface does not propagate smoothly in the simulations; rather there are periods where the interface does not move forward and after this incubation time, the interface jumps suddenly forward. Finally, there is a competition between homo- and heterogeneous growth; interface motion may be hindered by the growth of

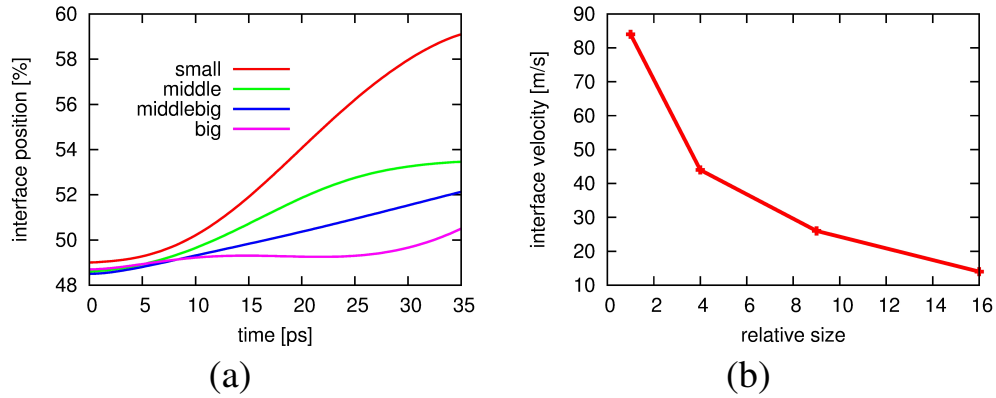

Figure 6.5: (a) Temporal evolution of the interface position in the first 35 ps for system 1-4. The original position of the interface in y direction(perpendicular to the phase boundary) has been set to 0. (b) Interface velocity averaged over the first 35 ps as a function of system size. The system size is given relative to the smallest system, system 1, cf Table 6.1.

the homogeneously nucleated phase, not only energetically (because the driving force for phase transformation may be decreased), but also spatially, if nuclei of the new phase have been formed nearby an interface.

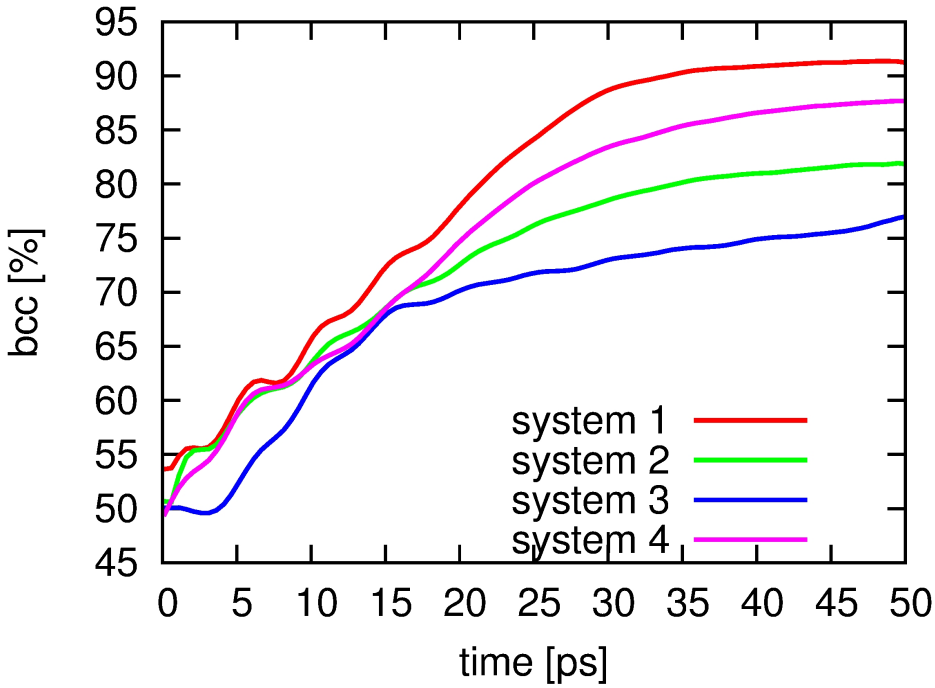

Figure 6.6: Temporal evolution of the fractional bcc content for various system size, as evaluated by common neighbor analysis (CNA). Data taken at a temperature of 100 K for the bicrystal in N-W geometry

While Fig. 6.5 quantified the heterogeneous phase growth, the total fraction of newly formed bcc material is shown in Fig. 6.6. These data thus sum the results of the transformation, irrespective of whether the new phase has been formed by homogeneous nucleation or by interface motion. In the first 15 - 20 ps, the relative rate of the formation of the new phase is rather constant for the 4 systems. Then the systems saturate at different maximum levels of transformed material; interestingly, the smaller systems show a higher maximum transformation degree. An inspection of snapshots of the final state of system 2 and 3 (not shown here) shows that in these systems, the original fcc and now transformed bcc grain is still surrounded by rather thick grain boundaries consisting of untransformed residual austenite, see Subsection 4.2.2. In the largest system 4, again a high transformation degree is achieved. Note that, in this big system, the transformation proceeds essentially entirely via homogeneous nucleation, and interface motion contributes only little, see Fig. 6.5. The homogeneous transition lost its "competitor" and thus exhibits an accelerated transition speed.

As noted above, the interfaces create local stresses and even misfit dislocations. It can not be excluded that these play a role in the transformation speeds. However, since the stress state varied in an unsystematic way between the systems, its influence will also be not systematic.

6.2.2 N-W geometry: austenitic transformation

In this subsection, the austenite bcc $\rightarrow$ fcc transition at high temperature of 1300 K will be discussed. The results for systems 1, 3 and 4 should be presented, since they all exhibit slightly changed behavior.

The smallest system 1 is presented in Fig. 6.7. The whole phase transformation of the original bcc grain is finished within 30 ps; it results in a completely transformed mixture of fcc and hcp phase material [close-packed (cp) phase]. Note that the difference between the fcc and hcp phase is quite small, around 4 meV/atom [69]. Small fluctuations of temperature or stress can cause the transition between them. Thanks to its small size, system 1 provides the possibility of studying the mechanism of the complex phase-boundary motion in detail. The nucleation starts at the left-hand border of the simulation box, see Fig. 6.7(a). Note that, due to the periodic boundary conditions, there is also a phase boundary at the left-hand side border. The nucleated cp phase grows finger-like into the simulation box, Fig. 6.7(b). In Fig. 6.7(c), the phase boundary in the original bcc grain has assumed a complex structure which may be called dendritic. After that, the dendrites grow in thickness, i.e., in vertical direction in Fig. 6.7(c). After the transformed cp grains have joined, only small pockets of original bcc material are left over and slowly continue transforming, Fig. 6.7(d)-(f).

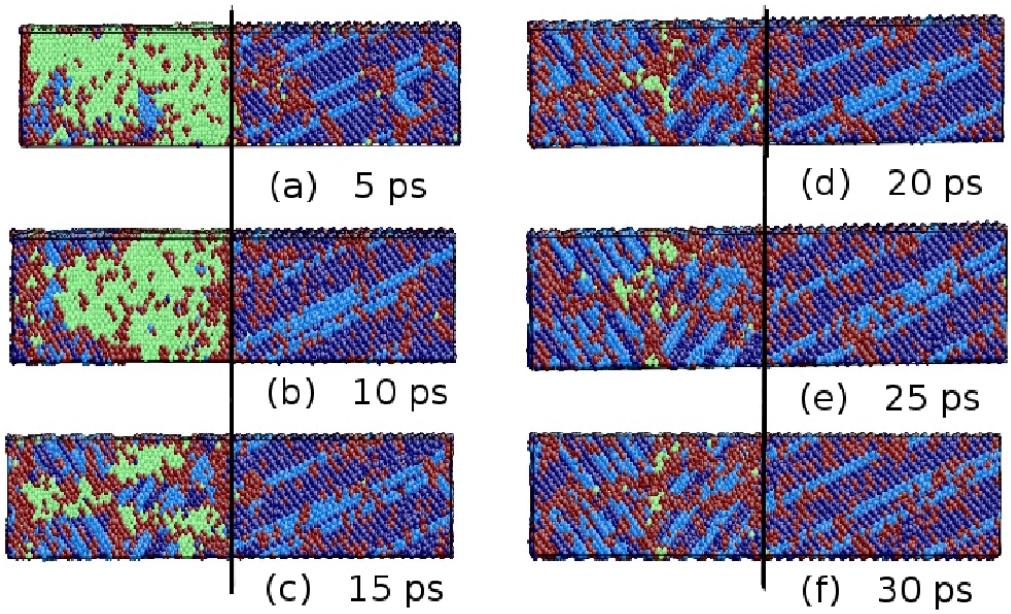

Figure 6.7: Snapshots showing the time evolution of the bcc → fcc transition in system 1 (N-W interface) at 1300 K. The original position of the interface is marked by a black line. Colors denote the local crystal structure as in Fig. 6.2.

The details of the austenitic phase transition in system 2 at high temperature have been presented in Subsection 4.2.3: This system features only the heterogeneous transformation of the bcc phase into the cp phase, i.e., the new cp phase is established mainly through the propagation of the phase boundary. System 3 behaves similar and is presented in Fig. 6.8. Note the incubation time of at least 15 ps where the transformation does not start, neither by formation of a nucleus nor by interface motion. Then, quite suddenly at 15 ps, the middle and the left-hand interface start moving towards each other, transforming the enclosed bcc grain up to a narrow gap at 20 ps; even this has closed at 25 ps, at which time the transformation is over. Note the formation of a pronounced twin structure in the transformed cp material, see Fig. 6.8(e) and (f). This twin structure is not unexpected: Engin and Urbassek [96] reported an analogous structure in their study of the martensitic phase transition in iron by using the Finnis-Sinclair potential; in that case the twin structures developed while an initial fcc crystallite (no phase boundaries) transformed spontaneously to bcc. The origin of the twin formation is the reduction of (shear) stress in the transforming system. Since the new phase has a lattice mismatch with the old phase, the continuous growth of a single grain of new material will lead to ever increasing stresses; twinning changes the orientation relationship of the grains of the newly forming phase in such a way as to relieve stress.

System 4, presented in Fig. 6.9, exhibits a slightly changed transformation behavior. At 5 ps, a large cp nucleus is formed which spans the entire bcc grain parallel to the interface. This nucleus is, however, not stable; it fluctuates strongly in size, until at 25 ps,

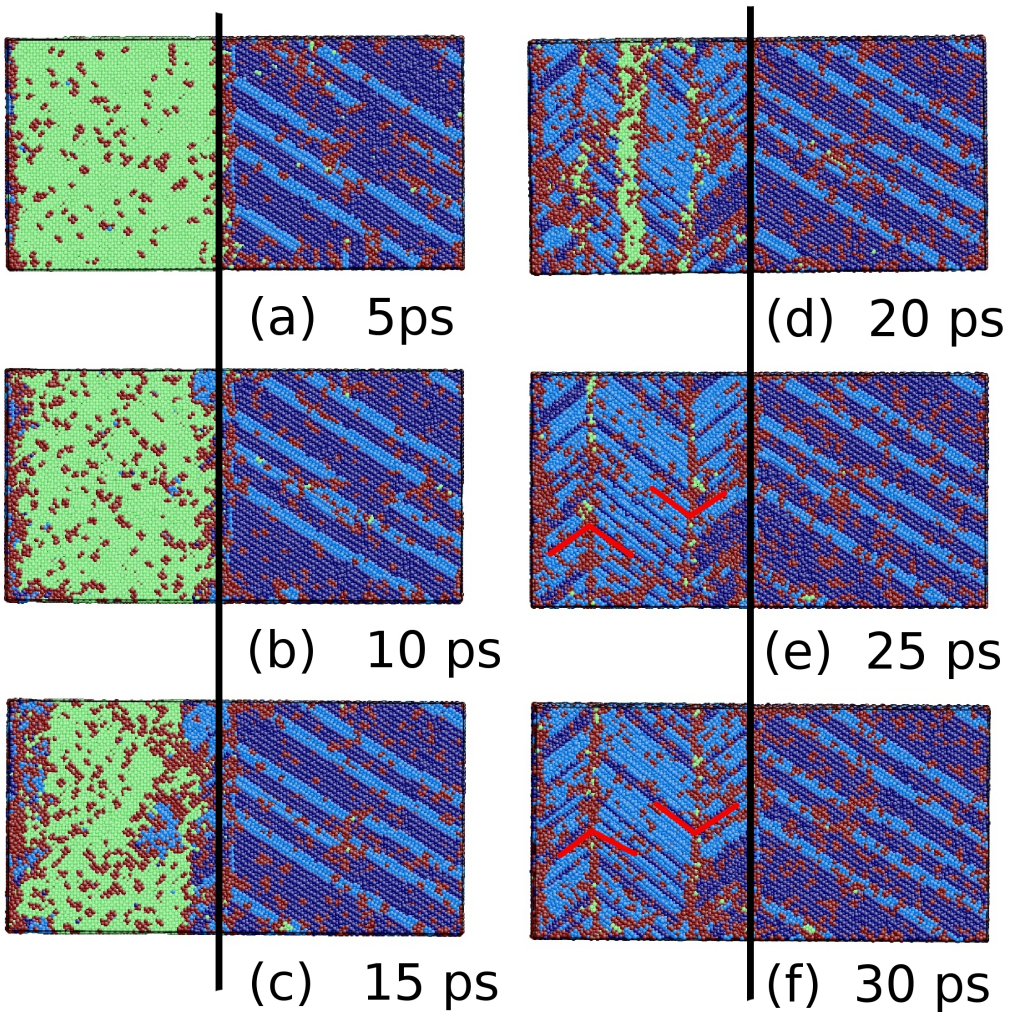

Figure 6.8: Snapshots showing the time evolution of the bcc → fcc transition in system 3 (N-W interface) at 1300 K. The original position of the interface is marked by a black line. Colors denote the local crystal structure as in Fig. 6.2. The red lines in (e) and (f) mark the twin structure in the transformed cp phase.

2 nearby nuclei have been created; at this time the bcc phase fraction is already down at 15 %. Shortly afterwards, the left-hand phase boundary starts moving, see Fig. 6.9(d) and (e). Also the two nuclei grow quickly, presumably due to the considerable roughness of their interface. The interface in the middle of the system remains stationary and does not move. Fig. 6.9(d) and (e) show nicely how the presence of homogeneously formed nuclei hinders the motion of the interface: While the interface in the middle of the system, which is very close to one of the nuclei, does not move, the left-hand interface, which is at some distance of the nuclei, moves towards them; also this interface stops moving as soon as it touches its neighboring nucleus. Finally, at 40 ps, it appears a mixture of heterogeneously and homogeneously transformed cp phase; they have different crystal orientations. This simulation was continued for another 100 ps, but a reorientation of the transformed grains could not be observed.

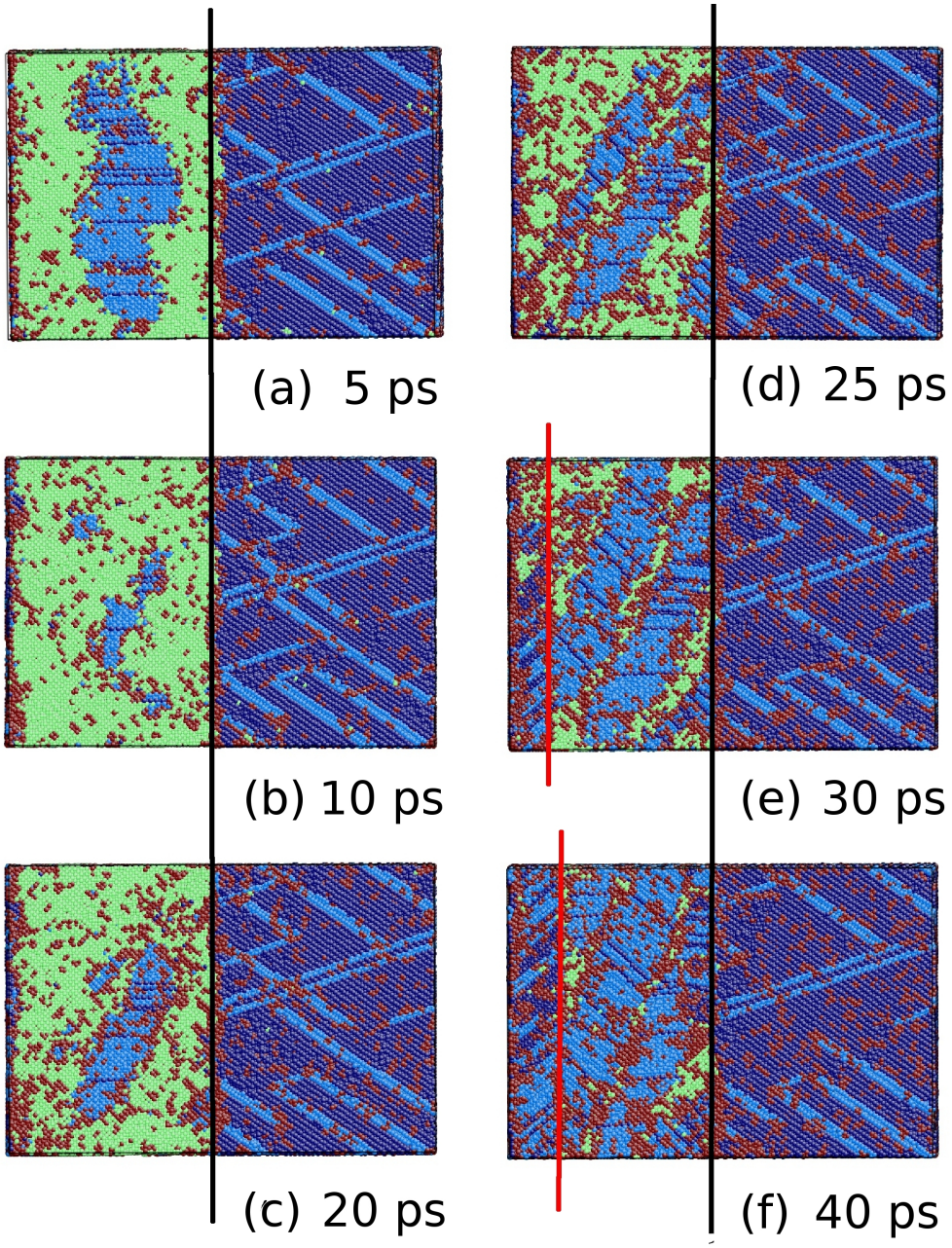

Figure 6.9: Snapshots showing the time evolution of the bcc → fcc transition in system 4 (N-W interface) at 1300 K- The original position of the interface is marked by a black line. Colors denote the local crystal structure as in Fig. 6.2. The red lines indicate the current positions of the interface which moved from the left-hand boundary into the original fcc crystallite.

It is hard to analyze the interface velocity for the high-temperature phase transformation for several reasons: (i) In this transformation, highly ragged interface contours appear. In particular, system 1 shows a dendritic interface structure. The considerable roughness of such interfaces prevents determining the current interface positions. (ii) In system 2-4, long incubation times of about 25 ps are observed before the interfaces start moving; then

rapid motion occurs. Averaging over such inhomogeneous data appears inappropriate. (iii) Compared to the relatively smooth propagation of the interface observed at the low-temperature martensitic transformation, the interfaces move rather abruptly and erratically at high temperature. Again, this leads to difficulties for identifying the current interface positions.

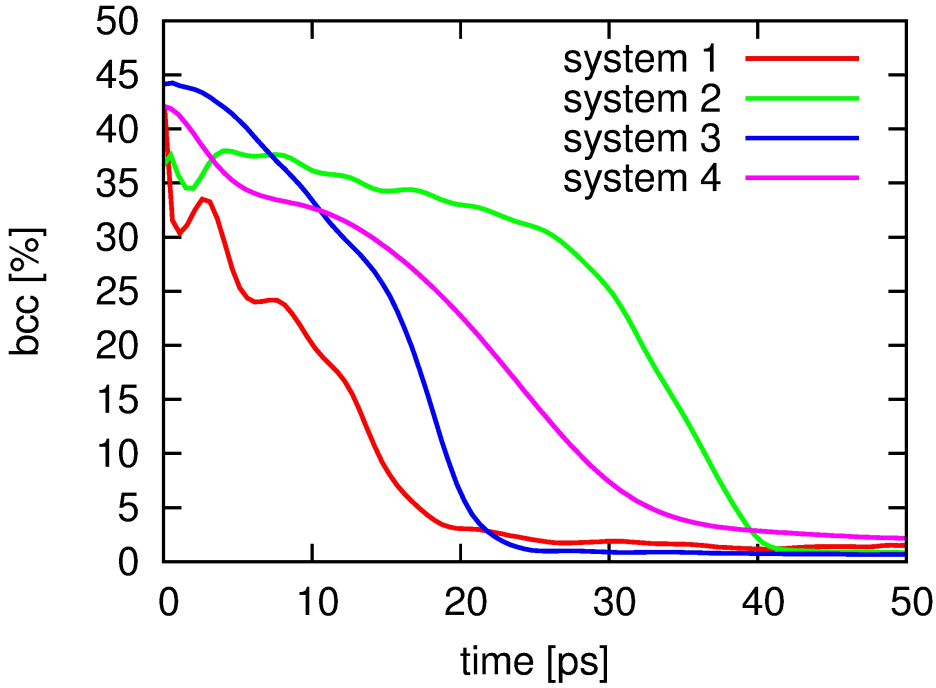

Figure 6.10: Temporal evolution of the fractional bcc content for various system sizes, as evaluated by common neighbor analysis (CNA). Data taken at a temperature of 1300 K for the bicrystal in N-W geometry.

However, it is more straightforward to analyze the transformation rate by determining the bcc fraction still contained in the samples. Fig. 6.10 shows the time evolution of the bcc fraction as a function of system size. The CNA detector does not operate so efficiently at high temperature for the interpretation of the data, since it is based on the distance of atom pairs and this is smeared out by atomic vibrations, see Appendix A. As a consequence the fraction of unidentified atoms increases while that of well identified phases decreases. Nevertheless, trends may be read off Fig. 6.10.

(i) A lower transformation rate in the first 25 ps is clearly seen for system 2, and to a lesser degree also for system 3 and 4. Note that, due to the inefficiency of the CNA detector at high temperatures, the plateau expected during the incubation period is smeared out since bcc atoms are misinterpreted as unidentified, cf. e.g., Fig. 6.8(a) and (b).

(ii) Towards the end of the transformation, system 2 and 3, and also system 1 at the time window between 15 and 20 ps, feature rather high transformation rates (steep decays). This features the phase of rapid interface motion after the incubation period and the formation of the twinned cp phase.

(iii) System 4 shows a slower transformation rate. This is a sign of the occurrence of homogeneous nuclei in the metastable bcc phase which hinder the motion of interface and thus eventually slow down the transformation process.

6.2.3 K-S geometry

In this subsection, the influence of the interface geometry on the martensitic and austenitic phase transition process will be discussed. To this end a biphasic crystal with a K-S interface is used and compared with the corresponding results for the N-W geometry. Since system size is not in the focus of this section, the K-S system 5 should be only compared to the system 2, which has the same size.

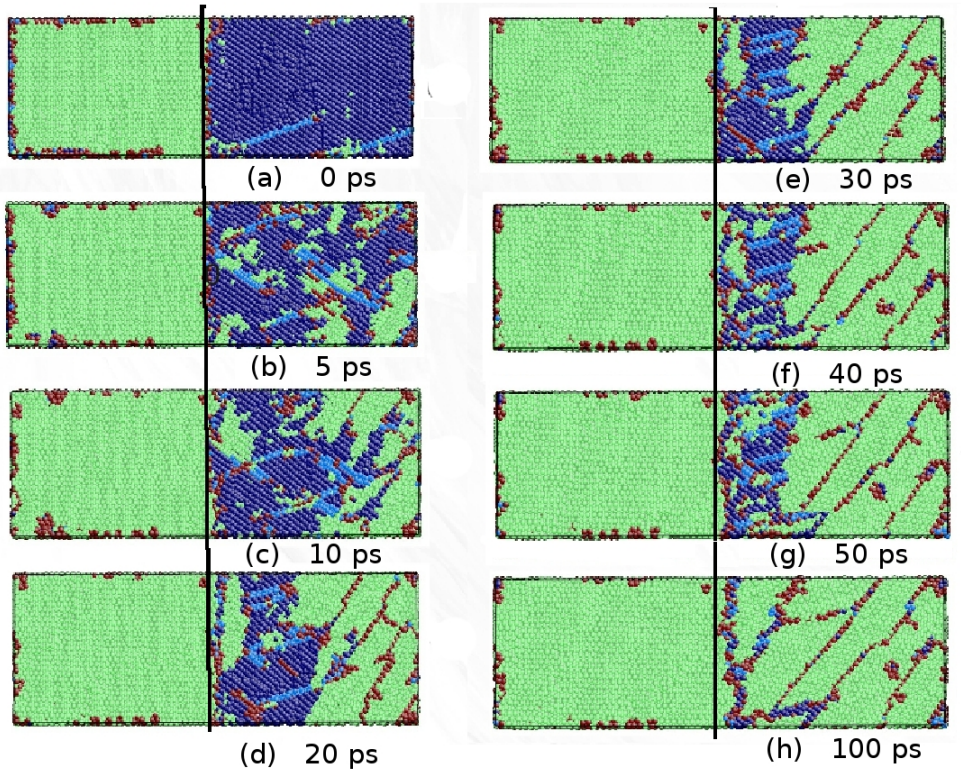

Figure 6.11: Snapshots showing the time evolution of the fcc → bcc transition in system 5 (K-S interface) at 100 K. The original position of the interface is marked by a black line. Colors denote the local crystal structure as in Fig. 6.2.

The time evolution of the martensitic transformation is displayed in Fig. 6.11. The transformation is dominated by homogeneous nucleation; many nuclei form quickly and

simultaneously in the fcc grain, which thereafter decomposes quickly. The bcc phase nucleated statistically in the fcc grain, see Fig. 6.11(b). Heterogeneous phase growth is not observed. The simultaneous nucleation of many grains leads to the formation of many stacking faults in the new bcc phase, which are identified as the red lines running diagonally through the snapshots. Rather quickly, after around 20-30 ps, the original fcc phase has shrunk to a narrow slab bounded by a new, almost planar interface on the right-hand side, Fig. 6.11(d)-(g). After 100 ps, this fcc slab has disappeared; only "residual austenite" phase in thickness of 2 monolayers has remained and forms a defect in the surrounding bcc crystal, Fig. 6.11(h).

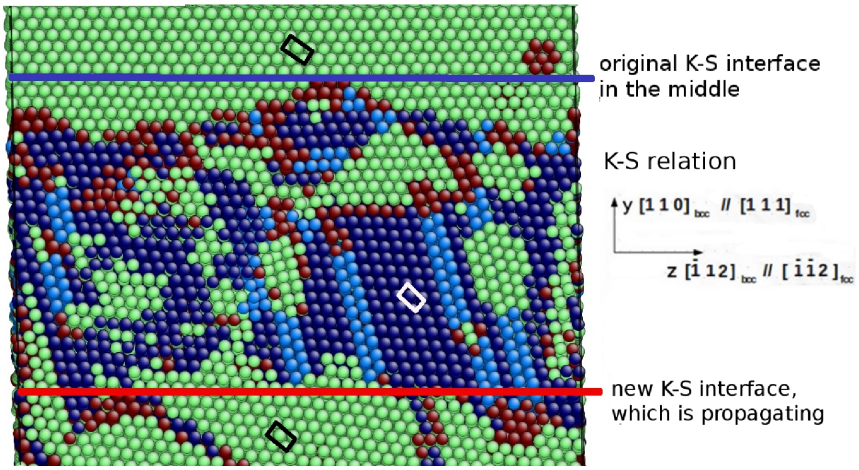

Figure 6.12: Close-up into Fig. 6.11(f), rotated by 90°. The blue line denotes the original K-S interface in the middle of the system, which does not move. The red line shows the new K-S interface, which has formed after homogeneous nucleation of the bcc phase in the fcc grain. The black rectangles show the body centered tetragonal (bct) lattice cells in the bcc phase, and the white rectangle indicates one bct lattice cell in the original fcc phase. Colors denote the local crystal structure as in Fig. 6.2.

Remarkably, the multiple heterogeneous nucleation does not lead to bcc grains with different orientations; rather the transformed bcc material has the same orientation as the original bcc crystal; rather than grain boundaries, only stacking faults exist in the transformed phase. This is demonstrated further in Fig. 6.12, where the transforming crystal structure is zoomed and the orientation relation between the newly formed and the original bcc phases is analyzed. Indeed the two crystallites have exactly the same crystal orientation; thus also the newly formed fcc-bcc interface satisfies the K-S orientation relationship.

Figure 6.13 displays the time evolution of the fractions of each phase in system 5. The massive increase of the bcc phase in the first 25 ps is due to the homogeneous bcc nucleation and its ensuing growth in the fcc grain, cf. Fig. 6.11(b)-(d). After 25 ps, the bcc phase growth decelerates. Compared to the N-W system (Fig. 6.6, system 2), the K-S system thus exhibits a slower transformation speed. The reason for the slower growth is

the absence of the heterogeneous transformation mode, which governed the N-W interface system. The fraction of the hcp phase remains below 10 % in this case; this small amount of hcp phase can be considered as stacking fault defects in the original fcc grain.

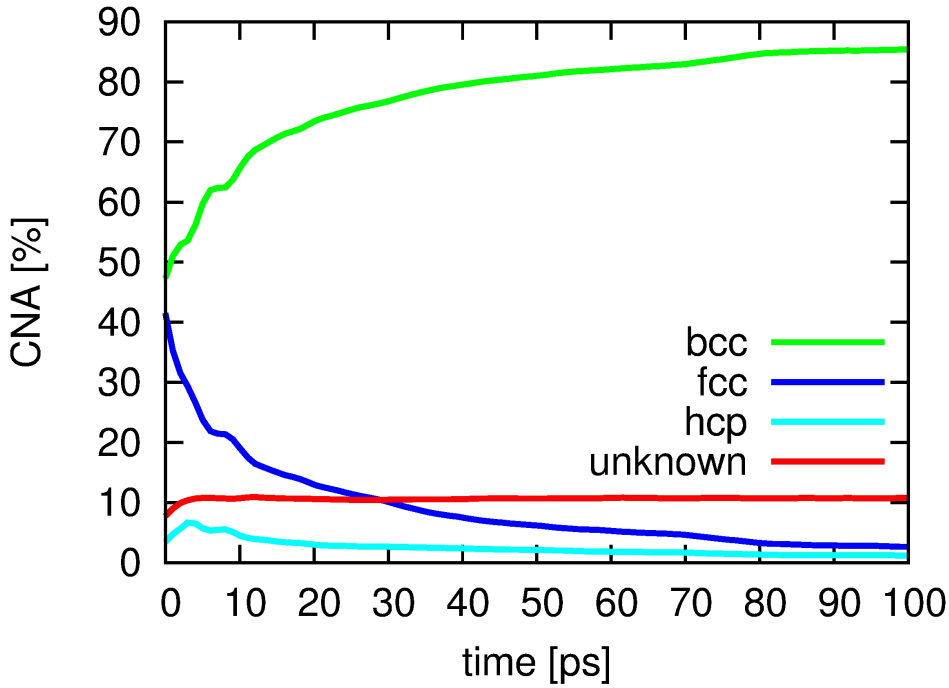

Figure 6.13: Temporal evolution of the fractional phase content for system 5 (K-S geometry), as evaluated by common neighbor analysis (CNA). Data taken at a temperature of 100 K for system 5 (K-S geometry).

Now the high-temperature austenitic transformation in the K-S system is analyzed. Fig. 6.14 displays snapshots for the transformation process at a temperature of 1300 K. Again the transformation starts quickly. Already at 10 ps, the small fcc nuclei which have formed join up with the existing fcc grain. Thus a complex interface structure is formed, see Fig. 6.14(d), in which the remaining bcc phase only survives in small pockets. The evolving complex interface looks rather similar to the dendritic interface growth reported by Tateyama *et al.* [97] for the K-S interface geometry, albeit for the low-temperature fcc $\rightarrow$ bcc transformation. Note in particular how the existing fcc dendrites in Fig. 6.14(c) spread sideways rather than growing in length before they combine in Fig. 6.14(d) between 10 and 20 ps. After the rapid transformation phase, which is terminated at 20 ps, the remaining narrow bcc pockets turn out to be rather stable and diminish only slowly.

The temporal evolution of the fraction of each phase is displayed in Fig. 6.15. The figure quantifies how rapidly the bcc phase decreases and forms the cp phases. The initial drop of the fcc phase is due to the formation of the hcp phase in the original fcc grain; it can be interpreted as stacking fault planes, cf. Fig. 6.14(b). After about 50 ps, the bcc

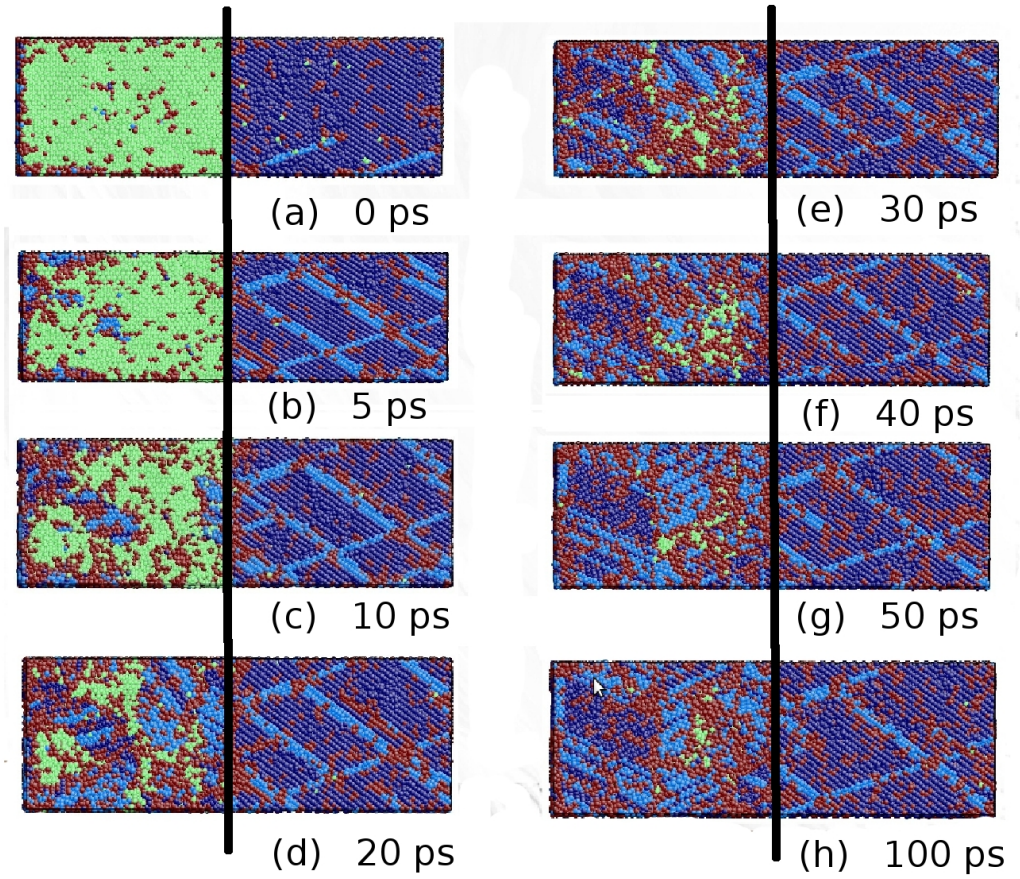

Figure 6.14: Snapshots showing the time evolution of the bcc → fcc transition in system 5 (K-S interface) at 1300 K. The original position of the interface is marked by a black line. Colors denote the local crystal structure as in Fig. 6.2.

fraction falls below 2 %. Note that the fraction of unidentified atoms is quite high; after 20 ps it is around 40 %. The reason for the high percentage of unidentified atoms lies mainly in the high temperature; as mentioned above, the thermal vibration of the atoms deteriorates the efficiency of the CNA detector, see Appendix A.

The interface velocity of the K-S system will not be analyzed. Firstly, at low temperature, the propagating interface is not the original one, but is newly formed after the homogeneous nucleation of bcc crystallites in the original fcc grain. Secondly, the huge roughness (needle-like growth) of the interface at high temperature makes the determination of the interphase position impossible. However, the time evolution of the growth of the bcc phase content show in Figs. 6.6, 6.10, 6.13 and 6.15 makes it possible to compare the phase transformation speeds in systems with N-W and K-S geometry. It can be concluded that the phase transition in the N-W system is faster than that in K-S system, not only at low temperature, but also at high temperature. Tateyama *et al.* [97] compared the bcc phase growth in the martensitic transformation of a biphasic Fe system

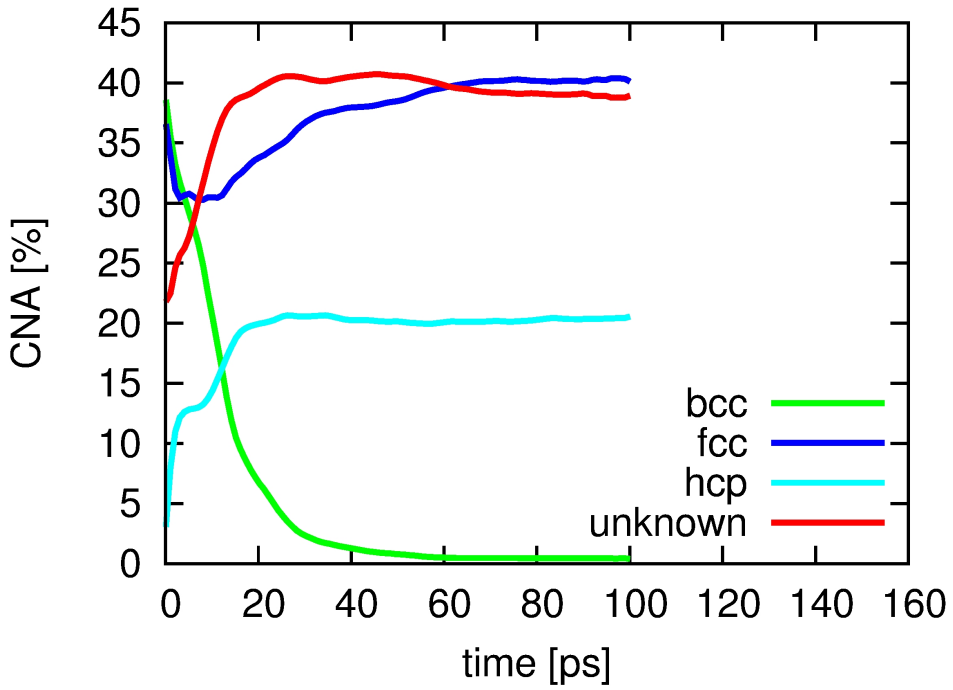

Figure 6.15: Temporal evolution of the fractional phase content for system 5 (K-S geometry), as evaluated by common neighbor analysis (CNA). Data taken at a temperature of 1300 K for system 5 (K-S geometry).

under N-W and K-S geometry; they reported a higher velocity of the planar interface propagation for the N-W interface than for the K-S interface.

6.3 Conclusions

In this chapter, the competition of homo- and heterogeneous phase growth in dependence of system size was studied in biphasic Fe systems. Two temperatures (100 and 1300 K) were investigated. In general, both homogeneous phase nucleation and heterogeneous phase growth by interface motion contribute to the phase transition. These two mechanisms are competitive in that the creation of nuclei in the bulk phase (homogeneous nucleation) hinders the interface motion (heterogeneous nucleation), and vice versa. In detail, the following results were obtained.

The martensitic phase transformation proceeds both via homo- and heterogeneous phase growth. During growth the interface roughens. While for the N-W geometry, the interface still has a globally planar form, it assumes a dendritic growth structure for the K-S geometry. In addition, a clear influence of the growth mode on the available volume has been seen: With increasing volume homogeneous growth dominates over heterogeneous growth. This is most easily seen by a decrease of the interface velocity during growth. The

physical reason behind this behavior is that the formation of a nucleus of the new phase, which is needed for homogeneous growth, is facilitated if a larger volume is available.

For the austenitic transformation, a similar but even more drastic behavior was observed. While in small volumes, homogeneous nucleation of the new phase was not seen at all, in the largest systems studied, stable nuclei may be generated and contribute to phase growth. For the K-S geometry, which was studied only for a moderate system size, only phase growth by interface motion was observed; the interface shows again a dendritic structure.

These results are relevant for future studies of phase transformation both form a physical and a methodological point of view. They show that not only in nanoscale systems,but also in bulk systems, in which the volume available for transformation has been restricted by the existence of microstructure such as grain boundaries, the phase transformation may proceed in a distinctly different manner than in the macroscopic systems. On the other hand, they can help designing the system sizes in which the phase transformation is to be studied when using atomistic simulation.

Chapter 7

Strain-induced phase transition in Fe thin films

The mechanism and kinetics of strain-induced phase transformations are of general fundamental interest in solid-state and materials science, and the bcc $\rightarrow$ hcp and analogous phase transitions have been studied for many years, both in experiment [111, 112, 113] and in simulation [114, 115, 116]. On the other hand, interest is rising in studying phase transitions in nanoscale and surface-dominated systems [4, 5]. Due to their large surface/bulk ration, they may exhibit dramatically changed properties as compared to bulk systems. Ultrathin films provide one example of systems where the small size (thickness) influences the properties decisively. Hardwick [117] reviewed the mechanical properties of free-standing thin films. In later years, Vinci and Valssak [118] summarized thin film mechanical testing methods.

Solid-state phase transition in ultrathin films have been investigated in recent years, focusing on the martensitic transformations and shape memory behavior. Brückner *et al.* [119] studied experimentally NiCr films (thickness of 320 nm) and found phase transitions during annealing, which affect film microstructure and internal stress. Cuenya *et al.* [120] studied experimentally ultrathin Fe films and characterized the observed fcc/bcc solid state transition as a function of film thickness. FePd films were investigated with respect to their magnetic and structural in [121, 122]. The martensitic transformation and shape memory behavior were also studied in these systems [123]. Buschbeck *et al.* [124] investigated how tunable strain can be exerted on such films. Besides metal films, also films based on oxide materials were studied [125, 126]. However, iron and its alloys attract particular interest due to the magnetism associated with the structural phase transition.

In this chapter, the strain-induced phase transitions of free-standing thin Fe films will be investigated. The dynamics of the solid-solid phase transition occurring will be studied.

The influence of crystal orientation and film thickness on the phase transition will be investigated and the pathway of the transformations occurring will be analyzed.

7.1 Methodology

The strain-induced phase transition in thin Fe films is studied by using the classical molecular dynamics simulations. In order to investigate the film thickness and crystallographic orientation dependence on the phase transition, six thin films in bcc structure are constructed. Three of these (films 1, 2, 3) have approximately similar size and thickness, but vary in surface orientation and will be studied in Subsection 7.2.1; the other three (film 4, 5, 6) have identical orientation, but vary in thickness, will be studied in Subsection 7.2.2. The specifications of the six films are assembled in Tab. 7.1.

Film	x	y	z	Δx (ML)	Δy (ML)	Δz (ML)	N
1	$[\bar{2}11]$	$[0\bar{1}1]$	$[111]$	43	49	18	305660
2	$[\bar{1}10]$	$[001]$	$[110]$	49	70	22	308700
3	$[0\bar{1}\bar{1}]$	$[01\bar{1}]$	$[100]$	49	49	31	302526
4	$[111]$	$[1\bar{1}0]$	$[11\bar{2}]$	40	49	20	316447
5	$[111]$	$[1\bar{1}0]$	$[11\bar{2}]$	40	49	10	159791
6	$[111]$	$[1\bar{1}0]$	$[11\bar{2}]$	40	49	5	81469

Table 7.1: Films studied in this chapter. z gives the orientation of the surface normal and Δz the film thickness. x and y are the directions to which tensile stress is applied and Δx, Δy are the corresponding thicknesses. See Fig. 7.1 for a sketch. All lengths are given in monolayers (ML). The total atom number is denoted by N.

The setup of the simulation system is depicted in Fig. 7.1. The film construction is described by using film 1 as example. A simulation box with dimensions of $201.52 \times 198.88 \times 89.47$ Å^3 is constructed and filled with Fe atoms in bcc structure. The box size corresponds to 43 (49, 18) atom layers in x (y, z) direction. Note that the length of the bcc lattice constant in the Meyer-Entel potential, which is used for the simulations, is 2.87 Å. Films 1-3 have the same thickness of 9 nm approximately and lateral sizes of 20×20 nm^2; the number of atoms is around 300 000.

In order to investigate the influence of the film thickness on the phase transition, films 4, 5 and 6 are constructed. These films are oriented in $[11\bar{2}]$ direction. Film 4 has similar dimensions as films 1-3 discussed above. Films 5 and 6 have the same dimension in lateral (x and y) direction as film 4, but differ in thickness, corresponding to 4.7 and 2.3 nm, respectively.

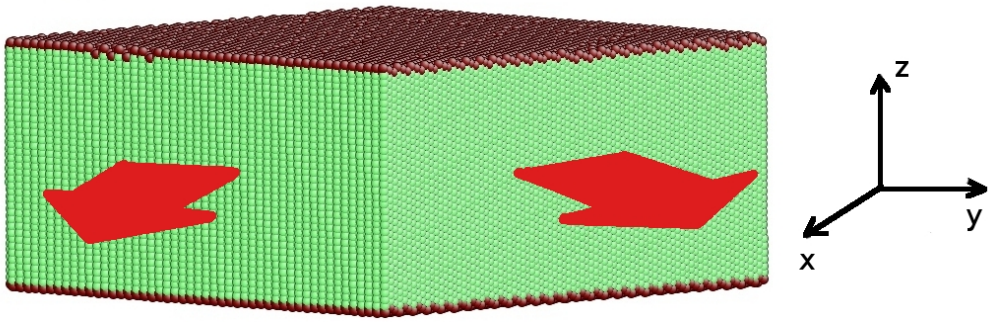

Figure 7.1: Setup of the thin film in the simulation. The surfaces in z direction are free. Biaxial strain is applied in x and y direction.

For all films, periodic boundary conditions are employed along the x and y directions; in z direction, which corresponds to the surface normal, the film surfaces are free. The systems are relaxed in an NPT ensemble at a temperature of 500 K, which is slightly below the equilibrium transition temperature in Meyer-Entel-Potential, by using a Nosé-Hoover thermostat for 50 ps. At this temperature, the bcc phase is still stable; however, the free-energy difference between the transforming phases is small, such that small influences (in this case: an applied strain) can lead to transformation. The pressure is controlled via a barostat in x and y directions; here it is set to 0, such that the pressure relaxes to < 100 MPa in lateral direction. Pressure control in the z direction (surface normal) is not employed, since here free surfaces are used; thus the pressure in z direction relaxes automatically to 0.

After relaxation, the dynamic simulations are performed in an NVT ensemble. Two (tensile) strains are applied along the x and y directions to the system with equal strength (biaxial strain). The strain is applied quasi-statically as follows. After each simulation time period of 1 ps, the system is strained homogeneously in both x and y direction by 0.05 %; then the system relaxes for the ensuing 1 ps simulation time. The strain rate thus amounts to 5×10^8 s^{-1}. The stress-strain curve, the critical strain necessary for phase transition, and the dynamics of the phase transition are studied in dependence of crystallographic orientation and the film thickness.

The local atomic structure is determined via the common neighbor analysis (CNA) [52]. Note that the energy difference between the fcc and hcp phase is quite small [69]. Therefore a transformed material is often observed, in which both hcp and fcc phases are present. This is called for short the “closed-packed” (cp) phase.

7.2 Results and discussion

7.2.1 Orientation dependence

Firstly, the stress-strain behavior of the thin films will be discussed. The total stress σ is calculated by using the following equation:

$$\sigma = \frac{1}{3}(\sigma_{xx} + \sigma_{yy} + \sigma_{zz}) \tag{7.1}$$

where σ_{xx}, σ_{yy} and σ_{zz} are the three stresses in x, y, and z directions. Fig. 7.2 displays the stress versus strain curves for the thin films with three different surface orientations. The initial linear behavior corresponds in all three cases to an elastic deformation in the bcc structure. Film 3 with a surface orientation in [100] direction shows the softest behavior, while film 1 and 2 exhibit a stiffer response.

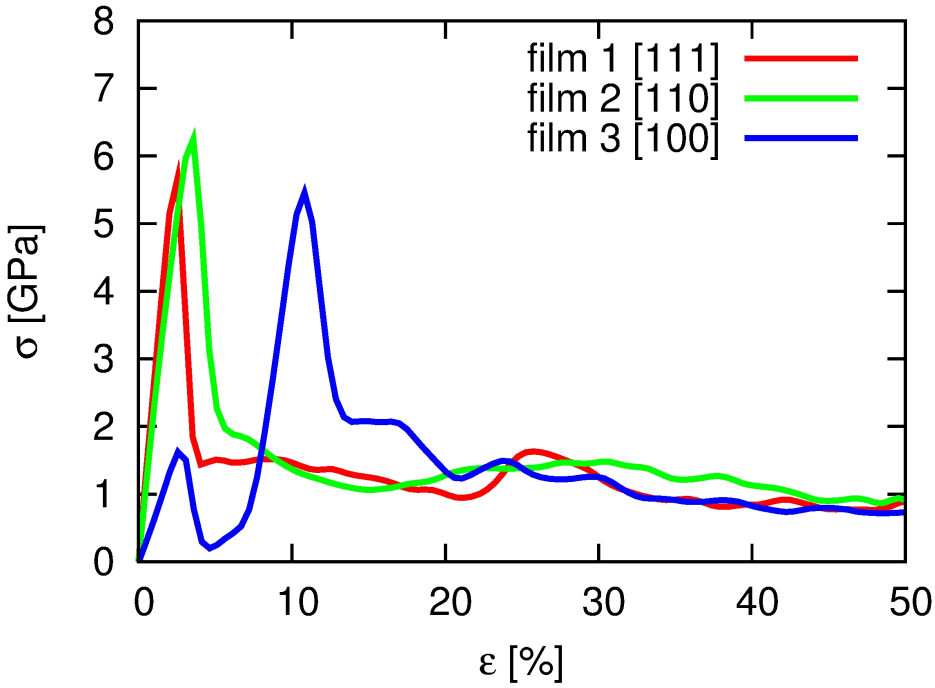

Figure 7.2: Stress vs. strain curves for films 1, 2 and 3.

After the linear-elastic increase, in each case the stress decreases strongly. This is the signal of a phase transition occurring in the film, during which stresses are relaxed. The nature of these phase transitions is discussed separately now in detail for the three films. Both fractional phase content and snapshots showing the microstructure evolution in the three films are displayed in Fig. 7.3 to 7.5.

For film 1, the bcc $\rightarrow$ cp transition takes place at a strain of 2.7 %. The fraction of the initial bcc phase decreases very rapidly, see Fig. 7.3(a), and a polycrystalline close-

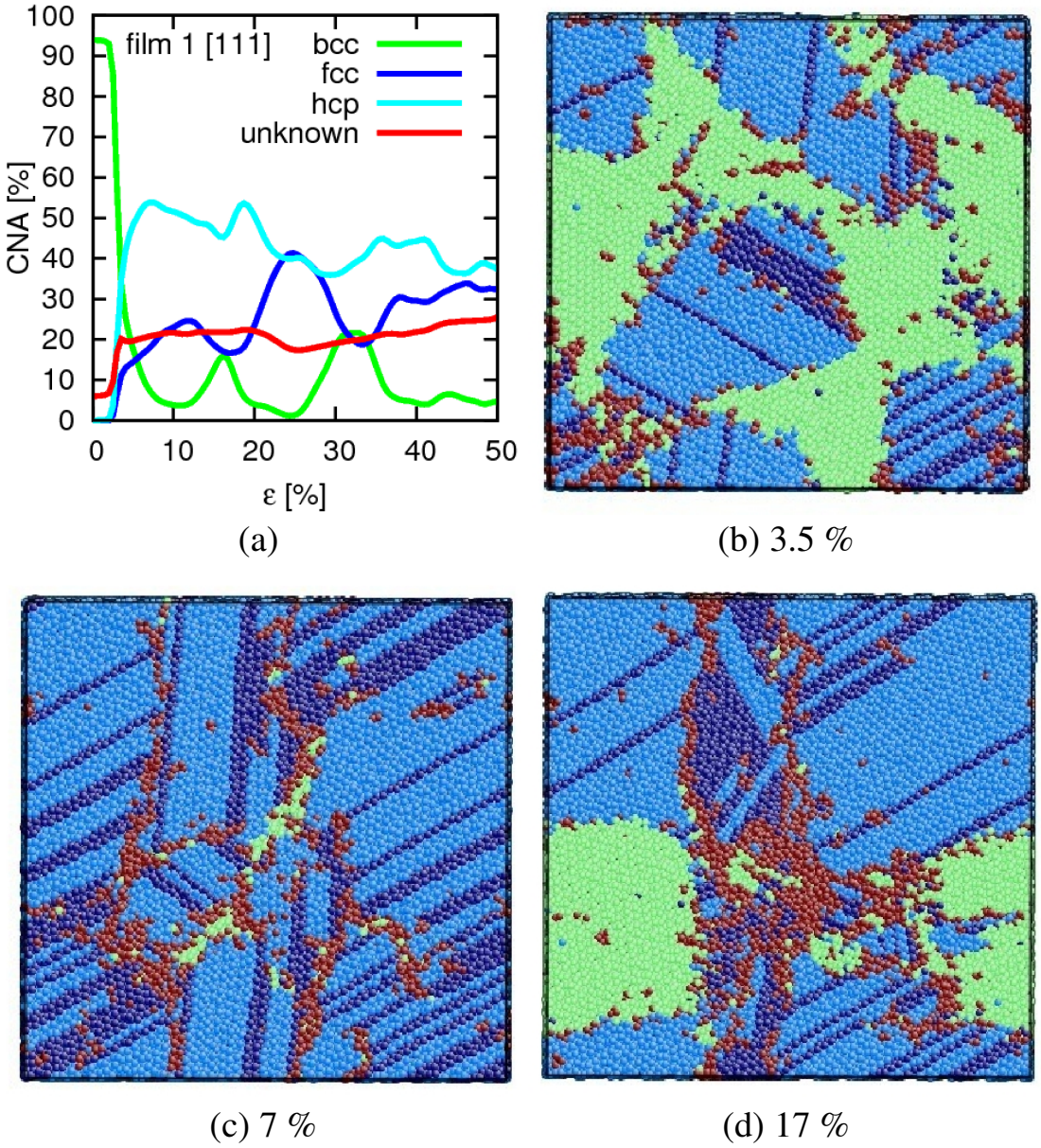

Figure 7.3: Temporal evolution of film 1 under strain. (a) Fractional phase content in the film, analyzed using common neighbor analysis (CNA). (b)-(d) Snapshots of the local atomic structure at strains of 3.5 %, 7 % and 17 % (the first bcc back transformation), in a cut along the (111) plane, parallel to the free surfaces. Colors denote the local crystal structure. Green: bcc; dark blue: fcc; light blue: hcp; red: unknown.

packed structure is formed; it consists mainly of hcp material, but also fcc grains are visible, Fig. 7.3(b). At higher strains, the phase transition decelerates. Fig. 7.3(c) shows the almost fully transformed material. The last untransformed bcc grains occupy only small volumes near grain boundaries. At a strain of 10.7 %, this first (bcc $\rightarrow$ cp) solid-solid phase transition is finished. At still higher strains, the fcc and hcp phases transform into each other. Note that the fcc and hcp phases have very similar free energies in the

Meyer-Entel potential: The free energy difference between the fcc and hcp phase is quite small, around 4 meV/atom [69]. Thus small changes in the temperature or in the pressure can cause a transition between the two phases.

At strains of 17 % and 32 %, two back transformations to the bcc phase can be observed, cf. Fig. 7.3(d). Sandoval *et al.* [17] reported a similar back transition of the partly transformed bcc phase in a nanowire system under high tensile uniaxial stress. The considerable shear deformations that build up cause a coherent shift of the lattice planes. Since the free-energy difference between the bcc and cp phase is small in the Meyer-Entel potential [56], such a coherent shift of the lattice planes may result in a change of crystal plane, i.e., a martensite phase transition.

For film 2, whose surface normal is oriented along the $[110]$ direction, the first phase transition starts at a strain of 4.0 % and is finished at a strain of 4.3 %, cf. Fig. 7.2 and Fig. 7.4(a). This transformation fits the Burgers path for the bcc to hcp transition [107] well, cf. the discussion of Fig. 7.6 below. Fig. 7.4(b)-(d) show some representative snapshots characterizing the transformations of this film. The nucleation of the cp phase takes place in this system statistically, Fig. 7.4(b); so a fine-grained polycrystalline cp structure is obtained after the first phase transition, Fig. 7.4(c). The reason for this statistical nucleation is the inhomogeneous distribution of the stress in this system. The increase of the unidentified atoms at a strain of 4 % occurs mostly at the grain boundary. The transformed cp phase contains a high fcc fraction of about 33 %. The fcc phase grows at the cost of the hcp phase. At a strain of 12 %, fcc and hcp have the same fraction in the cp phase; at larger strains, the fcc phase even surpasses the hcp phase and dominates to about 67 % in the cp phase. The reason for the transformation between the fcc and hcp phase has been discussed in the case of film 1 above.

The $[100]$ orientated thin film (film 3) loses its elasticity in a strain range from 2.7 % to 7 %, see Fig. 7.2. According to common neighbor analysis (CNA), Fig. 7.5(a), the initial bcc phase transforms continuously to a predominantly hcp phase; Fig. 7.5(c) shows that the fcc phase is contained in the hcp phase mainly as stacking fault planes. Thus, in contrast to the other orientations, an almost pure hcp thin film with relatively large grains is obtained at a strain of 7 %; the fcc fraction is only about 8 %. Compared to film 2, the phase transformation runs slower by a factor of ten. Since this is now an almost pure hcp film, it exhibits a second elastic regime up to a strain of 10.9 %. Note that the slope of the second elastic regime is steeper than that of the initial bcc phase; this is due to the fact that a different phase of the material exists in a nanocrystalline microstructure. Beyond strain of 10.9 %, the elasticity is lost again.

In Fig. 7.5, further aspects of evolution of the $[100]$ oriented thin film (film 3) can be observed. During the first solid-solid phase transition, see Fig. 7.5(a) and (b), the cp phase develops at the cost of the initial bcc phase until the whole system is transformed. Few

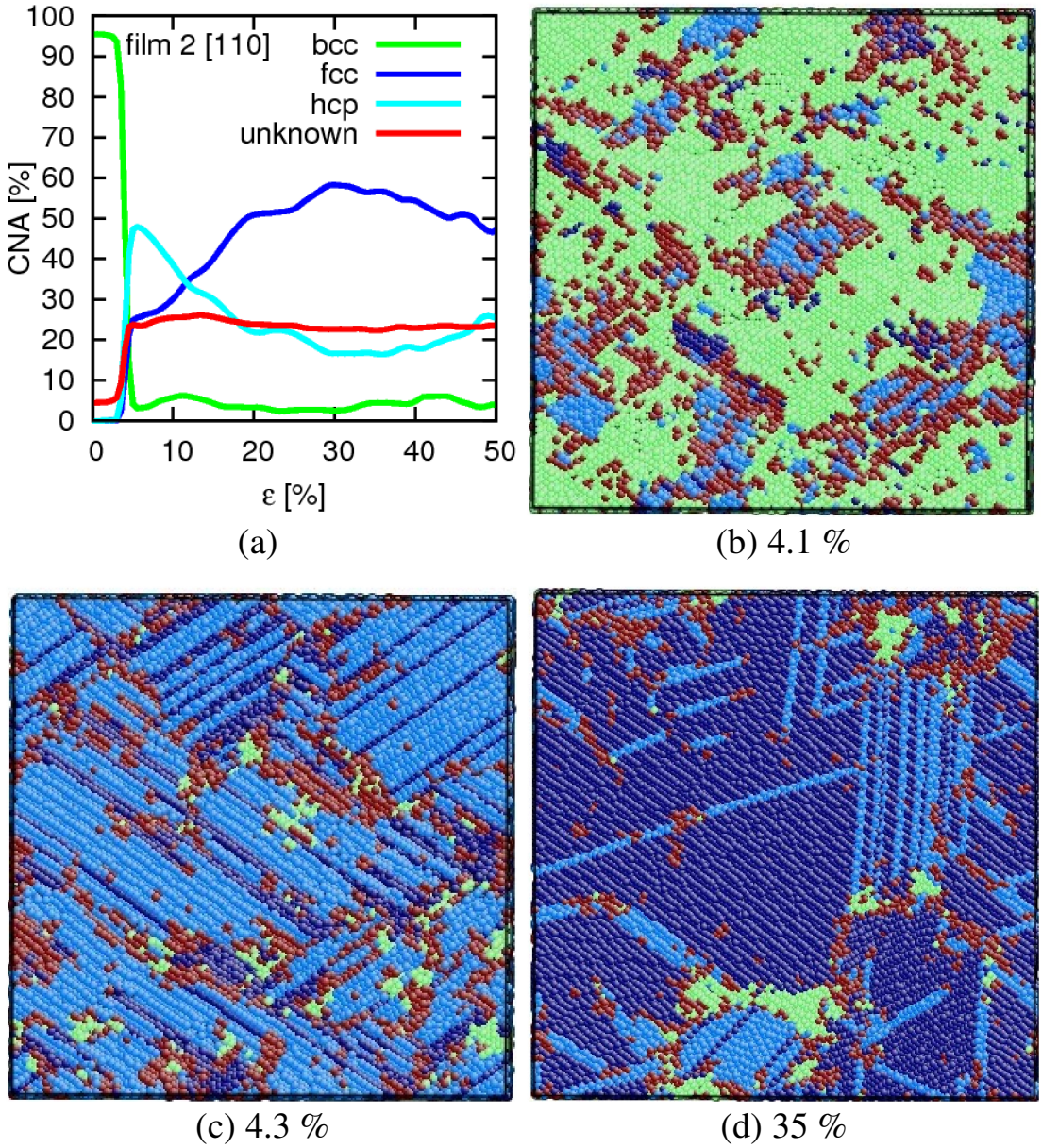

Figure 7.4: Temporal evolution of film 2 under strain. (a) Fractional phase content in the film, analyzed using common neighbor analysis (CNA). (b)–(d) Snapshots of the local atomic structure at strains of 4.1 %, 4.3 % and 35 %, in a cut along the (110) plane, parallel to the free surfaces. Colors denote the local crystal structure as in Fig. 7.3.

large hcp grains, which are oriented perpendicular to each other, are obtained. The fcc phase can be considered as stacking fault planes in the hcp phase, extending only one or two atom layers in width. see Fig. 7.5(c). The stacking faults planes are mostly oriented parallel to the x (i.e., $[0\bar{1}\bar{1}]$) direction and to the y (i.e., $[01\bar{1}]$) direction. The occurrence of these stacking fault planes can be explained in the following way. The difference between the fcc and hcp phases is just the stacking sequence. If one lattice plane of the fcc (hcp) lattice is shifted by the shear stress parallel to its neighboring planes, a stacking fault plane

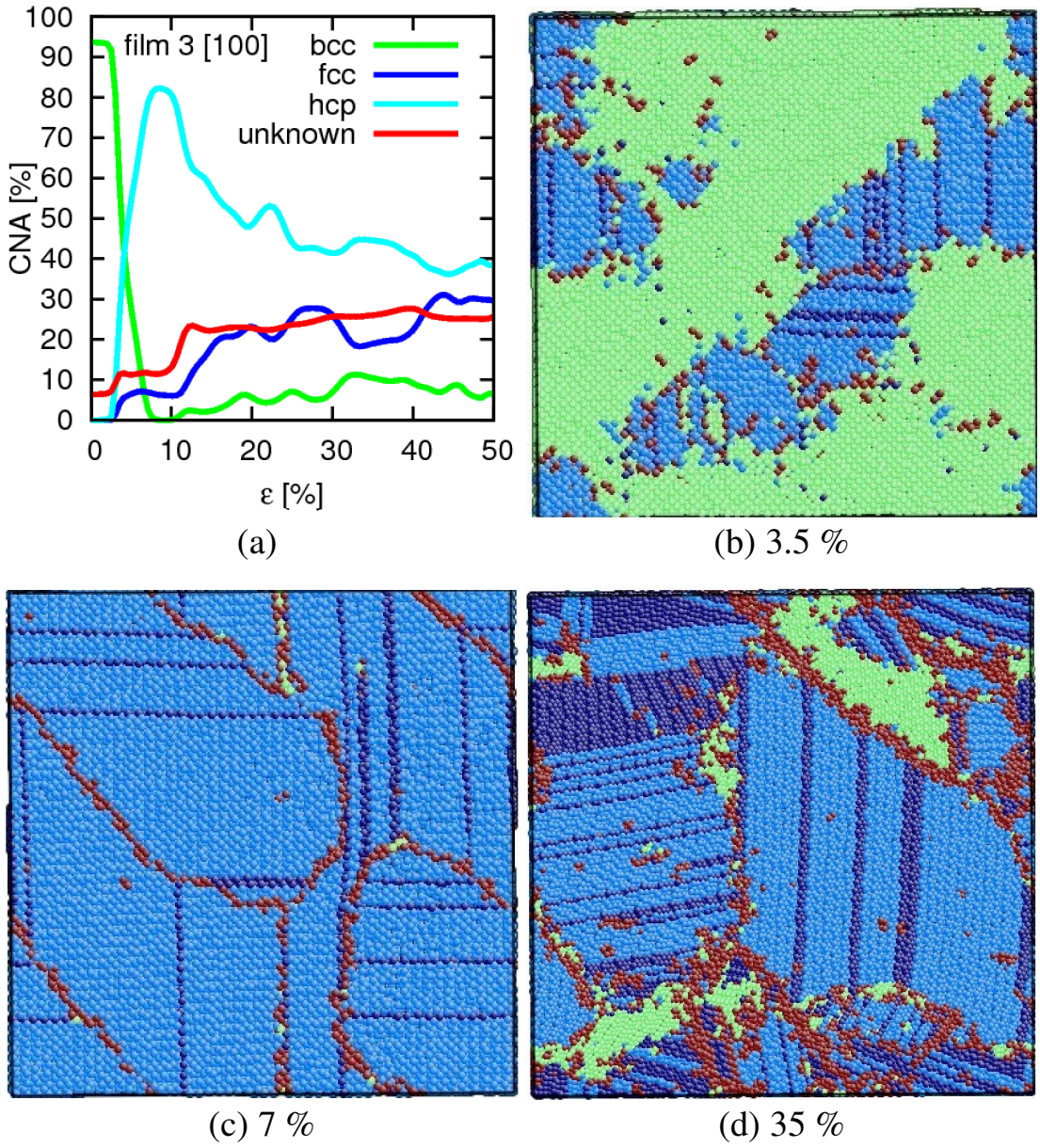

Figure 7.5: Temporal evolution of film 3 under strain. (a) Fractional phase content in the film, analyzed using common neighbor analysis (CNA). (b)-(d) Snapshots of the local atomic structure at strains of 3.5 %, 7 % and 35 %, in a cut along the (100) plane, parallel to the free surfaces. Colors denote the local crystal structure as in Fig. 7.3.

will be produced. The applied strain acts exactly as the necessary shear to shift the hcp atom layers to build a stacking fault.

After the second elastic regime, which corresponds to the elastic response of the hcp phase, small parts of the film transform back to the bcc structure; however, the fraction of back transformed bcc material is small, only up to 10 %. Simultaneously, with increasing starin, a reorientation of the hcp grains can be observed, see Fig. 7.5(d). Note that, in

nanowires, the phenomenon of reorientation has been reported repeatedly for fcc metals [127, 128].

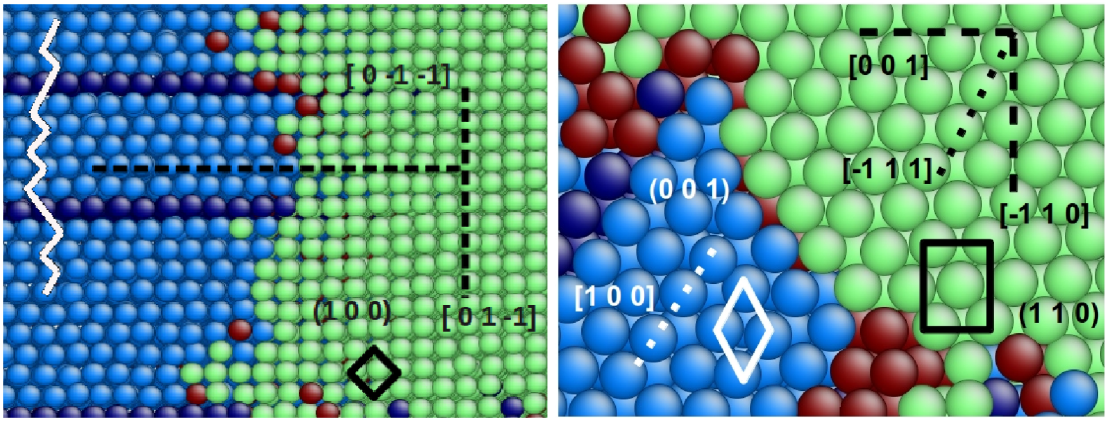

(a) (b)

Figure 7.6: Close-up into the transforming areas. Colors denote the local crystal structure as in Fig. 7.3. These close-up snapshots confirm that the bcc $\rightarrow$ hcp transformation observed obeys the Burgers orientation relations [107]. The dashed lines indicate the crystal orientations in x and y directions. The black solid squares denote bcc unit cells. The white rhombus denotes a unit cell in the hcp phase. (a) Film 3 with $[100]$ surface normal. Close-up into Fig. 7.5(b). By following the solid white line a stacking fault in the hcp phase can be identified. (b) Film 2 with $[110]$ surface normal. Close-up into Fig. 7.4(b). The black dotted line indicates the $[\bar{1}11]_{\mathrm{bcc}}$ direction, parallel to $[100]_{\mathrm{hcp}}$ direction, which is indicated by the white dotted line.

The pathway of the first bcc $\rightarrow$ hcp phase transition occurring in these 3 films is analyzed by close-up into the transforming region of the thin films, Fig. 7.6. All the transformations obey the Burgers path [107] for the bcc $\rightarrow$ hcp transition with orientation relationship

$$(110)_{\mathrm{bcc}} \parallel (001)_{\mathrm{hcp}} \qquad \text{and} \qquad [\bar{1}11]_{\mathrm{bcc}} \parallel [100]_{\mathrm{hcp}}.$$

This finding is demonstrated by two examples. Fig. 7.6(a) shows a $(100)_{\mathrm{bcc}}$ plane of film 3 with $[100]$ surface orientation. The horizontal direction is $[0\bar{1}\bar{1}]_{\mathrm{bcc}}$ and the vertical direction is the $[01\bar{1}]_{\mathrm{bcc}}$. The solid line shows the stacking fault (...ABABCABAB...) in the hcp phase, which is identified as fcc phase by CNA. Fig. 7.6(b) shows a $(110)_{\mathrm{bcc}}$ plane of film 2 with $[110]$ surface orientation. The horizontal and vertical directions correspond to the $[\bar{1}10]$ and $[001]$ directions of the bcc phase. Also in this case, stacking faults can be observed in the hcp phase, Fig. 7.4(b). The hexagonal structure is formed through two perpendicular shears in $[\bar{1}10]_{\mathrm{bcc}}$ and $[001]_{\mathrm{bcc}}$ directions.

7.2.2 Thickness dependence

In this subsection, the influence of film thickness on the transformation behavior will be discussed. A different surface normal orientation, the $[11\bar{2}]$ direction, is chosen here. This has the interesting feature that strain can be applied on the closet packed direction ($[111]$), the x direction. As Table 7.1 shows, film 4 has approximately the same size as the cases discussed in Subsection 7.2.1 above. This film will be introduced firstly. Then films 5 and 6, whose thickness has been shortened with respect to film 4, will be presented.

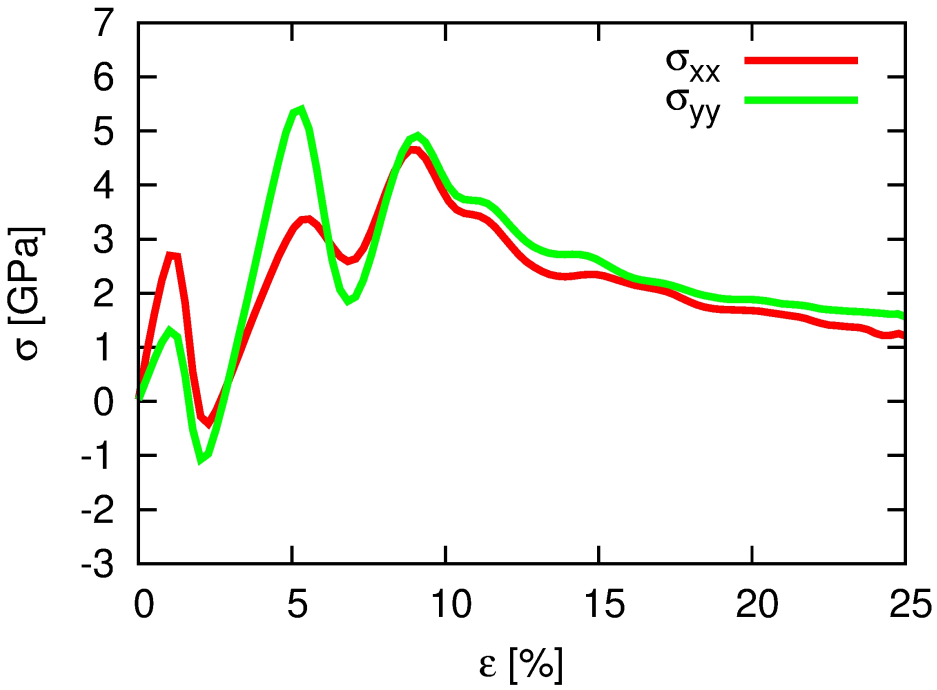

Figure 7.7: Stress vs strain curves for film 4. The diagonal inplane stresses σ_{xx} and σ_{yy} are plotted.

Firstly, the phase transition in a thin Fe film with a thickness of 9.4 nm (film 4) will be discussed. Fig. 7.7 shows the stress-strain behavior along the x and y directions up to a strain of 25 %. The $[111]$ direction is stiffer than then $[110]$ direction; this is similar to the behavior in the bulk material. After the fist linear-elastic regime, the stress-strain curves feature two more elastic regimes, which begin at a strain of 2.5 % and 7 %, respectively.

Figure 7.8(a) shows the evolution of the fractional phase content in this film with increasing strain. These data make it possible to identify the origin of the 2 further elastic regimes. The first regime corresponds to the transformed hcp phase; the second regime belongs to a cp phase which includes some back transformed bcc material. Fig. 7.8(b)-(d) show several representative snapshots. The whole transformation process can be divided into the following steps with increasing strain.

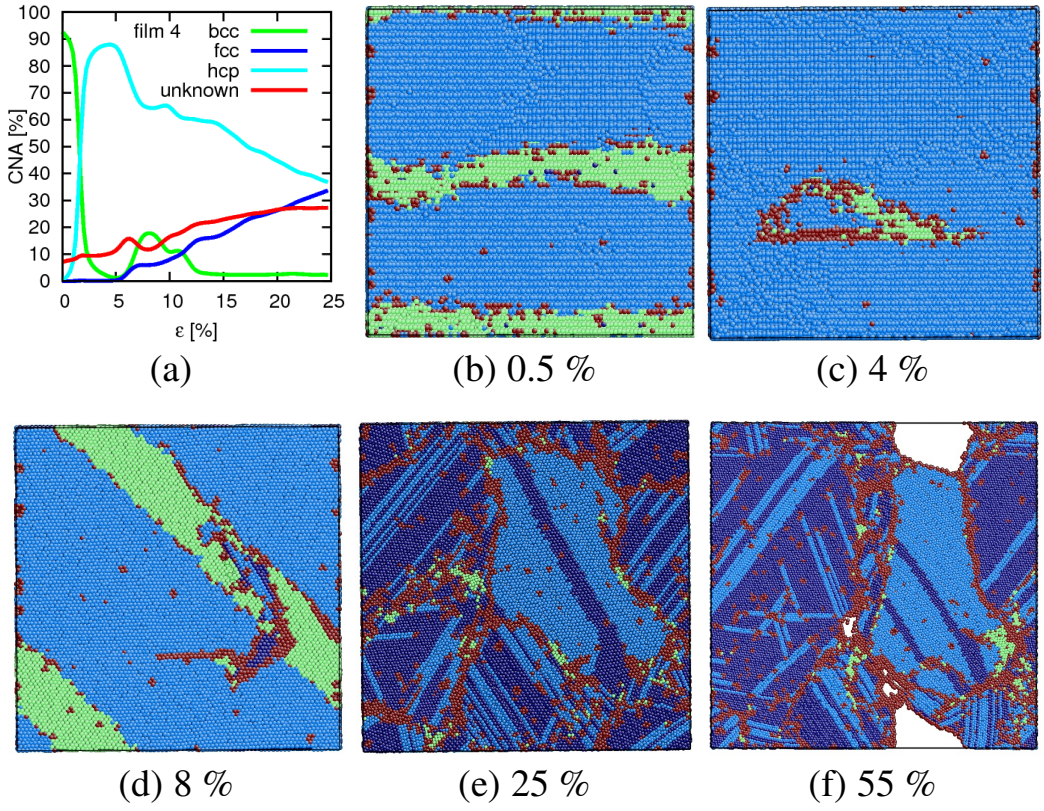

Figure 7.8: Temporal evolution of film 4 under strain. (a) Fractional phase content in the film, analyzed using common neighbor analysis (CNA). (b)-(f) Snapshots of the local atomic structure at strains of 0.5 %, 4 %, 8 %, 25 % and 55 %, in a cut along the $[11\bar{2}]$ plane, parallel to the free surfaces. Colors denote the local crystal structure as in Fig. 7.3.

(i) The first solid-solid phase transition takes place almost immediately after strain was applied, at a strain of about 1 %; it is terminated at a strain of about 3.5 %. The whole system transforms from its original bcc structure into pure hcp structure, cf. Fig. 7.8(b) and (c). Note that only 2 grains result here, of which one dominates the film volume. This hcp phase is responsible for the second linear elastic regime in Fig. 7.7.

(ii) For strains between 7 % and 10 %, a partial back transformation from the hcp phase to the bcc phase can be observed. Note that this back transformed phase has a different crystal orientation than the initial bcc phase, see Fig. 7.8(d). The fraction of the reconverted bcc phase amounts to 20 %, cf. Fig. 7.8(a). The back transformed bcc phase disappears again with further increased strain.

(iii) Some hcp material transforms into fcc structure. Stripe-shaped fcc phase in the hcp matrix is obtained. The film transforms from its original monocrystalline structure into a polycrystalline structure, Fig. 7.8(e).

(iv) The film starts breaking along a grain boundary, Fig. 7.8(f).

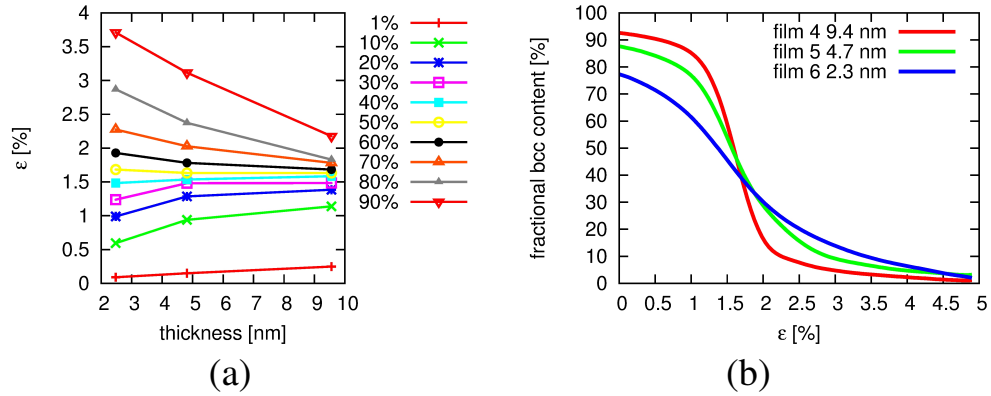

Figure 7.9: (a) Dependence of the transition strain, for which the fraction indicated in the legend has been transformed from bcc to cp, on film thickness. Symbols denote data taken for films 4, 5, and 6. Lines are to guide the eye. (b) Fractional content of the bcc phase as a function of strain for various film thicknesses.

The thickness of film 4 is reduced to 4.7 nm (film 5) and 2.3 nm (film 6). The phase transitions in the thinner films occur in an analogous fashion to that in the thicker film 4; hence snapshots for thinner films are not present here. Note that, the intergranular crack, which destroys the films at high strains, occurs earlier in thinner films than in thick films; this appears plausible.

Instead the dynamics of the first solid-solid phase transition is analyzed in detail. A transition degree over 90 % can be achieved for all three thickness. Fig. 7.9(a) shows the strains, at which a particular degree (from 1 % to 90 %) of the first bcc $\rightarrow$ hcp transformation is achieved versus the film thickness. The phase transformations starts earlier, i.e., at lower strain, in thinner films than in thicker films. This can be explained by noting that thinner films have a higher surface fraction than thicker films; the surface allows more space for the nucleation of the new phase compared to the bulk, and hence the new phase can be formed more rapidly in thinner films. A transformation degree of 40 % is achieved at a strain of about 1.6 % for all three cases. For larger strains the phase transition in thicker films develops faster than in thinner films.

The observation that the phase transition occurs more readily in thinner films parallels analogous findings for nanowires. Thus, in a study on phase transformation in nanowires, Sandoval and Urbassek [18] reported that the transition temperature increases inversely proportional to the diameter of the nanowires. Also in nanowire systems, a higher surface/bulk ratio helps the transformation process.

Figure 7.9(b) shows the change of the bcc fraction with increasing strain for different film thickness. The three curves cross at a transition degree of about 40 % with a strain

of 1.6 %. The slope of the curve for thicker films is higher than that for the thinner ones; this means that thick films exhibit a higher transformation velocity. These findings complement those of Fig. 7.9(a).

7.3 Conclusions

In this chapter, the strain-induced phase transition of thin Fe films was studied in its dependence on crystal orientation and film thickness. The mechanical behavior of the films, i.e., the stress strain curve, indicated that a complex series of processes occurs in the films. The analysis of the variation of the phase content in the films with increasing strain and the inspection of snapshots during the film evolution make the identification of the sequence of phase transformation possible, accompanied by nucleation of new grains and crystal reorientation, which are responsible for the film evolution.

The strain-induced transformation of the thin films was divided into four steps. It occurs typically in the sequence of (i) a bcc $\rightarrow$ hcp transition; (ii) the partial back transformation to the bcc phase; (iii) grain modification of the cp phase; (iv) finally, intergranular fracture occurs.

The reason for the complex processes occurring under strain lies in the build-up of high internal stresses in the film. Due to the small film thickness, these stresses cannot be relaxed by plastic deformation, i.e., the formation of dislocations. Rather phase transition occurs and relieves the stress. The crystal transforms mainly to the hcp structure, containing a high amount of fcc material (cp phase). This transformation obeys the Burgers mechanism in all cases, i.e., film orientations, studied.

Depending on the crystal orientation, the transformed cp phase reacts differently to a further increase of the strain. The two typical pathways observed are partial back transformation to the bcc structure, but with reoriented grains, and grain refinement.

Film thickness does not play a major role in the sequence of film transformations and grain reorientation processes occurring. This is due to the small film thickness of interest to this chapter, in which the formation of dislocations as a remedy to relieve the high stresses building up is improbable. However, an influence of film thickness on the transformation velocity was found. Thinner films allow for a faster nucleation of the new phase; the higher surface/volume ration in thinner films facilitates phase nucleation.

Chapter 8

Martensitic and austenitic phase transition in Fe-C bulk system

Fe-based materials, and in particular Fe-C alloys, are of special relevance. Solid-solid phase transition in bulk steel have been investigated for many years [1, 2, 3, 13], because many important applications are found in this area, e.g., for controlling the microstructure and the further change of macroscopic properties. However, atomistic simulation methods have up to now rarely been used to study phase transition in the Fe-C system. The majority of atomistic studies focused on the transition in pure iron [3, 10, 11, 12, 13, 16, 17, 18, 19] or in iron-metal alloys [20, 21, 22].

All alloying elements have a strong influence on the α-γ transition temperature of Fe; elements have therefore been classified into those that stabilize the α phase (γ-loop forming elements) and those that destabilize it (γ-openers). For substitutional alloys, the number of electrons introduced by the alloying element plays the central role, as it influences the magnetism in the alloy and hence the relative stability of α and γ phase [2]. Phase stability of interstitial alloys, in contrast, depends on the interstitial volume present in the different phases. Here, for simple geometric reasons, the gamma phase provides more space: The radius of the octahedral site in the Fe fcc lattice, r = 0.571 Å is larger than either the tetrahedral (r = 0.360 Å) or octahedral site (r = 0.191 Å) in the bcc lattice. This feature explains simply both the higher solubility in the fcc phase and the destabilization of the bcc lattice with increasing alloy concentration; it holds similarly for C, N and B interstitials.

This simple geometrical concept is corroborated by an analysis of the influence of C interstitials on the bonding and the elastic constants in Fe-C alloys. A recent combined experimental and theoretical study has observed that C atoms weaken the Fe-Fe bonds in the α phase, since Fe atoms neighboring an interstitial are shifted apart [30]. Similarly the elastic constants are weakened. In particular the elastic anisotropy, which is characterized

by the ration of the maximum and minimum shear modulus, increases with C content in the alpha phase; this feature is thus directly connected with the tetragonal distortion building up. As Zener [129] showed the increased anisotropy destabilizes the bcc lattice structure.

In this chapter, the $\alpha \leftrightarrow \gamma$ phase transition in Fe-C bulk systems will be studied. Both the austenitic and martensitic phase transition will be analyzed. The dependence of the transition temperatures on the C content and the transition pathway will be investigated.

8.1 Methodology

The phase transitions in the Fe-C system are studied by using the method of classical molecular dynamics simulation. The simulation volume is cubic and contains a bcc crystallite; all faces oriented in $< 100 >$ directions. The dimensions of the system amount to $43.05 \times 43.05 \times 43.05$ Å^3; this corresponds to 15 bcc atom layers in each cartesian direction. The total number of Fe atoms amounts to 6750. C atoms are inserted randomly in the octahedral interstitial sites. Note that, due to this random insertion, the simulation volume shows no tetragonal distortion but remains cubic. Five different atomic C concentrations are investigated: 0 at%, 0.2 at%, 0.5 at%, 0.8 at% and 1 at%. Periodic boundary conditions are employed in all three directions.

Fe atoms interact via the Meyer-Entel interaction potential [31] with each other. The C-Fe interaction is taken from the work of Johnson *et al.* [73]. Finally, C atoms interact via the Tersoff potential [130].

The systems are relaxed for 50 ps in an NPT ensemble at 50 K with pressure control (0 Pa) in all three directions. After equilibration, a heating/cooling cycle is performed: The temperature is increased from 50 K up to 1600 K with a heating rate of 1 K/ps, and then cooled down from 1600 K to 50 K with the same rate. The total simulation time thus amounts to 3.1 ns. During this cycle the simulation is controlled via an NPT ensemble: The temperature is controlled through a Nosé-Hoover thermostat and the pressure is fixed to 0 through a barostat with pressure control in all three directions. By the solid-solid phase transformations, the initially cubic volume can deform to a parallelepiped. The evolution of the system volume is monitored. The austenite and martensite temperature are determined from the volume-temperature plots.

For each C-concentration, five different simulations are run, which differ from each other by the initial C atom position. For each simulation, the austenite and martensite temperature are determined. The average over these individual temperatures is taken as the final result.

To study the dependence on the heating/cooling rate, 5 cooling rates are investigated: 1, 2, 3, 4 and 5 K/ps for the system with 0.5 at% C. In this case the initial positions of the C atoms are exactly the same for these runs.

All calculations are performed with the open-source LAMMPS code [85]. The local atomic structure is determined by using common-neighbor analysis (CNA) [52].

8.2 Results and discussion

8.2.1 Austenitic and martensitic phase transition

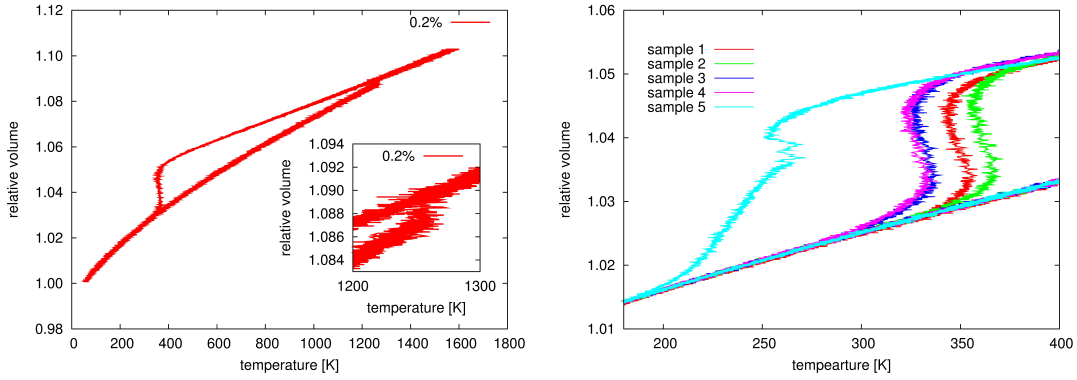

(a) (b)

Figure 8.1: Dependence of system volume on temperature during a heating/cooling cycle. C concentration 0.2 at%. Data normalized to the volume at 50 K immediately after relaxation. (a) Data for the entire heating/cooling cycle. Inset shows details of the austenitic transition. (b) Individual data for 5 different systems with identical C concentration (0.2 at%) but varying sites of the C atoms in the bcc Fe lattice.

Firstly, the temperature-induced phase transition in the Fe-C systems will be discussed. Fig. 8.1(a) displays the volume-temperature plot for the 0.2 at% system as an example. Upon heating, the system expands until at around 1250 K, the volume jumps suddenly; this indicates the austenitic transformation to the fcc phase. Upon cooling, the system contracts until around 380 K and the volume jumps back at this temperature, indicating the transformation to the bcc phase. The hysteresis observed here thus can be taken as an indicator of a first order structural phase transition. Similar hystereses have been observed previously in metallic systems during the austenitic/martensitic phase transition [131, 132, 133].

Note that the volume changes occur abruptly, thus signaling that the transformations proceed in one step throughout the simulation volume. This is due to the fact that (i) the simulation is started from a single crystal; (ii) due to the high thermal rates strong

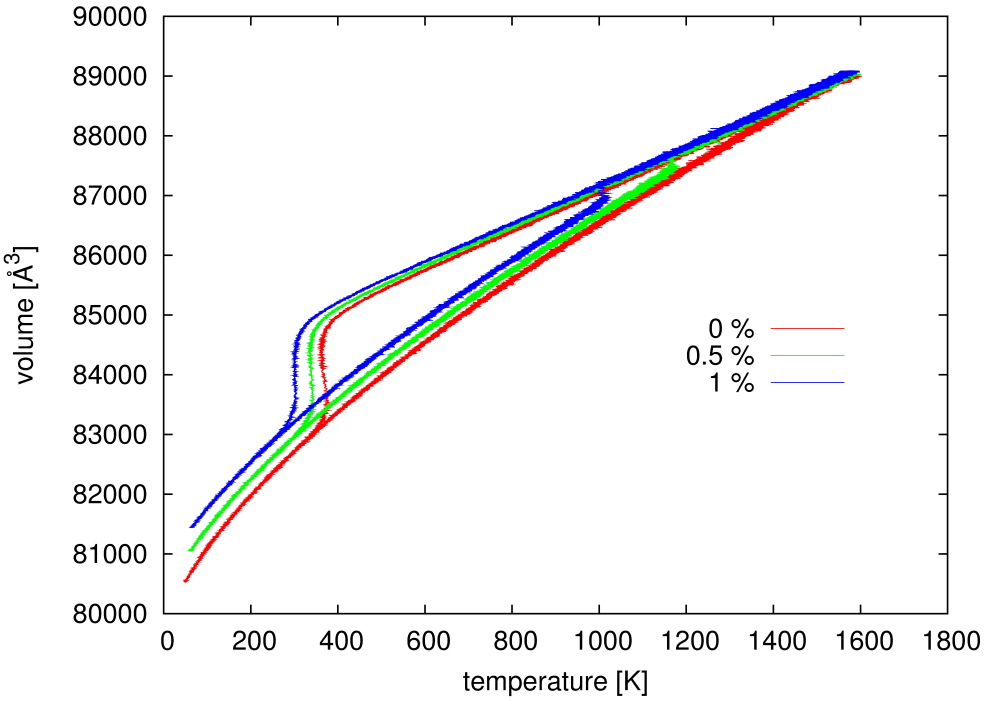

Figure 8.2: Dependence of system volume on temperature during a heating/cooling cycle. Data for several C concentrations are shown.

superheating and -cooling are created and thus the driving force for the transition becomes strong; (iii) the system is small. In experiment, as a rule the transformation proceeds in several steps [134]; thus it is necessary to distinguish between a martensite start and martensite finish temperature. This is not necessary in the simulations here.

The volume change in the austenitic transformation is considerably smaller than that in the martensitic transformation. This is due to the local microstructure forming in the austenitic phase and will be discussed below, see Fig. 8.6 in Subsection 8.2.2.

In Fig. 8.1(b), data are compared on the martensitic transition for the individual simulations performed for the system with 0.2 at% C concentration. 5 individual systems have been simulated which only varied in the initial random position of the C atoms. Considerable changes between the individual systems can be seen. The maximum variation of the martensite temperature amounts up to 100 K. Note that the influence on the austenite temperature is much smaller. The results for systems with higher C concentration are similar. The strong influence of the random C positions is attributed to the local elastic stress generated by them. High local stresses will influence the phase transition.

C atoms do not diffuse during the simulations; they remain at the position which they occupied initially. This means that C atoms will not equilibrate or homogenize their positions in the course of the simulation.

Figure 8.2 shows the volume-temperature hystereses for varying C concentration. The absolute volumes of the systems are displayed here to show the volume increase of the

initially relaxed samples with increasing C content. The main result here is that the austenite and martensite temperatures decrease systematically with increasing C content.

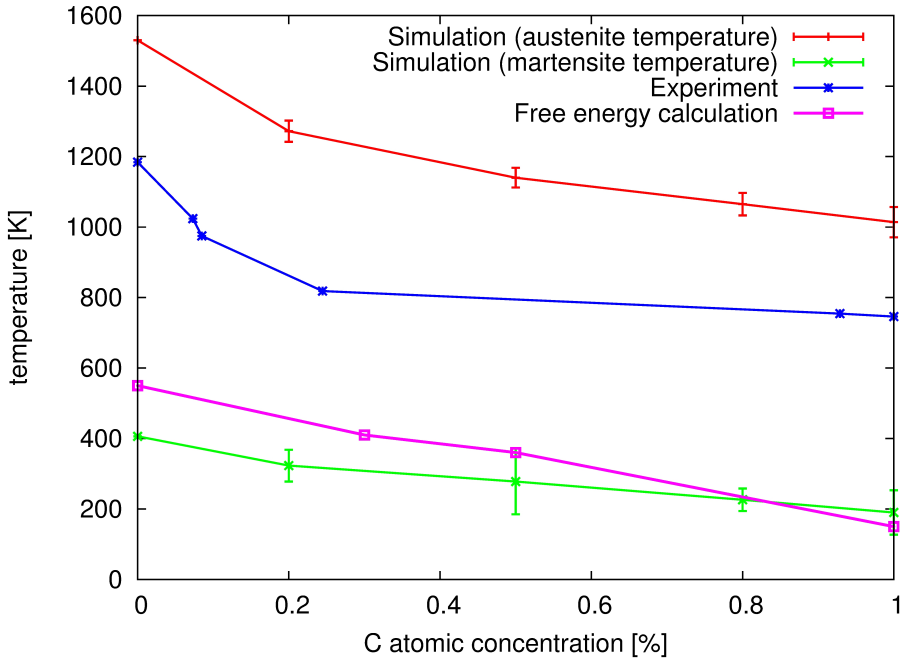

Figure 8.3: The austenite and martensite temperature in dependence of the C concentration compared with experimental values [134] and the results from free energy calculations [135]. Error bars denote the average error of the mean values for the simulation data.

These data are quantified in Fig. 8.3, which shows the austenite and martensite temperature in dependence of the C concentration. The simulation results are compared with the experimental values [134]; these have been obtained for the martensite start temperature. In addition, the recently obtained transition temperatures from free-energy calculations are included [135]. The simulation data for the martensite temperature are considerably smaller than the experimental data. This is a well-known feature of the Meyer-Entel potential used for the simulations, which features the equilibrium bcc-fcc phase transition temperature at 550 $\pm$ 50 K [56]; in reality it is 1185 K. However, the data are in good agreement with the recent free-energy calculations.

Figure 8.4 displays snapshots of the simulation system for the 0.2 at% C concentration during the heating/cooling cycle. The initial and final surface is a bcc $\{100\}$ plane. Fig. 8.4(b) shows a snapshot just during this austenitic transition. Here the local crystal structure of many Fe atoms cannot be identified correctly by using the CNA. This is due to several reasons: (i) During the phase transition, the atoms leave their equilibrium positions. They may be located on the intermediate positions between the fcc and bcc sites. (ii) The high temperature leads to strong thermal fluctuations of the atoms, which influence the operation of the CNA detector negatively. (iii) As mentioned before, the

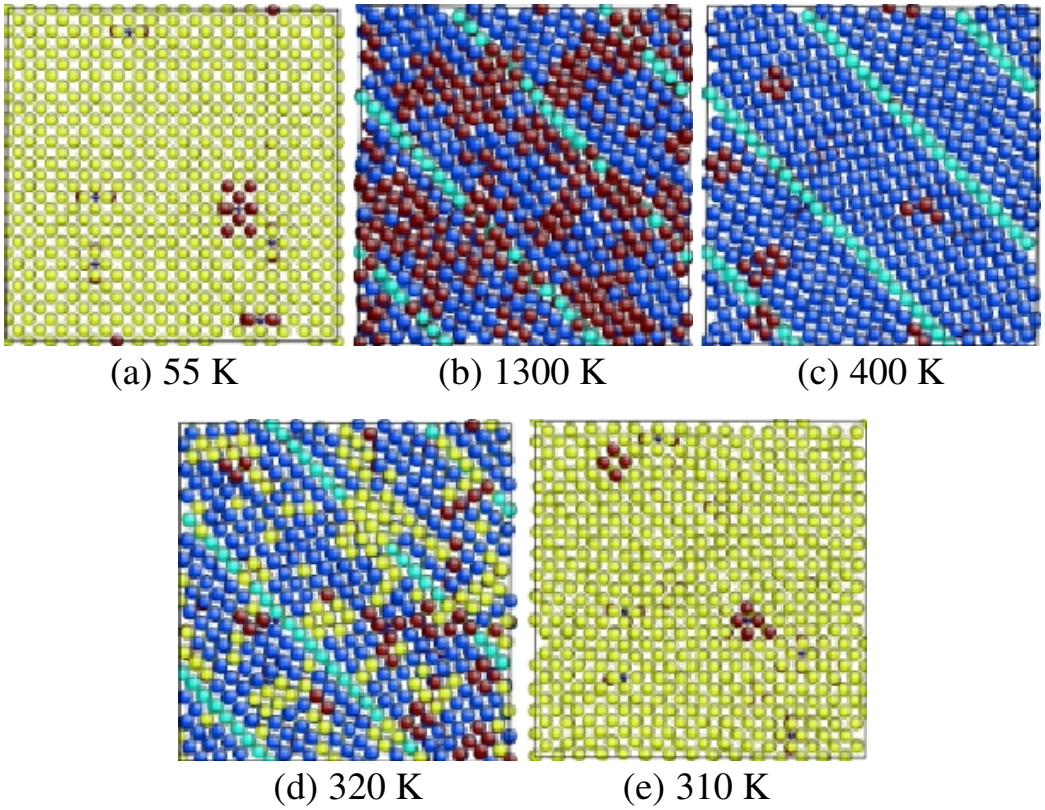

Figure 8.4: Snapshots of the system with 0.2 at% C concentration during the heating [(a) and (b)] and cooling [(c)-(e)] cycle. Colors denote the local crystal structure as obtained by CNA. Yellow: bcc; dark blue: fcc; light blue: hcp; red: unknown; small blue spheres: C atoms.

C atoms disturb the local symmetry of the Fe lattice. Fig. 8.4(c) shows the completely transformed austenite phase at temperature of 400 K (during the cooling phase). The transformed fcc phase shows a characteristic twin structure, which will be discussed in detail in Subsection 8.2.2. At a temperature of 320 K, Fig. 8.4(d), the martensitic phase transition takes place, and is terminated at 310 K, Fig. 8.4(e).

8.2.2 Mechanisms of the transition

In this subsection, the pathway followed by the phase transition will be discussed. The simulations show that the pathway of the transition is similar in all systems. The system with 0.2 at% C concentration is taken as an example.

Figure 8.5 displays the evolution of the stress during the heating/cooling cycle. Due to the barostat, the pressure is well controlled and stays at zero during the cycle. Only at the austenitic and martensitic phase transitions, considerable stresses are created in the system. While the stresses in the austenitic transition are only around 0.1 GPa, stresses in the martensitic transition amount to > 1 GPa.

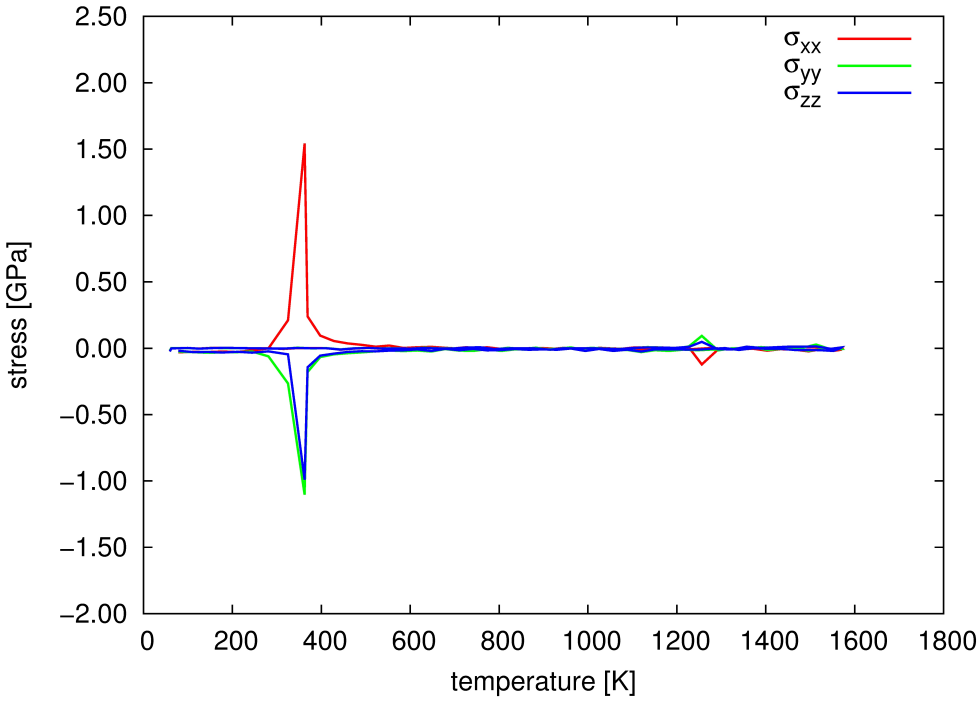

Figure 8.5: Diagonal components of the stress tensor in the three cartesian directions during the heating/cooling cycle for the system with 0.2 at% C concentration. Data have been smoothened to get rid of temperature-induced fluctuations.

The difference can be understood by monitoring the microstructure developing in the austenite phase, Fig. 8.6. The formation of a regular twin structure can be observed here. The twin planes running diagonally through this figure are $\{111\}$ planes, as it is common in the fcc systems. The lattice shear accompanying twinning relieves the stress during the transformation and is thus responsible for the relatively small stresses showing up during the transition.

Upon cooling, at the martensite temperature, the twinned austenite structure transforms back to bcc and the twin structure is resolved. Without the stress-relieving effect of the twins, the martensitic transition causes about 12 times higher stress than the austenitic transition (Fig. 8.5) and the volume change is much bigger than the austenitic phase transition (Fig. 8.1 and 8.2).

8.2.3 Dependence on the heating/cooling rate

It is well known [136] that the difference of the austenite and martensite temperature (the width of the hysteresis) depends on the heating/cooling rate dT/dt: The hysteresis becomes wider for larger rate. Simulations of heating/cooling rates from 1-4 K/ps are performed for an Fe-C system with 0.5 at% C concentration. The simulation results, Fig. 8.7(a), show that indeed the width of the hysteresis increases with dT/dt; the austen-

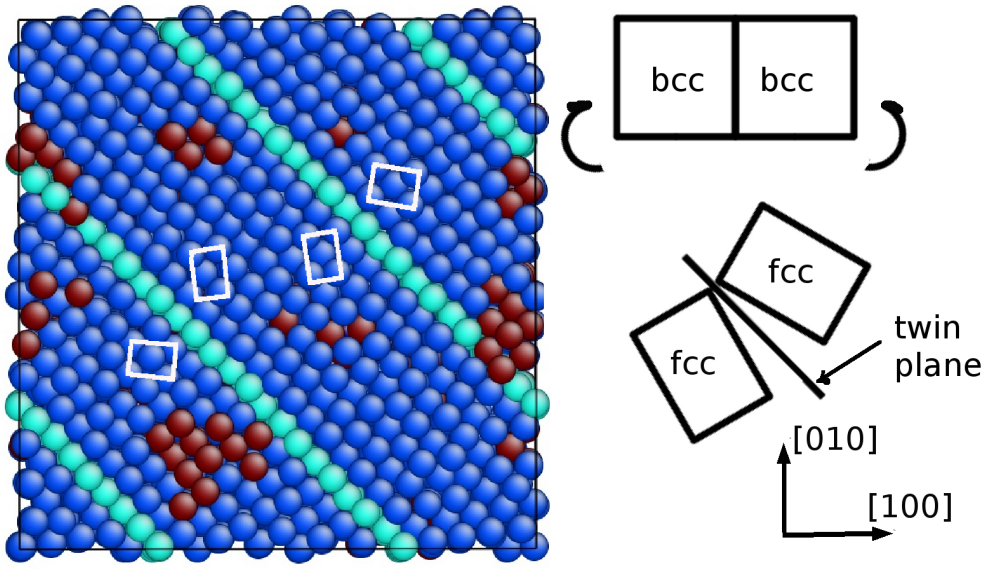

Figure 8.6: Twin structure developing during the austenitic phase transition for the system with 0.2 at% C concentration. The snapshot shows the original $(001)_{\mathrm{bcc}}$ plane which has transformed to a $(\bar{2}11)_{\mathrm{fcc}}$ plane. The axis orientation of the initial bcc phase is indicated at the lower right-hand side. The white rectangles show the symmetric fcc lattice at both sides of the twin planes. The formation of the twin structure is indicated schematically.

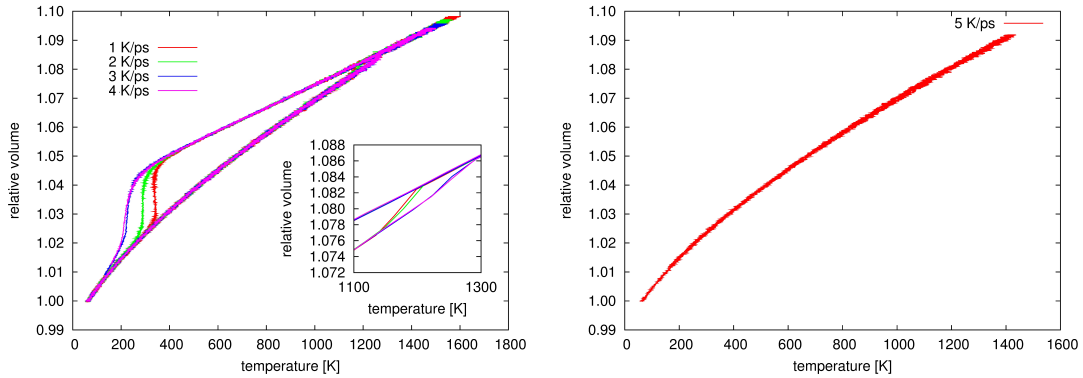

(a) (b)

Figure 8.7: Dependence of relative system volume on temperature during a heating/cooling cycle. (a) Data are shown for for heating/cooling rates from 1-4 K/ps for the system with 0.5 at% C concentration. Inset shows details of the austenitic transition. (b) For a heating/cooling rate of 5 K/ps the hysteresis has vanished.

ite temperature increases and the martensite temperature decreases. Fig. 8.8 quantifies the dependence of the martensite (austenite) temperature on the heating (cooling) rate.

In addition, with increasing rate, the transformation needs more time. This is seen most clearly in the almost 100 K span of the temperatures which the martensite transformation requires for completion in Fig. 8.7(a) for the highest cooling rate. The simulation data for dT/dt = 3 and $= 4$ K/ps are almost identical. When further increasing the rate to 5 K/ps,

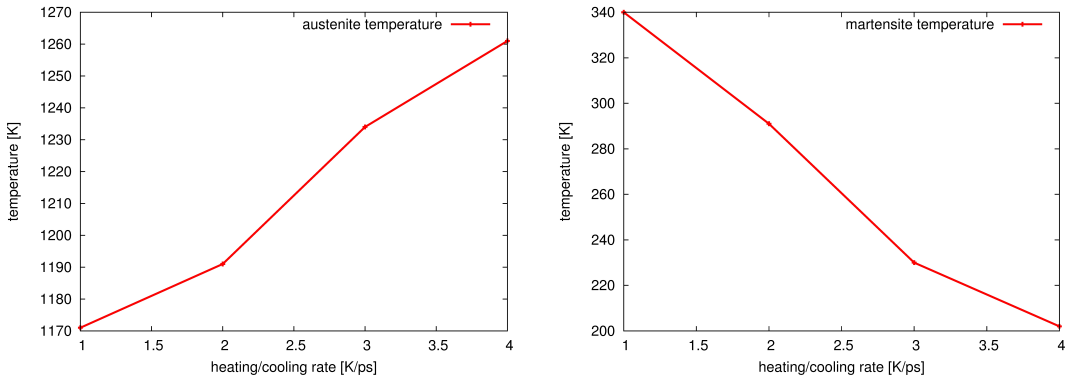

(a) (b)

Figure 8.8: Dependence on the (a) austenite and (b) martensite temperature on the heating/cooling rate.

the thermal expansion and contraction follow the same pathway, see Fig. 8.7(b); the phase transitions are suppressed.

8.3 Conclusions

This chapter approached the austenitic and martensitic solid-solid phase transformation in the Fe-C system as a function of the C content. Note few atomistic simulation studies are available for the phase transition in Fe-C system.

When subjecting the Fe-C system to a heating/cooling cycle, the martensitic and the austenitic phase transformation occur at well defined temperatures and spontaneously transform the entire crystallite. Both the austenite and martensite temperature decrease with increasing C content. These results are in agreement with the experimental finding. In addition, a strong dependence of the transition temperature on the actual positions of the C interstitial atoms was found; it is due to the local stress exerted.

The stresses building up during the austenitic transformation are an order of magnitude smaller than that during the martensitic transformation. This is caused by the build-up of a regular twin structure in the austenite phase, which helps to release the high transformation stress. In addition, with increasing heating/cooling rate the phase transition is retarded; for extreme rates ($dT/dT \geq 5$ K/ps) it is suppressed.

Chapter 9

Martensitic and austenitic phase transformation in Fe-C nanowires

Nanoscale systems, due to their higher surface/volume ration, may exhibit drastically changed properties with respect to bulk materials, for instance with respect to their mechanical and magnetic behavior [6, 7, 8]. In addition, they may also exhibit different behavior in phase transitions. In fcc metals, pseudo-elasticity or shape memory behavior [127, 128, 137, 138] as well as stress-induced phase transitions [139] have been discussed. Ma *et al.* [140, 141] reported on surface-tension-induced structural phase transitions. For bcc metal, Sandoval and Urbassek [17, 18, 19] studied both the temperature- and stress-induced phase transition in nanowires, and a rich variety of features, such as reorientation and back-transformation to the original structure at high strain, have been reported.

In this chapter, the phase transition in Fe-C nanowires will be studied by using molecular dynamics simulation. Both the austenitic and martensitic phase transition will be studied. The influence of the C-concentration, the wire diameter and an axial tensile load on the phase transitions will be investigated. The pathway of the transformations occurring will be analyzed.

9.1 Methodology

The method of classical atomistic simulation is used to study the phase transitions in Fe-C nanowires. The cylindrical nanowires have a diameter of D = 4.68 nm and a length of 20.88 nm; they are prepared in the bcc structure. The cylinder axis is oriented along $[111]$ direction; periodic boundary conditions are used in this direction. The surface of the nanowire has free boundaries. The total number of Fe atoms amounts to 30 808. C atoms are inserted randomly in the octahedral interstitial sites. Fig. 9.1 shows the setup of the

simulation. Six different atomic concentration of C (0 at%, 0.2 at%, 0.5 at%, 0.8 at%, 1.0 at% and 1.2 at%) are investigated.

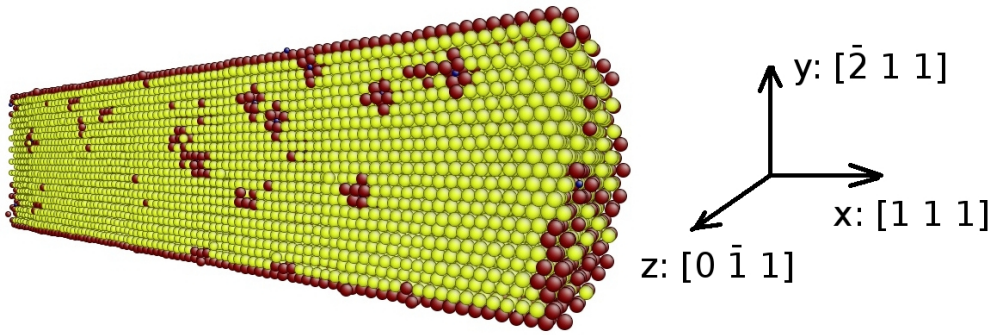

Figure 9.1: Setup of the nanowire sliced along the $(0\bar{1}1)$ plane. Colors denote the local crystal structure. Yellow: bcc; red: unknown; small blue spheres: carbon atoms.

Fe atoms interact via the Meyer-Entel interaction potential [31] with each other. The C-Fe interaction is taken from the work of Johnson *et al.* [73]. Finally, C atoms interact each other via the Tersoff potential [130].

The systems are relaxed for 100 ps in an NPT ensemble at a temperature of 50 K with pressure control (0 GPa) in the axial direction. After equilibration, a heating/cooling cycle is performed: The temperature is increased from 50 K to 1000 K and then decreases back to 50 K in an NPT ensemble; the heating/cooling rate was chosen as 1 K/ps. The temperature is controlled by a Nosé-Hoover thermostat. The length change of the nanowire is monitored. Sudden jumps are indications of solid-state phase transformations.

Besides the standard diameter of D = 4.68 nm, diameters of 2.8, 6.9 and 9.2 nm are investigated; in these cases the C-concentration is fixed at 0.5 at%.

In order to study the dependence of the transformation on an axial tensile stress, 5 different stresses from 0.5 GPa to 3 GPa are applied to the wire in axial direction. In these cases, the wires have the standard diameter of 4.68 nm and a concentration of 0.5 at%.

All calculations are performed with the open-source LAMMPS code [85]. The local atomic structure is determined by common neighbor analysis (CNA) [52].

9.2 Results and discussion

9.2.1 Austenitic and martensitic transition

Firstly, the C concentration dependence of the transition temperature in the Fe-C nanowires will be discussed. Fig. 9.2 displays the change of the nanowire length with temperature in the heating/cooling cycle. Note first that wires with higher C concentration are longer after relaxation; this is due to the volume expansion caused by C atom insertion. Upon

heating, the wire expands until at around 800 K, the length jumps suddenly; this indicates a phase transition from the bcc to the close-packed (cp) phase. As discussed in detail below, the cp phase is a mixture of fcc and hcp fractions. Upon cooling, the system contracts until at around 500 K and the length jumps back, indicating the transformation to the bcc phase. In analogy to the transitions in the bulk Fe-C system in the last chapter, the hysteresis observed here is characteristic for first-order structural phase transformations.

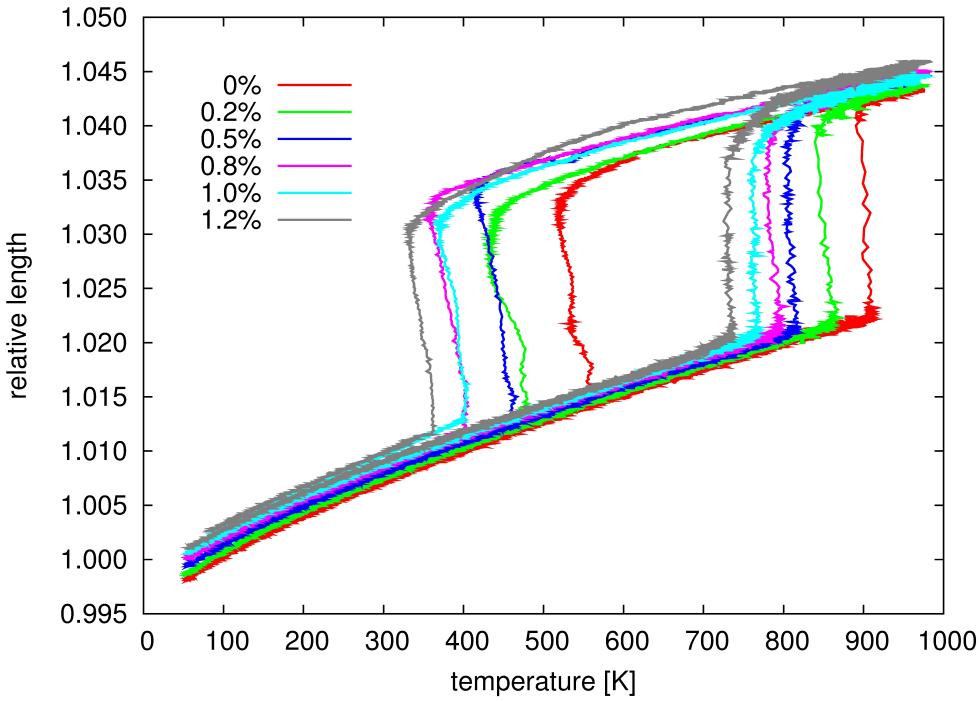

Figure 9.2: Dependence of wire length on temperature during a heating/cooling cycle. C concentration is indicated in the legend. Data normalized to the length of the nanowire before relaxation.

The data in Fig. 9.2 demonstrate a systematic dependence of the transition temperatures with C content; both austenitic and martensitic temperatures decrease with increasing C concentration. This trend is systematically seen for the austenitic temperature, but appears more irregular for the martensite temperature, where e.g., the curves for 0.8 and 1.0 at% C are almost coincide. These irregularities are due to the statistical distribution of C atoms in the nanowire; different initial distributions give rise to different local stresses which influence the transformation. The austenitic transformation, occurring at higher temperature, is less influenced.

The width of the transformation is only 10 K, and hence the transformations are completed within 10 ps; the C content has no effect on the transformation speed.

Fig. 9.3 quantifies the austenite and martensite temperatures determined from Fig. 9.2; here the average temperature, at which the nanowire length jumps, is taken as the austenite and martensite temperature, respectively. The prime result is that both the martensite and

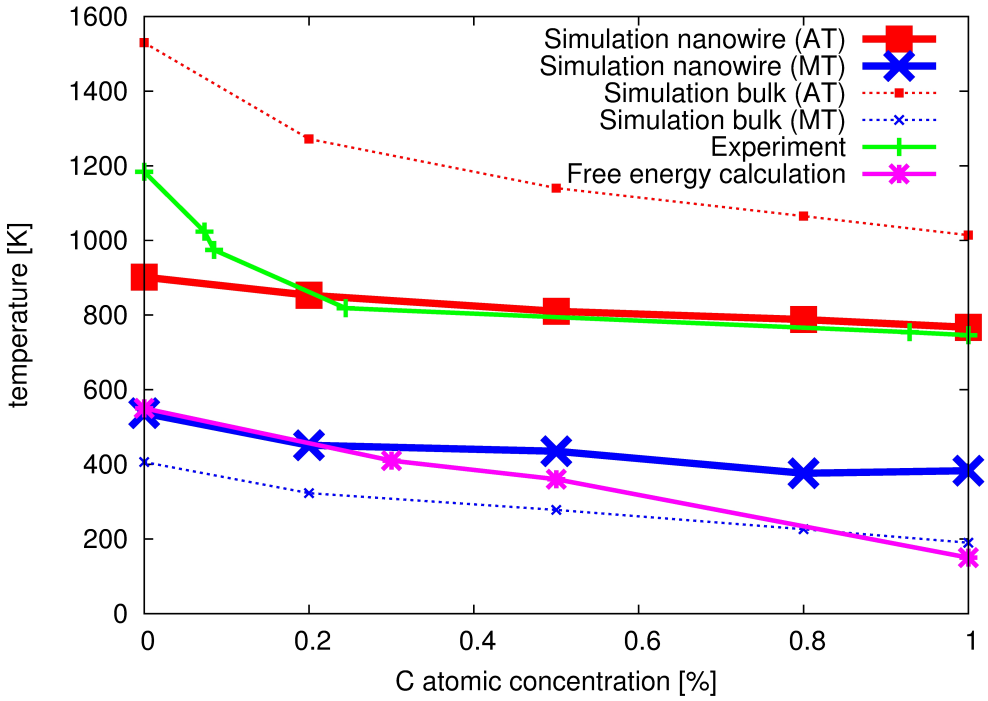

Figure 9.3: The austenite (AT) and martensite (MT) temperature of nanowires in dependence of C concentration. Data are compared to results for bulk systems: simulations (Fig. 8.3), experimental values [134] and free energy calculations [135].

the austenite temperatures decease systematically with increasing C concentration. The simulation results are compared with simulation data (Fig. 8.3) obtained for a bulk Fe-C system. The same trend is observed in the nanowire as in the bulk system; however, the hysteresis is considerably smaller. The reason hereto is that in the bulk, the kinetics of the phase transformation is strongly hindered due to the constraints set by the environment (implemented as periodic boundaries in the simulation). In the nanowire, in contrast, the free surfaces facilitate the phase transformation. In particular phase nucleation may easily occur at the surfaces due to the free volume available there.

In addition, data for the equilibrium values of the bcc-fcc phase transition [135] are plotted in Fig. 9.3; these have been taken from free-energy calculations and determine the temperature at which the free energies of fcc and bcc phase are equal. This temperature has been determined previously for pure Fe in the Meyer-Entel potential to be 550 ± 50 K [18, 38, 69]; again with increasing C content the equilibrium transition temperature decreases. Experimental data [134] show the same trend, see Fig. 9.3.

Figure 9.4 displays snapshots of the nanowire (0.5 at% C concentration) at several temperatures during the heating/cooling cycle. Both axial and cross-sectional slices are displayed. Fig. 9.4(a) shows the status after relaxation. Fe atoms, which cannot be identified correctly, are situated either on the wire surface or in the vicinity of C atoms, where the strong strain fields prevent the proper structure identification. Fig. 9.4(b) shows

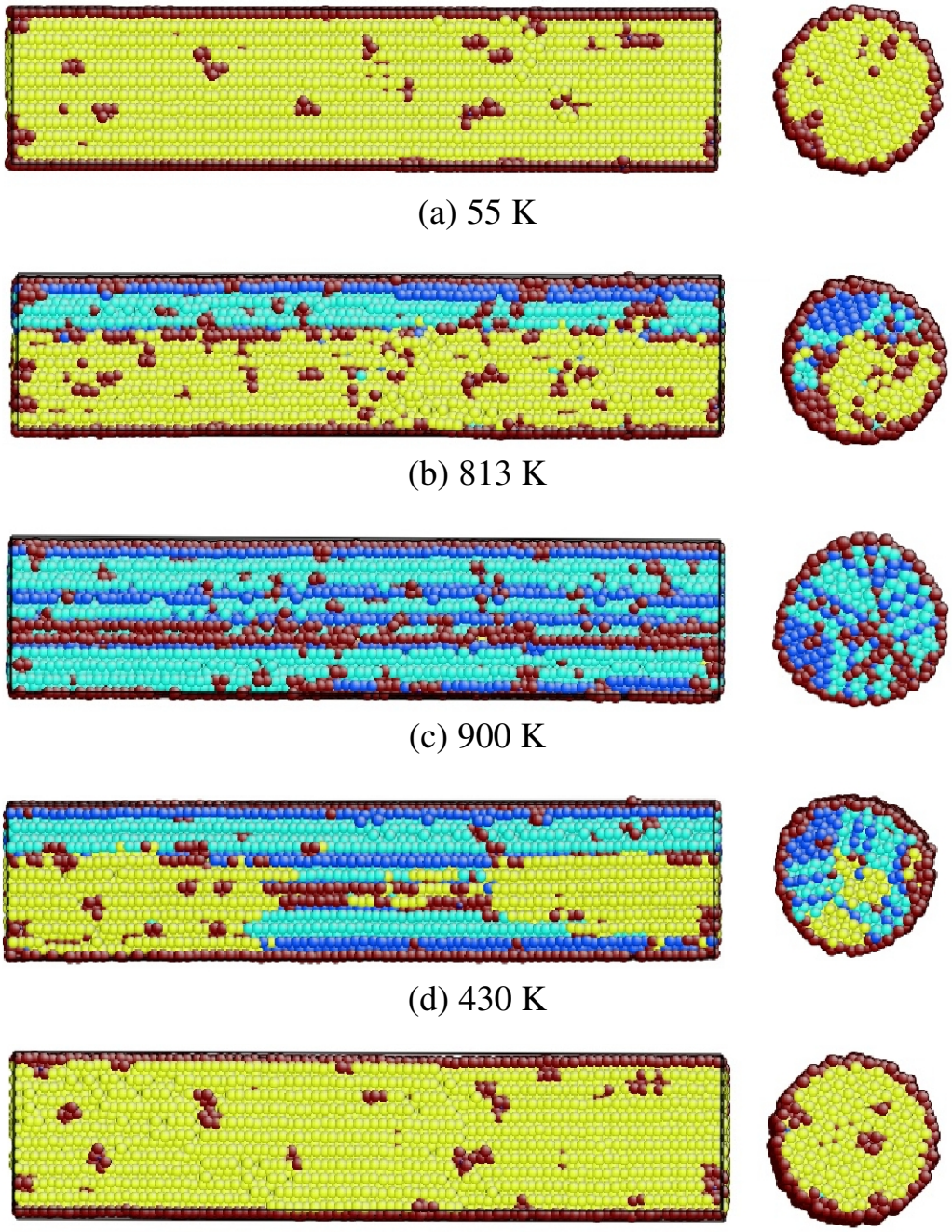

(a) 55 K

(b) 813 K

(c) 900 K

(d) 430 K

(e) 420 K

Figure 9.4: Snapshots of the nanowire with 0.5 at% C concentration for various temperature. Left: axial slice along the $(0\bar{1}1)_{\mathrm{bcc}}$ plane; right: cross-sectional slice. Colors denote the local crystal structure. Yellow: bcc; dark blue: fcc; light blue: hcp; red: unknown; small blue spheres: C atoms.

the wire during the ongoing austenitic phase transition. The new phase nucleates at the nanowire surface, because atoms at the surface have sufficient space for moving into new lattice sites. The new phase spreads until the entire wire is transformed, Fig. 9.4(c). Phase transformation results in a mixture of fcc and hcp phases (cp). Such a mixture has already

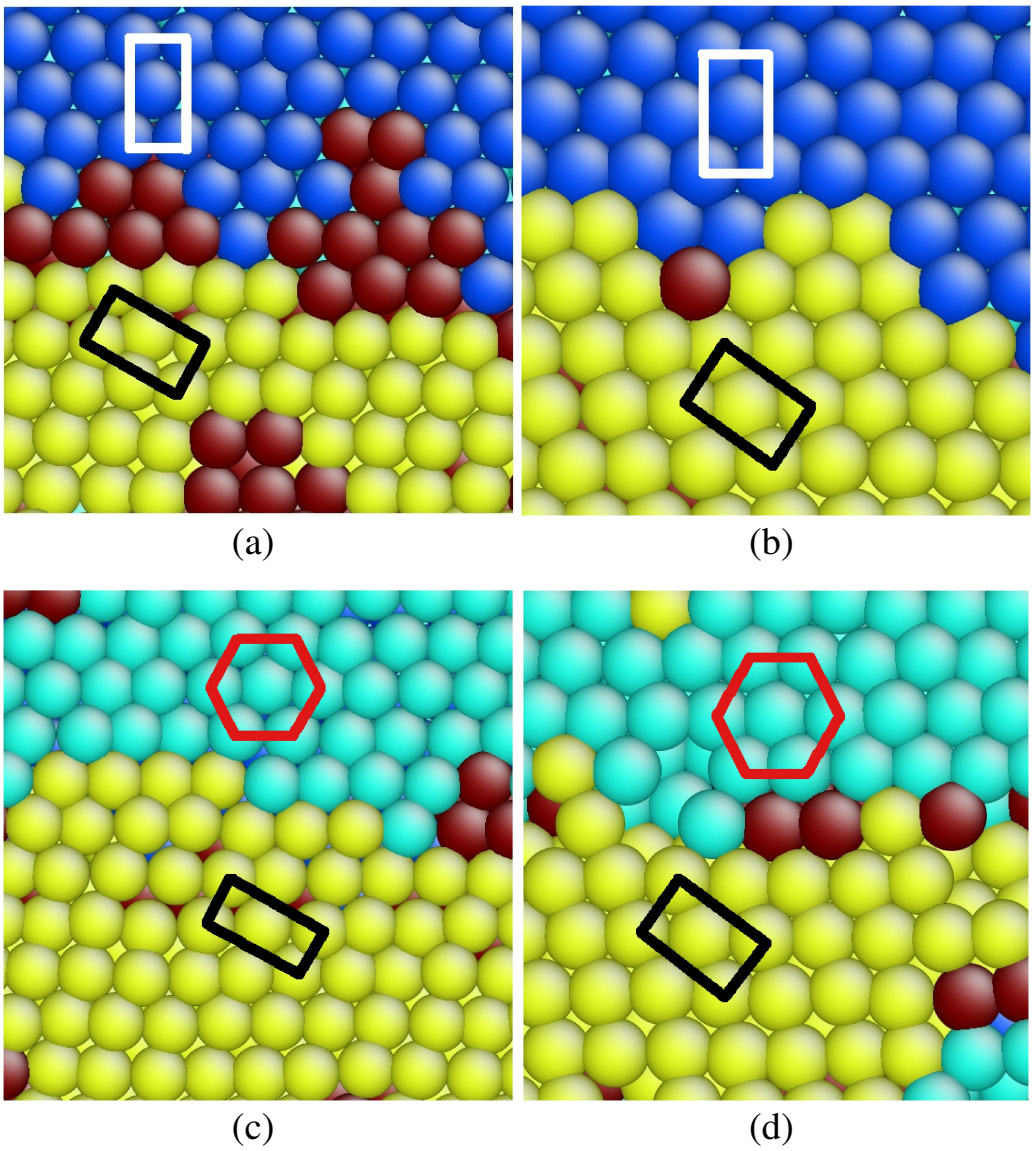

Figure 9.5: Close-up of the ongoing transformations: (a) austenitic and (b) martensitic transition bcc $\leftrightarrow$ fcc. In both cases, the bcc plane is $(0\bar{1}1)$ and the fcc plane is (111). The horizontal direction is the wire axis $[111]_{\mathrm{bcc}} \parallel [\bar{1}10]_{\mathrm{fcc}}$, and the upward direction is $(\bar{2}11))_{\mathrm{bcc}} \parallel (11\bar{2})_{\mathrm{fcc}}$. (c) austenitic and (d) martensitic transition bcc $\leftrightarrow$ hcp. In these cases, the bcc $(0\bar{1}1)$ plane corresponds to the (001) hcp plane. The horizontal direction is the wire axis $[111]_{\mathrm{bcc}} \parallel [010]_{\mathrm{hcp}}$, and the upward direction is $(\bar{2}11)_{\mathrm{bcc}} \parallel (210)_{\mathrm{hcp}}$. Colors denote the local crystal structure as in Fig. 9.4. The black (white) rectangle identifies a bcc (fcc) unit cell and the red hexagon identifies the hexagonal structure in $(001)_{\mathrm{hcp}}$ plane.

been observed in pure Fe nanowires [18]; note that the energy difference between the fcc and the hcp phase in the Meyer-Entel potential amounts to only around 4 meV/atom [69].

Fig. 9.4(d) captures the nanowire during the martensitic transformation. Again the transformation starts at the surface and spreads out; in addition, the highly defective core acts as a nucleation center for the bcc phase. After completion of the transformation,

Fig. 9.4(e), the wire looks almost identical to its initial state, Fig. 9.4(a). Note that the transformation only takes 10 K, corresponding to 10 ps.

Figure 9.5 gives insight into the transition pathway by showing the crystallographic relationship between the original bcc and the newly formed fcc phase. The snapshot have been obtained during the transformation phases, where both phase coexist in the wire. The snapshot demonstrates that the two phases obey the Kurdjumov-Sachs (K-S) relationship [34]:

$$(0\bar{1}1)_{\mathrm{bcc}} \parallel (111)_{\mathrm{fcc}} \qquad \text{and} \qquad [\bar{2}11]_{\mathrm{bcc}} \parallel [11\bar{2}]_{\mathrm{fcc}}.$$

It is well known [40] that low-carbon steels, like in the cases studied here, transform according the K-S relationship, while the high-carbon steels obey the Nishiyama -Wassermann (N-W) relationship [32, 33]:

$$(011)_{\mathrm{bcc}} \parallel (111)_{\mathrm{fcc}} \qquad \text{and} \qquad [01\bar{1}]_{\mathrm{bcc}} \parallel [11\bar{2}]_{\mathrm{fcc}}.$$

During the transformation also the hcp phase is created. As Fig. 9.5(c) and (d) show, the bcc $\leftrightarrow$ hcp transition follows the Burgers orientation relations [107], which satisfy

$$(0\bar{1}1)_{\mathrm{bcc}} \parallel (001)_{\mathrm{hcp}} \qquad \text{and} \qquad [111]_{\mathrm{bcc}} \parallel [010]_{\mathrm{hcp}}.$$

Note that the K-S and Burgers pathways are also found for other C concentrations investigated.

9.2.2 Dependence on wire diameter

In this subsection, the dependence of the phase transition on the diameter of the wire will be discussed. Fig. 9.6 shows the relative length-temperature plots during a heating/cooling cycle for nanowires of various diameters in the range of D = 2.8-9.2 nm. In all cases, both austenitic and martensitic phase transition can be observed. Firstly, the nanowires with diameter $D \geq 4.6$ nm are taken into account. With increasing diameter the hysteresis widens; this effect is particularly pronounced for the martensitic transformation. Thus, with increasing diameter, the transformation temperatures have the tendency of approaching the bulk values, cf. Fig. 9.3. Sandoval and Urbassek [17] set up a thermodynamic model which explains the increase of the austenitic temperature with wire diameter. It is based on including explicitly the specific surface energy for curved surfaces into the free-energy equilibrium of a wire.

The thinnest nanowire with a diameter of only 2.8 nm shows a different behavior. It shortens during the austenitic transformation and increases its length during the martensitic transformation, in gross contrast to the thicker wires. The reason for this different

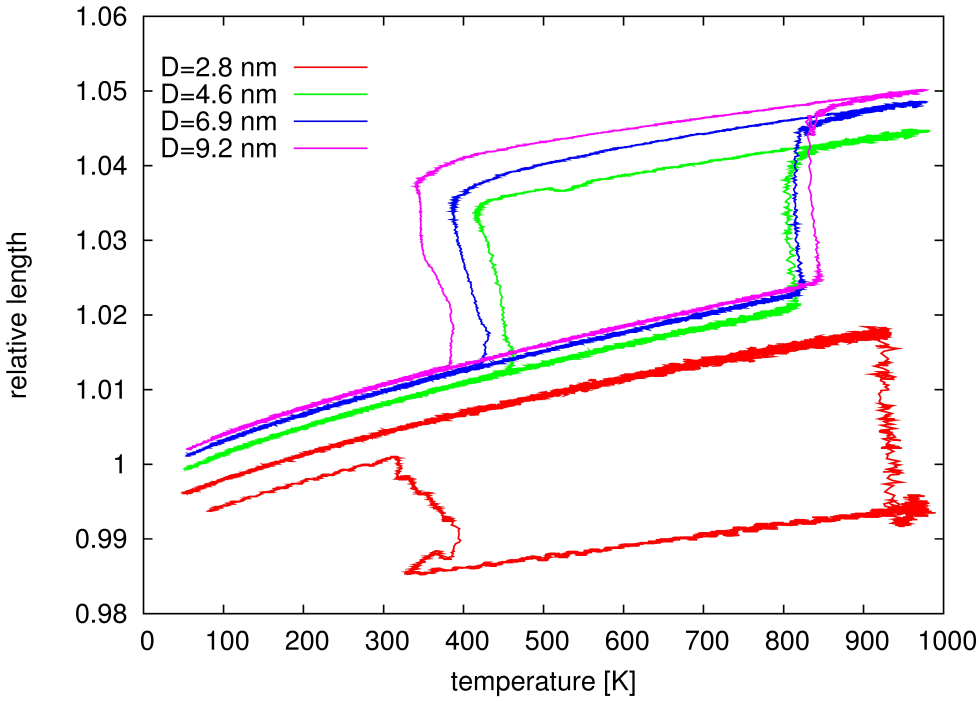

Figure 9.6: Dependence of wire length (0.5 at% C concentration) on temperature during a heating/cooling cycle. Wire diameter D is indicated in the legend. Data normalized to the length of the nanowire before relaxation.

behavior is illuminated by the snapshots given in Fig. 9.7. Fig. 9.7(a) shows the nanowire immediately after the austenitic transition and the (b) displays the status immediately after the martensitic transition. The nanowire buckles during the austenitic transition and thereby changes its shape macroscopically, leading to a smaller effective length. The microstructure of the wire is strongly different from that of larger wires. It now shows a bamboo-like structure, in which fcc and hcp phases keep alternating, including a rich percentage of stacking faults. Inspection of a video of the deformation process shows that the new phase penetrates immediately throughout the cross section of the wire, rather than being restricted to the surface for the thicker wires. From that cross-section the phase transformation propagates in axial direction. Since the lattice orientation is oblique to the original bcc orientation, this growth leads to wire bulking, which must be counteracted by the formation of novel grains. The transformation generates internal stresses which displace the fcc planes and induce the formation of stacking fault planes.

While in the thicker wires nucleation occurred at the surface, leading to a single crystalline wire, in particular for the martensitic phase transformation. The large surface/volume ration of the ultrathin wire gives rise to this novel axial growth scenario.

Upon cooling, the ultrathin wire transforms to its single crystalline original shape, Fig. 9.7(b). Only a single glide occurred, thus gives evidence of the vivid deformation history of the wire. In this sense, this ultrathin wire acted like a shape-memory metal,

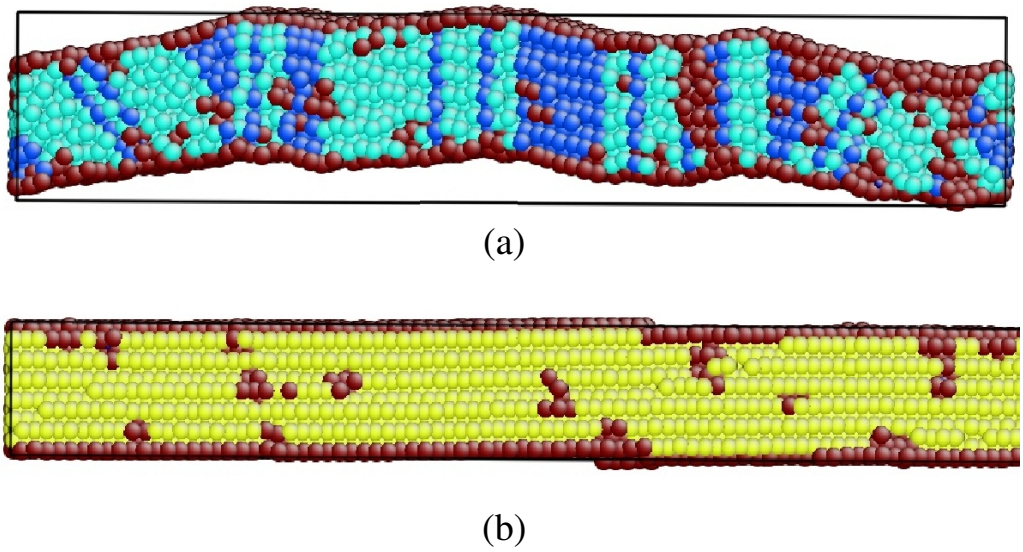

(a)

(b)

Figure 9.7: Snapshots of the thinnest nanowire (diameter D = 2.8 nm) after the (a) austenitic and (b) martensitic transformation. C concentration 0.5 at%. Colors denote the local crystal structure as in Fig. 9.4.

which found its original form ever after considerable deformation. Note that, a simulation with an ever thinner wire D = 2 nm, gave similar results as those presented here.

9.2.3 Dependence on axial load

External stress may influence the phase transformation behavior. The influence of an external axial tensile stress p on the transformation is investigated in Fig. 9.8. Note that the wire length immediately after relaxation (data for temperature 50 K in Fig. 9.8) increase systematically with p, as was to be expected. For tensile loads $p \leq 1.5$ GPa the heating/cooling cycle is qualitatively similar to the results discussed above, Fig. 9.2. Quantitatively, both the austenite and the martensite temperatures are decreased. It is argued that for increased tensile load, the material is strained giving more room for the transformation to occur.

At higher stresses, the austenitic transformation is still observed, but the martensitic back-transformation is suppressed. The snapshots of the cooled down wires, Fig. 9.9, show the process occurring. For p = 2 GPa, the wire fails; plastic deformation resulted in the formation of a neck. For p = 3 GPa, the phase transformation is inhibited and retained austenite is observed in the interior of the wire. The nanowire shows a complex mixture of bcc, fcc and hcp phases.

A reorientation of the bcc phase takes place in the wire, see Fig. 9.10. The original axis was oriented along the $[111]_{\mathrm{bcc}}$ and changes to $[100]_{\mathrm{bcc}}$. The fcc phase shows no reorientation while it exists. No plasticity is observed at this axial load, demonstrating that

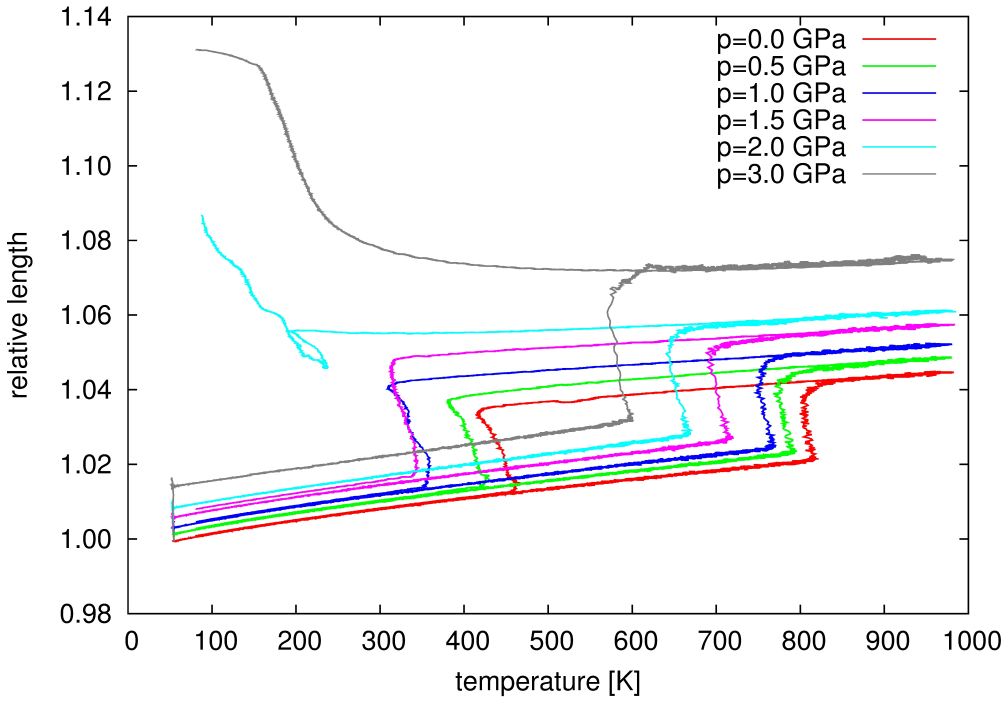

Figure 9.8: Dependence of wire length (0.5 at% C concentration) on temperature during a heating / cooling cycle. Wire diameter D is 4.68 nm. Data normalized to the length of the nanowire before relaxation.

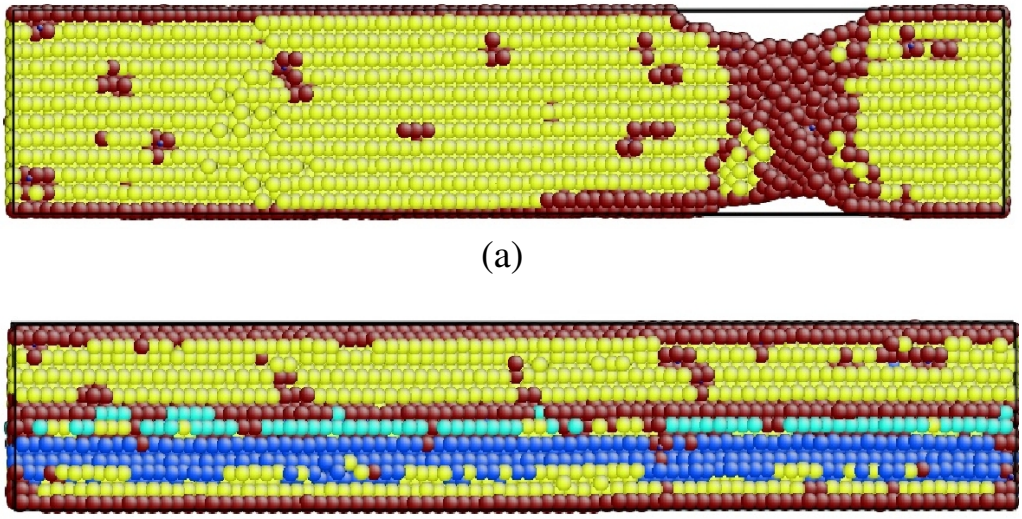

(a)

(b)

Figure 9.9: Snapshots of the nanowire (diameter D = 4.68 nm) at the end of the heating/cooling cycle for an applied load of (a) 2 GPa, (b) 3 GPa. Colors denote the local crystal structure as in Fig. 9.4.

the multiphase mixture has a high tensile strength, which is caused by the reorientation process.

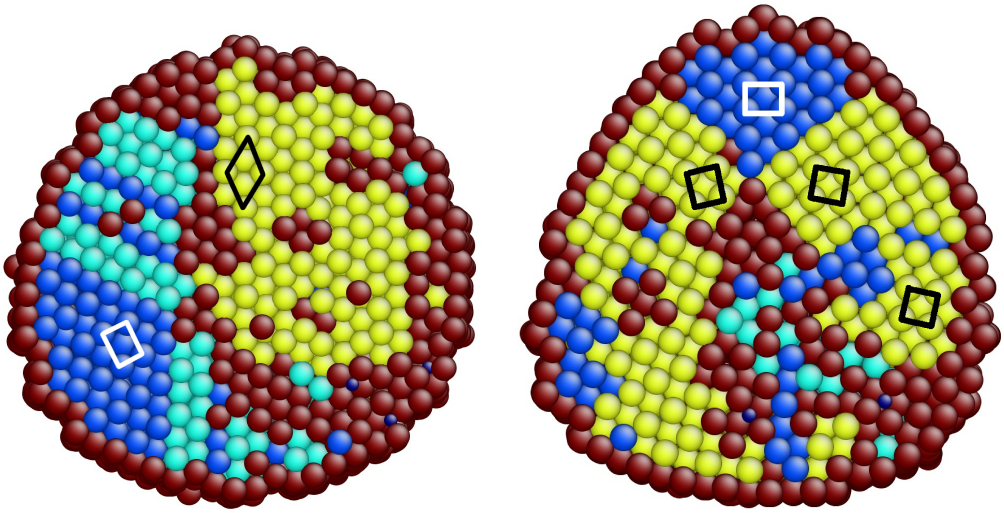

(a) (b)

Figure 9.10: Cross-sectional view of (a) the unstressed wire during the martensitic transformation, and (b) of the wire under p = 3 GPa axial stress at the end of the heating/cooling cycle (80 K). In (a) the plotted cross-sectional plane is the $(111)_{\mathrm{bcc}}$ plane and $(\bar{1}10)_{\mathrm{fcc}}$ plane. The black rhombus (white rectangle) denote bcc (fcc) unit cells. In (b) the plotted cross-sectional plane is $(110)_{\mathrm{bcc}}$ and $(\bar{1}10)_{\mathrm{fcc}}$. The wire underwent a reorientation. The black squares (white rectangles) denote bcc (fcc) unit cells. Colors denote the local crystal structure as in Fig. 9.4.

9.3 Conclusions

In this chapter, the austenitic and martensitic phase transition in Fe-C nanowires were studied as a function of the C content. In addition, the dependence of wire diameter and axial load on the phase transformation was discussed.

When subjecting the nanowire to a heating/cooling cycle, sudden length changes signal the martensitic and the austenitic phase transformation. Martensite and austenite temperature decrease with increasing C content. There results are in agreement with the experimental finding that C stabilizes the close-packed phase. The martensitic temperature is higher and the austenite temperature is lower, than that in bulk Fe-C (Chapter 8) alloys.

With increasing wire diameter, the transition temperatures tend to their bulk values. For not too thin wires, the transformation starts from the surface and transforms quickly the wire. Bcc and fcc phase obey the Kurdjumov-Sachs orientation relationship. For ultrathin wires (diameter $D \leq 2.8$ nm), the austenite transformation proceeds in axial and the wire is transformed to a nanocrystalline bamboo-like structure of hcp and fcc phases. In consequence the wire buckles. Upon cooling, it (almost) assumes its initial form (shape memory).

Under high axial tensile stress the nanowire can still undergo the austenitic transformation. However, the martensite transformation is partially suppressed, leading to strong plastic deformation. Under the highest loads, the austenite transforms only partially back to the martensite; a complex mixture of bcc, fcc and hcp phase was obtained in the nanowire. A reorientation of the bcc phase takes place in the wire. This reorientation causes a high tensile strength of the multiphase mixture.

Chapter 10

Summary

In the present work, the phase transitions in different Fe/Fe-C systems were studied by using the classical atomistic simulation. This work can be summarized as follows:

In Chapter 2, the generals of material science were represented. This chapter involved the general information about pure Fe and Fe-C systems. Three different types of phase boundaries and the martensitic phase transformation in Fe system were explained in detail.

In Chapter 3, the basic idea of the classical atomistic method [molecular dynamics (MD) simulation] was introduced. Some basic concepts in MD, such as the boundary conditions and the ensembles, were discussed. The detectors, which were used for simulations in this work, were explained in detail. In addition, some interatomic potentials for describing the Fe-Fe and Fe-C interactions were presented. Some properties of the Meyer-Entel potential [31], which is the only one in the class of EAM potentials can model both the $\alpha \rightarrow \gamma$ and $\gamma \rightarrow \alpha$ phase transition, were introduced. This potential was compared with some other Fe potentials and some successful applications of it were listed.

Chapter 4 treated the temperature-induced phase transitions in an Fe bicrystal containing a bcc/fcc interface with N-W orientation geometry. Misfit dislocations were found at phase boundary growing into the bcc side after the relaxation. Interface energy without contribution of the misfit dislocations amounts to 0.96 Jm^{-2}, which is in fair agreement with the experimental finding. Both homogeneous and heterogeneous nucleations of the bcc phase were observed during the martensitic phase transition at a temperature of 100 K. At the high temperature of 1300 K, the phase transition does not take place in the first 20 ps (incubation period), and only heterogeneous nucleation of the cp phase could be observed. The interface propagates with an approximately constant velocity of 24 m/s at 100 K , while at 1300 K the interface velocity after the incubation period amounts on average to 180 m/s with a maximum value of 450 m/s.

Chapter 5 is an extension of chapter 4. The influence of shear strain on phase transitions of Fe were studied in a biphasic fcc/bcc crystal, which is (meta-) stable in the temperature range investigated. At 300 K, both heterogeneous and homogeneous growth of the stable bcc was observed. Increased the temperature to 400 K, only heterogeneous growth could be found. Above the transition temperature, the interface does not move. The phase transition occurs homogeneously from the bulk material.

In Chapter 6, the competition of homo- and heterogeneous phase growth was studied by using biphasic crystals containing bcc/fcc interfaces with different size. It was found that the creation of nuclei in the bulk phase (homogeneous nucleation) hinders the interface movement (heterogeneous nucleation), and vice versa. Depending on the available volume, the two mechanisms contribute competitively to the phase transition. In addition, the influence of the interface geometry on the phase transition was investigated in this chapter; for the N-W geometry, the interface still has a globally planar form during the interface motion, while it assumes a dendritic growth structure for the K-S geometry.

The strain-induced phase transition of thin Fe films was investigated in its dependence on crystal orientation and film thickness in Chapter 7. The strain-induced phase transition was divided into four steps: (i) a bcc $\rightarrow$ hcp transition; (2) the partial back transformation to the bcc phase; (iii) grain modification of the cp phase; (iv) intergranular fracture. Depending on the crystal orientation, the transformed cp phase behaves differently to a further increase of the strain. Two typical mechanism were found here: partial back transformation to the bcc phase, but with reoriented grains, or grain refinement. Film thickness does not influence the sequence of film transformation and grain reorientation processes occurring. In thinner films, a faster nucleation of the new phase was observed.

Chapter 8 approached the temperature-induced phase transitions in Fe-C bulk systems. When subjecting the Fe-C system to a heating/cooling cycle, it was found that both the martensite and austenite temperature decrease with increasing C content. In addition, the actual positions of the C interstitial atoms influence the transition temperature. It was also observed that the phase transitions cause high stresses building up, which can be released by twinning during the austenitic phase transition. In contrast, this twin structure is resolved during the martensitic phase transition; this causes an order of magnitude higher transformation stress than that during the austenitic phase transition. Finally, the phase transition is retarded with increasing heating/cooling rate.

In Chapter 9, the austenitic and martensitic phase transition was studied in Fe-C nanowires by subjecting the wire to a heating/cooling cycle. As found in last chapter, both the austenite and martensite temperature decrease with increasing C content. Due to the surface effect, the martensite temperature is higher and the austenite temperature is lower than that in bulk systems. In addition, the phase transitions obey the K-S orientation relationship. The length-temperature hysteresis becomes wider with increasing wire

diameter. For diameter from 4.6 to 9.2 nm, the transformation starts from the surface and transforms quickly the whole wire. For diameter $\leq$ 2.8 nm, a totally different behavior of transformation was observed: A bamboo-like structure of hcp and fcc phase was found during the austenitic phase transition, which proceeds in axial direction. This leads to wire buckling. Upon cooling, the wire assumes its initial form during the martensitic phase transition (shape memory effect). Under axial tensile stress of 2 GPa, the nanowire can still undergo the austenitic phase transition, while the martensitic phase transition is partially suppressed; this leads to the formation of a neck. Increasing the tensile stress to 3 GPa, the austenitic phase transforms only partially back to the martensitic phase. A reorientation of the bcc phase was observed here, which gives the multi-phase mixture a high tensile strength.

Zusammenfassung

In der vorliegenden Arbeit sind die Phasenumwandlungen in verschiedenen Fe/Fe-C Systemen mit Hilfe von der klassischen atomistischen Simulation untersucht worden. Die Arbeit kann im Folgenden zusammengefasst werden:

In Kapital 2 sind die Grundlagen von Werkstoffwissenschaft vorgestellt worden. Das Kapital umfasste die allgemeinen Informationen von reinen Fe und Fe-C Systemen. Drei verschiedenen Typen von Phasengrenzen und die martensitische Phasenumwandlung sind in Detail erklärt worden.

In Kapital 3 ist die Grundidee von der Molekular Dynamik Simulation erklärt worden. Einige Grundbegriffe, wie Randbedingungen und Ensembles, wurden vorgestellt. Die Methoden, die in Rahmen von dieser Arbeit benutzt wurden, sind da ausführlich erklärt worden. Außerdem sind einige Potentiale, die zur Beschreibung der Wechselwirkungen zwischen Fe-Fe und Fe-C dienen, präsentiert worden. Die Eigenschaften vom Meyer-Entel Potential [31], das einzige Potential für Fe vom EAM Typ, das nicht nur $\alpha \leftrightarrow \gamma$ Umwandlung, sondern auch $\gamma \rightarrow \alpha$ Umwandlung beschreiben kann, wurden vorgestellt. Das Potential wurde mit einigen anderen Potentialen von Fe verglichen und einige erfolgreiche Anwendungen sind aufgelistet worden.

Kapital 4 betrachtete die temperatur-induzierte Phasenumwandlung von einem bikristallinen Fe System. Das System beinhaltet eine bcc/fcc Phasengrenzen in N-W Geometrie. Durch Bildung von Fehlpassungsversetzungen ändert sich die Gitterstruktur an der Grenzfläche. Die Energie der Phasengrenze ohne Wirkung von Versetzungen beträgt 0.96 Jm/s^2 mit einer guten Übereinstimmung mit Experiment. Wenn die Temperatur nah zur Gleichgewichtstemperatur gewählt ist, findet die Phasenumwandlung in Zeitrahmen von Molekulardynamik nicht statt; hier ist die Umwandlungskinetik langsam und die Aktivierungsenergie zwischen zwei Phasen ist hoch. Nur zwei Temperaturen wurden gefunden, bei den die Phasenumwandlung untersucht werden kann. Die martensitische Phasenumwandlung ($fcc \rightarrow bcc$) ist untersucht worden bei einer Temperatur von 100 K. Bei dieser Temperatur raut die Grenzfläche geringfügig auf und bewegt sich mit einer Geschwindigkeit von 24 m/s. Gleichzeitig findet homogene Keimbildung von der bcc Phase im Bulk fcc Korn statt. Bei hohen Temperatur von 1300 K wurde die austenitische Phasenumwandlung beobachtet. Hier ist das Keimwachstum behindert für

ca.20 ps und keine homogene Keimbildung kann beobachtet werden. Beide Merkmale können durch eine kinetische Energiebarriere zwischen den zwei Phasen erklärt werden. Die Energiebarriere ist größer bei hoher als bei niedriger Temperatur. Die Grenzflächengeschwindigkeit nach der Inkubationsphase beträgt durchschnittlich 180 m/s mit einem maximalen Wert von 540 m/s.

Kapital 5 ist eine Erweiterung von Kapital 4. Externe Dehnungen sind auf dem biphasischen fcc/bcc System im Temperaturbereich, bei dem das System (meta-) stabil ist, angelegt worden. Eine starke Abhängigkeit von der Temperatur wurde gefunden. Bei niedriger Temperatur, die weit entfernt von der Gleichgewichtstemperatur im Meyer-Entel Potential ist, konnten sowohl heterogene als auch homogene Wachstum von der stabilen bcc Phase beobachtet werden. In der Nähe von Umwandlungstemperatur wurde nur heterogenes Wachstum gefunden bei einer Temperatur von 400 K. Dies stimmt mit der reduzierten Triebkraft für Keimbildung der stabilen Phase überein. Oberhalb der Umwandlungstemperatur findet homogene Phasenumwandlung statt, wobei die bcc Phase zur dichtgepackten (cp) Phase transformiert. In diesem Fall bewegt sich die Grenzfläche nicht. In Abwesenheit von Dehnung ist das System stabil - zumindest für alle untersuchte Temperaturen im zeitlichen Rahmen zugänglich in den Simulationen . Diese Ergebnisse verdeutlichen somit, wie die externe Dehnung als Triebkraft für Initiierung der $bcc \rightarrow fcc$ Phasenumwandlung wirkt. Darüber hinaus zeigen die Ergebnisse, wie die Änderung der Umgebungstemperatur die Wirkung der angelegten Dehnung in einer komplexen Weise beeinflusst und insbesondere das Zusammenspiel zwischen homogenen und heterogenen Umwandlungspfade beeinflusst.

In Kapital 6 ist die Konkurrenz zwischen homo- und heterogenen Phasenwachstum in Abhängigkeit von der Systemgröße in einem biphasischen System untersucht worden. Wie in Kapital 5 ist die Phasenumwandlung bei zwei Temperaturen (100 K und 1300 K) untersucht worden. Im Allgemeinen tragen sowohl homogene Keimbildung als auch heterogenes Wachstum bei Grenzflächenbewegung bei. Die zwei Mechanismen sind konkurrierend, wobei die Bildung von Keimen in der Bulk-Phase (homogene Keimbildung) die Grenzflächenbewegung (heterogene Keimbildung) hindert, und umgekehrt. Die martensitische Phasenumwandlung erfolgt durch sowohl homo- als auch heterogenes Phasenwachstum. Während des Wachstums wird die Grenzfläche grob. Bei N-W Geometrie hat die Grenzfläche noch eine global planare Form, während eine dendritische Struktur bei der K-S Geometrie auftritt. Außerdem wurde eine deutliche Beeinflussung von der Wachstumsart auf dem verfügbaren Volumen beobachtet: mit zunehmendem Volumen dominiert homogenes Wachstum über heterogenes Wachstum. Dies lässt sich einfach bestätigen, weil die Grenzflächengeschwindigkeit während des Wachstums abnimmt. Die physikalische Ursache hinter dem Verhalten kann so erklärt werden, dass eine Bildung eines Keims von der neuen Phase, die notwendig ist für homogenes Wachstum,

erleichtert wird, wenn ein größeres Volumen zur Verfügung steht. Bei der austenitischen Umwandlung wurde ein ähnliches, aber noch dramatischeres Verhalten beobachtet. In kleinem Volumen wurde homogene Keimbildung von der neuen Phase gar nicht gesehen, während in großem Volumen stabile Keime gebildet werden und zu Phasenwachstum beitragen. Bei der K-S Geometrie, die nur in einer mäßigen Größe untersucht wurde, wurde nur Phasenwachstum, das durch Grenzflächenbewegung erfolgt, beobachtet; die Grenzfläche zeigt wieder eine dendritische Struktur. Diese Ergebnisse sind relevant für zukünftige Studien der Phasenumwandlung sowohl aus einer physikalischen als auch einer methodischen Sicht. Außerdem wurde gezeigt, dass nicht nur in nanoskaligen Systemen, sondern auch in Bulk-Systemen das verfügbare Volumen für Umwandlung durch das Vorhandensein von Mikrostrukturen wie Korngrenzen eingeschränkt wurde. Die Phasenumwandlung kann in einer deutlich anderen Weise als in den makroskopischen Systemen ablaufen. Auf der anderen Seite können die Ergebnisse mitwirken bei Wahl der Größe des Sytems, in dem sich die Phasenumwandlung studieren lässt, wenn die atomistische Simulation verwendet wird.

In Kapital 7 ist die spannungs-induzierte Phasenumwandlung von Fe Dünnschichten in Abhängigkeit von Kristallorientierung und Schichtdicke untersucht worden. Das mechanische Verhalten von den Schichten, d.h., die Spannung-Dehnung Kurve weist darauf hin, dass eine komplexe Reihe von Prozessen in den Schichten stattfinden. Die Analyse der Variation des Phasengehalts in den Schichten mit zunehmender Spannung und die Inspektion von Momentaufnahmen während der Schichtenentwicklung ermöglicht die Identifizierung der Sequenz von Phasenumwandlungen, begleitet von Keimbildung neuer Körner und Kristallumorientierung, die für Schichtenentwicklung verantwortlich sind. Die spannung-induzierte Phasenumwandlung in Dünnschichten wurde in vier Schritte unterteilt. Sie tritt im Allgemeinen in dieser Reihenfolge auf (i) ein $bcc \rightarrow hcp$ Übergang, (ii) die teilweise Rückumwandlung in der bcc Phase, (iii) Korn-Modifikation der cp Phase, (iv) schließlich findet interkristalliner Bruch statt. Der Grund für diese komplexen Vorgänge liegt an die Bildung von hohen inneren Spannungen in der Schicht. Aufgrund der geringen Schichtdicke können die Spannungen nicht durch plastische Verformung abgebaut werden, d.h., nicht durch die Bildung von Versetzungen. Stattdessen findet Phasenumwandlung statt, bei der die Spannung abgebaut werden kann. Der Kristall transformiert sich vor allem in die hcp Struktur, die einen hohen Anteil von fcc Material (cp Phase) enthält. In allen untersuchten Fällen (Orientierungen) gehorcht die Umwandlung dem Burgers Mechanismus [107]. In Abhängigkeit von der Kristallorientierung reagiert die transformierte cp Phase unterschiedlich auf eine weitere zunehmende Spannung. Dabei werden zwei Pfade beobachtet: Teilweise Rückumwandlung in die bcc Phase, aber jetzt mit umorientierten Körnern, oder Kornverfeinerung. Schichtdicke spielt keine wichtige Rolle in der Reihenfolge der Phasenumwandlung- und Umorien-

tierungsvorgänge. Aufgrund der geringen Schichtdicke ist die Bildung von Versetzungen als Abhilfe zum Abbau der hohen Spannung nicht möglich. Allerdings wurde ein Einfluss der Schichtdicke auf die Umwandlungsgeschwindigkeit gefunden. Dünnere Schichten ermöglichen eine schnellere Keimbildung der neuen Phase; das hohe Oberflächen/Volumen Verhältnis in dünneren Schichten erleichtert die Keimbildung.

In Kapital 8 wurde die austenitische und martensitische Phasenumwandlung in Abhängigkeit von C-Gehalt im Fe-C-Bulk System betrachtet. Nur wenige atomistische Simulationsstudien stehen für den Phasenübergang im Fe-C System zur Verfügung. Bei einem Aufheizungs/Abkühlungs-Zyklus finden die austenitische und die martensitische Umwandlung bei eindeutigen Temperaturen statt, wobei der gesamte Kristallit spontan transformiert. Die Martensit- Temperatur nimmt mit zunehmenden C-Gehalt ab. Im Gegensatz erhöht sich die Austenit Temperatur mit zunehmendem C-Gehalt. Diese Ergebnisse sind in Übereinstimmung mit dem experimentellen Befund, dass C die fcc-Phase stabilisiert. Es wurde auch gezeigt, dass die Umwandlungstemperatur von den aktuellen Positionen der interstitiellen C-Atomen stark abhängig ist; das ist aufgrund der ausgeübten lokalen Spannung. Die Spannungen beim austenitischen Übergang sind eine Größenordnung kleiner als die beim martensitischen Übergang. Dies wird verursacht durch den Aufbau einer regelmäßigen Zwillingsstruktur in der Austenit Phase, wodurch die hohe Umwandlungsspannung abgebaut werden kann. Außerdem wird die Phasenumwandlung mit zunehmender Aufheizungs/Abkühlungs-Rate verzögert; bei extremen Raten ($dT/dT \geq 5K/ps$) wird die Umwandlung total unterdrückt.

In Kaptial 9 wurde die Phasenumwandlung in Fe-C Nanodrähten untersucht, in Abhängigkeit vom C-Gehalt. Zusätzlich ist die Abhängigkeit von Drahtdurchmesser und axialer Belastung diskutiert worden. Bei einem Aufheizungs/Abkühlungs-Zyklus signalisieren plötzliche Längenänderungen die martensitische und die austenitische Umwandlung. Martensit- und Austenit-Temperatur nehmen mit zunehmendem C-Gehalt ab. Dies stimmt mit dem experimentellen Befund überein, dass C die dicht-gepackten Phase stabilisiert. Die Martensit-Temperatur ist höher und die Austenit-Temperatur ist niedriger als in Bulk Fe-C Legierungen (Kapital 8). Mit zunehmendem Drahtdurchmesser neigen die Umwandlungstemperaturen zu ihren Bulkwerten. Bei nicht zu dünnen Drähten startet die Umwandlung von der Oberfläche und wandelt den Draht schnell um. Bcc und fcc Phasen folgen der K-S Orientierungsbeziehung. Bei ultradünnen Drächten (Durchmesser ≤ 2.8 nm) verläuft die austenitische Umwandlung in der axialen Richtung und der Draht transformiert sich zu einer nanokristallinen Bambus-Struktur von hcp und fcc Phasen. In Folge verformt der Draht. Nach Abkühlung übernimmt der Draht (fast) seine ursprüngliche Form (Formgedächtnis). Unter hoher axialer Zugspannung läuft die austenitische Umwandlung immer noch ab. Jedoch ist die martensitische Umwandlung teilweise unterdrückt. Dies führt zur starken plastischen Verformung. Unter den höchsten

Belastungen transformiert sich die austenitische Phase nur zum Teil zurück, während die kristallinen Phasen im Draht reorientiren und der mehrphasige Mischung eine hohe Zugfestigkeit geben.

A. Efficiency of the CNA detector

The thermal vibrations of the atoms are strong at high temperatures, so that the distance between atoms can be influenced dramatically. In this context, the common neighbor analysis (CNA) detector (Subsection 3.5.2) works inefficiently at such high temperatures, e.g., in Subsection 4.2.3 and 6.2.2 by studying the austenitic phase transition at 1300 K. In these cases, about 40 % of the atoms in the system can not be identified, see Fig. 4.10 and 6.15.

This problem can be solved partly by quenching of the system from high temperature. The quenching time must be selected with care. The atoms will be frozen by a too short quenching time and have no time to go back to their equilibrium positions. In contrast, a too long quenching time leads to phase transition. An example will be shown here.

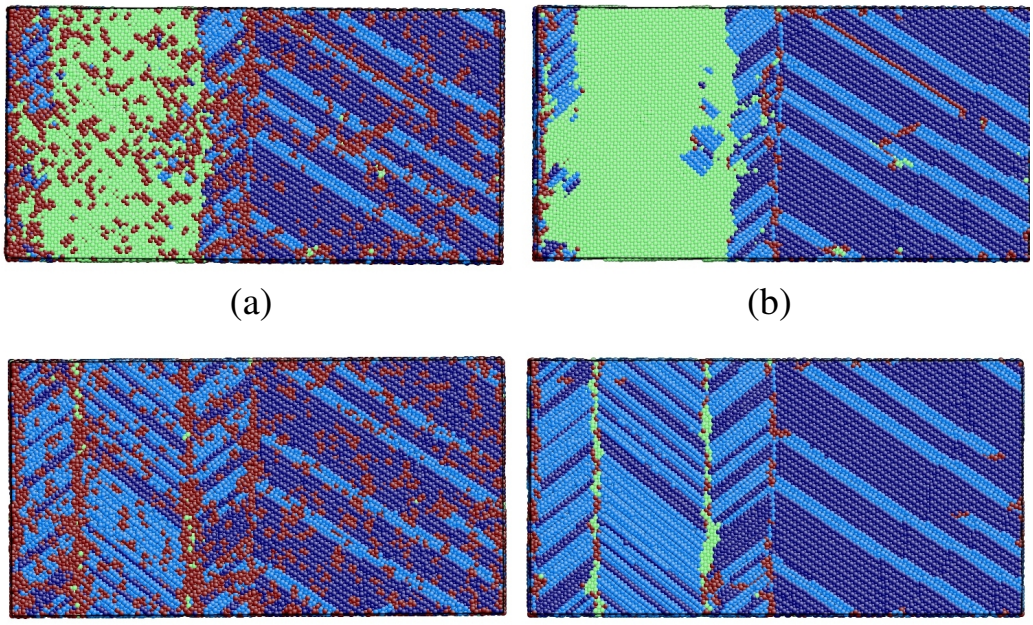

Figure A1: Snapshots of the ongoing austenitic phase transition at 1300 K. Two time steps are taken for the quenching. (a) and (b) status at 15 ps before/after the quenching. (c) and (d) status at 50 ps before/after the quenching. Colors denote the local crystal structure. Green: bcc; dark blue: fcc; light blue: hcp; red: unknown.

The system 3 (biphasic system with an fcc/bcc phase boundary, see Table 6.1) in Chapter 6 at a temperature of 1300 K is chosen for the quenching experiment. Two status at 15 ps (Fig. 6.8) and 50 ps during the ongoing transformation are taken. The quenching time is selected as 1 ps, i.e., the system temperature drops from 1300 K to 0 K in 1 ps.

Figure A1 displays the effect of quenching. Before quenching, a big amount of atoms cannot be identified by using the CNA detector at such a high temperature [red points in Fig. A1(a) and (c)]. After quenching, the most previously undetectable atoms can be identified well [Fig. A1(b) and (d)]. Although the quenching time has been selected carefully, a small amount of atoms at the twinning planes still transformed in the bcc phase. The fractional phase contents before and after the quenching are compared in Fig. A2.

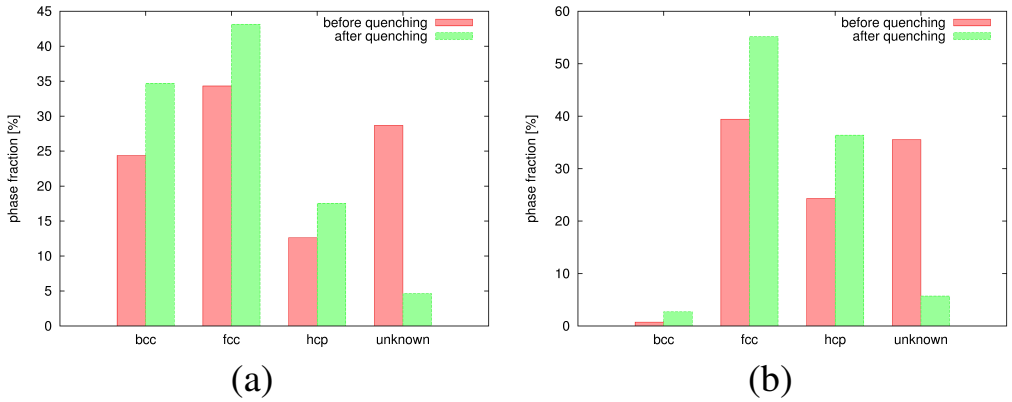

Figure A2: Fraction of each phase for two time steps during the austenitic phase transition at 1300 K before and after the quenching. (a) 15 ps (b) 50 ps.

B. Tables for the Meyer-Entel potential

The Meyer-Entel potential [31], which was used for calculations in this work, belongs to the EAM (embedded-atom-method) class, where the total energy is a sum of embedded energy and pair interaction, see Subsection 3.6.1. Note that the embedded energy is a function of electron density and the pair interaction is a function of effective charge.

Suitable approaches should be found for the numerical calculation for the embedded energy $F(\rho)$, the effect charge $Z(r)$ and the electron density $\rho^{at}(r)$. The atomic density at distance r (within the cutoff distance r_c) is given as follows

$$\rho^{at}(r) = N_{4s}|\psi_{4s}(r)|^2 + (N_v - N_{4s})|\psi_{3d}(r)|^2 - \rho_c \tag{C1}$$

where N_v is the total number of valence electrons, N_{4s} provides the relative s-d contributions. ρ_c is a constant defined in order to obtain continuity at the cutoff distance r_c. ψ_{4s} and ψ_{3d} are wave functions of the valence electrons. The parameters N_{4s}, N_v and r_c for the Meyer-Entel potential are given in Table B1.

	N_v	N_{4s}	r_c
Fe	8	0.57	8.332

Table B1: Parameters N_v, N_{4s} and r_c determining the electron density function ρ^{at} [31]. The cutoff distance r_c is given in units of Bohr radius a_B.

The calculation of the wave functions ψ was taken from Hartree-Fock calculation by Clementi and Roetti [72]. The wave function is given as follows

$$\psi(r) = \sum_i C_i \frac{(2\xi_i)^{n_i+1/2}}{\{4\pi(2n_i)!\}^{1/2}} r^{n_i-1} exp(-\xi_i r) \tag{B2}$$

The values of parameter n_i, ξ_i and C_i are listed in table B2.

i	n_i	ξ_i	C_i
4s			
1	1	27.03350	-0.00392
2	1	19.01040	-0.03027
3	2	13.51700	-0.02829
4	2	10.13050	-0.15090
5	3	5.21660	-0.21377
6	3	3.47616	-0.05096
7	4	1.92517	0.50156
8	4	1.07742	0.60709
3d			
1	3	6.06828	0.40379
2	3	2.61836	0.71984

Table B2: Parameters n_i, ξ_i and C_i determining the wave function ψ [72]. The values of ξ_i are given in units of a_B^{-1}.

The table B3 shows the parameters used for calculation of the embedding function $F(\rho)$ and pair potential function $\Phi(r)$ (equations 3.7-3.10) by using cubic splines.

ρ/ρ_0	F_{Fe}	F''_{Fe}	r/a_0	Z_{Fe}	Z''_{Fe}
0.0	0.0	0.0	0.0	26.0	0.0
0.5	-0.2823		0.7	1.4403	
1.0	-0.4276		0.87	0.2452	
2.0	-0.3030		0.94	0.1491	
2.3	0.0	0.0	1.0	0.0734	
			1.20	0.0	0.0

Table B3: Parameters determining the embedding function $F(\rho)$ and pair potential function $\Phi(r)$ [31]. The energies are given in units of R_y with $1R_y$ = 13.6054 eV, the effective charges Z in e^{-1}. The average electron density ρ_0 amounts to 2.776 $\cdot 10^{-3} a_B^{-3}$ and equilibrium lattice constant $a_0 = 5.42 a_B$.

Bibliography

[1] D. A. Porter and K. E. Easterling, *Phase Transformations in Metals and Alloys* (Chapman & Hall, London, 1992), 2nd ed.

[2] W. Pepperhoff and M. Acet, *Constitution and Magnetism of Iron and its Alloys* (Springer, Berlin, 2001).

[3] E. Pereloma and D. V. Edmonds, editors, *Phase Transformations in Steels*, vol. 2: Diffusionless Transformations, High Strength Steels, Modelling and Advanced Analytical Techniques (Woodhead Publishing Limited, Cambridge, UK, 2012).

[4] P. E. Blöchl, C. Joachim and A. J. Fisher, editors, *Computations for the Nano-Scale*, vol. 240 of *NATO ASI Series E* (Kluwer Academic Press, Dordrecht, 1993).

[5] P. M. Duxbury and T. J. Pence, editors, *Dynamics of Crystal Surfaces and Interfaces* (Plenum Publishing Corporation, New York, 1997).

[6] J. A. Venables, *Introduction to Surface and Thin Film Processes* (Cambridge University Press, Cambridge, 2000).

[7] L. B. Freund and S. Suresh, *Thin Film Materials: Stress, Defect Formation and Surface Evolution* (Cambridge University Press, Cambridge, 2003).

[8] Q. Mei and K. Lu, Prog. Mater. Sci. **52**, 1175 (2007).

[9] P. Tian, Annu. Rep. Prog. Chem., Sect. C **104**, 142 (2008).

[10] S. Tateyama, Y. Shibuta and T. Suzuki, Scripta Mater. **59**, 971 (2008).

[11] C. W. Sinclair and R. G. Hoagland, Acta Mater. **56**, 4160 (2008).

[12] Z. Q. Qiu, J. Pearson and S. D. Bader, Phys. Rev. Lett. **67**, 1646 (1991).

[13] W. Dürr, M. Taborelli, O. Paul, R. Germar, W. Gudat, D. Pescia and M. Landolt, Phys. Rev. Lett. **62**, 206 (1989).

[14] K. Kadau, R. Meyer and P. Entel, Surf. Rev. Lett. **6**, 35 (1999).

[15] K. Kadau and P. Entel, J. Magn. Magn. Mater. **198-199**, 531 (1999).

[16] P. Entel, M. Kreth, R. Meyer and K. Kadau, in *Modeling and Simulating Materials Nanoworld*, edited by P. Vincenzini and F. Zerbetto (Techna Group, Faenza, Italy, 2004), vol. 44 of *Advances in Science and Technology*, p. 101.

[17] L. Sandoval and H. M. Urbassek, Nano Lett. **9**, 2290 (2009).

[18] L. Sandoval and H. M. Urbassek, Nanotechnology **20**, 325704 (2009).

[19] L. Sandoval and H. M. Urbassek, Appl. Phys. Lett. **95**, 191909 (2009).

[20] J. J. Blackstock and G. J. Ackland, Philos. Mag. A **81**, 2127 (2001).

[21] K. Kadau, P. Entel and P. S. Lomdahl, Comput. Phys. Commun. **147**, 126 (2002).

[22] L. E. Kar'kina, I. N. Kar'kin and Y. N. Gornostyrev, Phys. Met. Metallogr. **101**, 130 (2006).

[23] K. F. Laneri, J. Desimoni, G. J. Zarragoicoechea and A. Fernández-Guillermet, Phys. Rev. B **66**, 134201 (2002).

[24] N. N. Rammo and O. G. Abdulah, J. Alloys Compounds **420**, 117 (2006).

[25] M. Ruda, D. Farkas and G. Garcia, Comput. Mater. Sci. **45**, 550 (2009).

[26] D. E. Jiang and E. A. Carter, Phys. Rev. B **67**, 214103 (2003).

[27] D. E. Jiang and E. A. Carter, Phys. Rev. B **71**, 045402 (2005).

[28] C. S. Becquart, J. M. Raulot, G. Bencteux, C. Domain, M. Perez, S. Garruchet and H. Nguyen, Comput. Mater. Sci. **40**, 119 (2007).

[29] A. Ishii, S. Ogata, H. Kimizuka and J. Li, Phys. Rev. B **85**, 064303 (2012).

[30] N. Gunkelmann, H. Ledbetter and H. M. Urbassek, Acta Mater. **60**, 4901 (2012).

[31] R. Meyer and P. Entel, Phys. Rev. B **57**, 5140 (1998).

[32] Z. Nishiyama, Sci. Rep. Tohoku Imp. Univ. **23**, 637 (1934).

[33] G. Wassermann, Arch. Eisenhüttenwes. **6**, 347 (1933).

[34] G. V. Kurdjumov and G. Sachs, Z. Phys. **64**, 325 (1930).

[35] http://www.geo.arizona.edu/xtal/geos306/fall09-12.htm.

[36] I. A. Ovid'ko, Rev. Adv. Mater. Sci. **1**, 61 (2000).

[37] J. M. Howe, *Interface in Materials: Atomic Structure, Thermodynamics and Kinetics of Solid-Vapor, Solid-Liquid and Solid-Solid Interfaces* (Wiley, New York, 1997).

[38] L. Sandoval, H. M. Urbassek and P. Entel, New J. Phys. **11**, 103027 (2009).

[39] E. C. Bain, Trans. AIME **70**, 25 (1924).

[40] H. K. D. H. Bhadeshia and R. W. K. Honeycombe, *Steels, Microstructure and Properties* (Elsevier, London, 2006), 3rd ed.

[41] T. Fukino and S. Tsurekawa, Materials Transactions **49**, 2770 (2008).

[42] L. Verlet, Phys. Rev. **159**, 98 (1967).

[43] M. P. Allen and D. J. Tildesley, *Computer Simulation of Liquids* (Oxford University Press, New York, 1987), 1st ed.

[44] J. M. Haile, *Molecular Dynamics Simulation: Elementary Methods* (Wiley, New York, 1997), 1st ed.

[45] H. J. C. Berendsen, J. P. M. Postma, W. F. van Gunsteren, A. Dinola and J. R. Haak, J. Chem. Phys. **81**, 3684 (1984).

[46] H. C. Andersen, J. Chem. Phys. **72**, 2384 (1980).

[47] S. Nosé, J. Chem. Phys. **81**, 511 (1984).

[48] W. G. Hoover, Phys. Rev. A **31**, 1695 (1985).

[49] C. L. Kelchner, S. J. Plimpton and J. C. Hamilton, Phys. Rev. B **58**, 11085 (1998).

[50] V. Dupont and F. Sansoz, in *Trends in Computational Nanomechanics*, edited by T. Dumitrica and J. Leszczynski (Springer, Netherlands, 2010), vol. 9 of *Challenges and advances in computational chemistry and physics*, p. 160.

[51] J. D. Honeycutt and H. C. Andersen, J. Phys. Chem. **91**, 4950 (1987).

[52] D. Faken and H. Jonsson, Comput. Mater. Sci. **2**, 279 (1994).

[53] A. Stukowski, Modelling Simul. Mater. Sci. Eng. **20**, 045021 (2012).

[54] M. S. Daw and M. I. Baskes, Phys. Rev. Lett. **50**, 1285 (1983).

[55] M. S. Daw and M. I. Baskes, Phys. Rev. B **29**, 6443 (1984).

[56] C. Engin, L. Sandoval and H. M. Urbassek, Model. Simul. Mater. Sci. Eng. **16**, 035005 (2008).

[57] M. W. Finnis and J. E. Sinclair, Philos. Mag. A **50**, 45 (1984), Erratum: **53** (1986) 161.

[58] U. Fano and J. A. Stephens, Phys. Rev. B **34**, 438 (1986).

[59] R. A. Johnson and D. J. Oh, J. Mater. Res. **4**, 1195 (1989).

[60] Z. Yang and R. A. Johnson, Model. Simul. Mater. Sci. Eng. **1**, 707 (1993).

[61] M. Müller, P. Erhart and K. Albe, J. Phys.: Condens. Matter **19**, 326220 (2007).

[62] T. Lee, M. I. Baskes, S. M. Valone and J. D. Doll, J. Phys.: Condens. Matter **24**, 225404 (2012).

[63] R. J. Weiss and K. J. Tauer, Phys. Rev. **102**, 1490 (1956).

[64] W. Bendick and W. Pepperhoff, Acta. Metall. **30**, 679 (1982).

[65] H. Hasegawa and D. G. Pettifor, Phys. Rev. Lett. **50**, 130 (1983).

[66] A. P. Sutton, *Electronic Structure of Materials* (Clarendon Press, London, 1993).

[67] D. Pettifor, *Bonding and Structure of Moleculaes and Solids* (Clarendon Press, Oxford, 1995).

[68] M. Finnis, *Interatomic Forces in Condensed Matter* (Oxford University Press, Oxford, 2003).

[69] L. Sandoval, H. M. Urbassek and P. Entel, Phys. Rev. B **80**, 214108 (2009).

[70] P. Entel, R. Meyer, K. Kadau, H. C. Herper and E. Hoffmann, Eur. Phys. J. B **5**, 379 (1998).

[71] P. Entel, R. Meyer and K. Kadau, Philos. Mag. B **80**, 183 (2000).

[72] E. Clementi and C. Roetti, Data Nucl. Data Tables **14**, 167 (1974).

[73] R. A. Johnson, J. G. Dienes and A. C. Damask, Acta Metall. **12**, 1215 (1964).

[74] V. Rosato, Acta Mater. **37**, 2759 (1989).

[75] R. A. Rosato, M. Guillope and B. Legrand, Philos. Mag. A **59**, 321 (1989).

[76] D. J. Hepburn and G. J. Ackland, J. Phys. Rev. B **78**, 165115 (2008).

[77] S. Garruchet and M. Perez, Comput. Mater. Sci. **43**, 286 (2008).

[78] E. Clouet, S. Garruchet, H. Nguyen, M. Perez and C. S. Becquart, Acta. Mater. **56**, 3450 (2008).

[79] D. Terentyev, N. Anento, A. Serra, V. Jansson, H. Khater and G. J. Bonny, Nucl. Mater. **408**, 272 (2011).

[80] C. W. Sinclair, M. Perez, R. G. A. Veiga and A. Weck, Phy. Rev. B **81**, 224204 (2010).

[81] R. G. A. Veiga, M. Perez, C. S. Becquart, C. Domain and S. Garruchet, Phy. Rev. B **82**, 054103 (2010).

[82] R. G. A. Veiga, M. Perez, C. S. Becquart, E. Clouet and C. Domain, Acta. Mater. **59**, 6963 (2011).

[83] C. Bos, J. Sietsma and B. J. Thijsse, Phys. Rev. B **73**, 104117 (2006).

[84] H. Song and J. J. Hoyt, Acta Mater. **60**, 4328 (2012).

[85] S. Plimpton, J. Comp. Phys. **117**, 1 (1995). http://lammps.sandia.gov/.

[86] J. M. Rigsbee and H. I. Aaronson, Acta Metall. **27**, 365 (1979).

[87] M. J. Demkowicz, R. G. Hoagland and J. P. Hirth, Phys. Rev. Lett. **100**, 136102 (2008).

[88] A. Hashibon, C. Elsässer, Y. Mishin and P. Gumbsch, Phys. Rev. B **76**, 245434 (2007).

[89] L. Liu, K. D. Kafui and C. Thornton, Powder Technology **199**, 189 (2010).

[90] L. E. Murr, *Interfacial Phenomena in Metals and Alloys* (Addison-Wesley, Reading, MA, 1975).

[91] M.J. Spencer, A. Hung, I. K. Snook and I. Yarovsky, Surf. Sci. **513**, 289 (2002).

[92] W. R. Tyson and W. A. Miller, Surf. Sci. **62**, 267 (1977).

[93] M. A. Miller and W. P. Reinhardt, J. Chem. Phys. **113**, 7035 (2000).

[94] K. A. Jackson and B. Chalmers, Can. J. Phys. **34**, 473 (1956).

[95] J. W. Christian, *The Theory of Transformation in Metals and Alloys* (Pergamon Press, Oxford, 2002).

[96] C. Engin and H. M. Urbassek, Comput. Mater. Sci. **41**, 297 (2008).

[97] S. Tateyama, Y. Shibuta, T. Kumagai and T. Suzuki, ISIJ Int. **51**, 1710 (2011).

[98] M. Hillert and L. Höglund, Scr. Mater. **54**, 1259 (2006).

[99] G. B. Olson and M. Azrin, Metall. Trans. A **9A**, 713 (1978).

[100] G. B. Olson and M. Cohen, Metall. Trans. A **13A**, 1907 (1982).

[101] T.-H. Ahn, C.-S. Oh, D. H. Kim, K. H. Oh, H. Bei, E. P. George and H. N. Han, Scr. Mater. **63**, 540 (2010).

[102] S. Zaefferer, J. Ohlert and W. Bleck, Acta Mater. **52**, 2765 (2004).

[103] W. J. Dan, S. H. Li, W. G. Zhang and Z. Q. Lin, Mater. Des. **29**, 604 (2008).

[104] M. Biglari and E. J. Mittemeijer, Model. Simul. Mater. Sci. Eng. **20**, 075010 (2012).

[105] D. Z. Liu, T. Kikuchi, S. Kajiwara and N. Shinya, J. Intel. Mater. Syst. Struct. **10**, 569 (1999).

[106] G. D. Sandrock and R. F. Hehemann, **4**, 451 (1971).

[107] W. G. Burgers, Physica **1**, 561 (1934).

[108] C. J. Huang and D. J. Browne, Metall. Mater. Trans. A **37**, 539 (2006).

[109] E. A. Jäger and E. J. Mittemeijer, Acta Mater. **59**, 5775 (2011).

[110] E. A. Jäger and E. J. Mittemeijer, Int. J. Mat. Res. (formerly Z. Metallk.) **102**, 837 (2011).

[111] F. M. Wang and R. Ingalls, Phys. Rev. B **57**, 5647 (1998).

[112] H. Kato, Y. Liang and M. Taya, Scr. Mater. **46**, 471 (2002).

[113] Y. Ivanisenko, W. Lojkowski and H.-J. Fecht, Materials Science Forum **539-543**, 4681 (2007).

[114] F. Willaime and C. Massobrio, Phys. Rev. Lett. **63**, 2244 (1989).

[115] M. Ekman, B. Sadigh, K. Einarsdotter and P. Blaha, Phys. Rev. B **58**, 5296 (1998).

[116] H. Djohari, F. Milstein and D. Maroudas, Phys. Rev. B **79**, 174109 (2009).

[117] D. A. Hardwick, Thin Solid Films **154**, 109 (1987).

[118] R. P. Vinci and J. J. Vlassak, Annu. Rev. Mater. Sci. **26**, 431 (1996).

[119] W. Brückner, W. Pitschke, J. Thomas and G. Leitner, J. Appl. Phys. **87**, 2219 (2000).

[120] B. R. Cuenya, M. Doi, S. Löbus, R. Courths and W. Keune, Surf. Sci. **493**, 338 (2001).

[121] Y. Ma, A. Setzer, J. W. Gerlach, F. Frost, P. Esquinazi and S. G. Mayr, Adv. Funct. Mater. **22**, 2529 (2012).

[122] J. Ko, T. Bae and J. Hong, J. Appl. Phys. **112**, 113919 (2012).

[123] T. Edler, S. Hamann, A. Ludwig and S. G. Mayr, Scr. Mater. **64**, 89 (2011).

[124] J. Buschbeck, I. Opahle, M. Richter, U. K. Rößler, P. Klaer, M. Kallmayer, H. J. Elmers, G. Jakob, L. Schultz and S. Fähler, Phys. Rev. Lett. **103**, 216101 (2009).

[125] G. Golan, A. Axelevitch, B. Sigalov and B. Gorenstein, Microelectr. J. **34**, 255 (2003).

[126] J. Y. Suh, R. Lopez, L. C. Feldman and R. F. Haglund, J. Appl. Phys. **96**, 1209 (2004).

[127] W. Liang, M. Zhou and F. Ke, Nano Lett. **5**, 2039 (2005).

[128] H. S. Park, K. Gall and J. A. Zimmerman, Phys. Rev. Lett. **95**, 255504 (2005).

[129] C. Zener, *Elasticity and Anelasticity of Metals* (U. Chicago, Chicago, 1948), pp. 16ff.

[130] J. Tersoff, Phy. Rev. B **39**, 5566 (1989).

[131] T. Krenke, M. Acet, E. F. Wassermann, X. Moya, L. Mañosa and A. Planes, Phys. Rev. B **72**, 014412 (2005).

[132] N. P. Lazarev, C. Abromeit, R. Schäublin and R. Gotthardt, J. Appl. Phys. **100**, 63520 (2006).

[133] V. G. Sathe, S. Banik, A. Dubey, S. R. Barman, A. M. Awasthi and L. Olivi, Adv. Mater. Res. **52**, 175 (2008).

[134] G. Krauss, *Principles of Heat Treatment of Steel* (American Society for Metals, Metals Park, Ohio, 1980).

[135] E. Sak-Saracino and H. M. Urbassek (2013), in preparation.

[136] J. L. Dossett and H. E. Boyer, *Practical Heating Treating* (ASM International, Materials Park, OH, USA, 2006), 2nd ed.

[137] W. Liang and M. Zhou, Phy. Rev. B **73**, 115409 (2006).

[138] C. Ji and H. S. Park, Nanotechnology **18**, 305704 (2007).

[139] H. S. Park, Nano Lett. **6**, 958 (2006).

[140] F. Ma and K. W. Xu, J. Mater. Res. **22**, 1299 (2007).

[141] F. Ma, K. W. Xu and P. K. Chu, Mater. Sci. Eng. R (2013).

Publications

List of Publications

(1) B. Wang and H. M. Urbassek: *Phase transitions in an Fe system containing a bcc/fcc phase boundary: An atomistic study*, Phys. Rev. B **87**, 104108 (2013). http://link.aps.org/doi/10.1103/PhysRevB.87.104108

(2) B. Wang and H. M. Urbassek: *Molecular dynamics study of the $\alpha-\gamma$ phase transition in Fe induced by shear deformation*, Acta Mater. **61(16)**, 5979 (2013). http://dx.doi.org/10.1016/j.actamat.2013.05.045

(3) B. Wang and H. M. Urbassek: *Atomistic dynamics of the bcc $\leftrightarrow$ fcc phase transition in iron: competition of homo- and heterogeneous phase growth*, Comput. Mater. Sci. **81**, 170 (2014). http://dx.doi.org/10.1016/j.commatsci.2013.08.005

(4) B. Wang and H. M. Urbassek: *Computer simulation of strain-induced phase transformations in thin Fe films*, Modelling Simul. Mater. Sci. Eng. **21**, 085007, (2013). http://iopscience.iop.org/0965-0393/21/8/085007/

(5) B. Wang, E. Sak-Saracino, N. Gunkelmann and H. M. Urbassek: *Molecular-dynamics study of the $\alpha \leftrightarrow \gamma$ phase transition in Fe-C*, Comp. Mater. Sci. **82**, 399 (2014) http://www.sciencedirect.com/science/article/pii/S0927025613006162

(6) B. Wang, E. Sak-Saracino, L. Sandoval and H. M. Urbassek: *Martensitic and austenitic phase transformations in Fe-C nanowires: a molecular-dynamics approach* (submitted to Modelling Simul. Mater. Sci. Eng.).

(7) R. Schmitt, B. Wang, H. M. Urbassek, R. Müller: *Modeling of martensitic transformations in pure iron by a phase field approach using information from atomistic simulation*, Technische Mechanik **33(2)**, 119-130 (2013).

Conferences

(1) Workshop, DFG-Graduiertenkolleg 814, Noverber, 2010, Waldfischbach, Germany

(2) Final colloquium, DFG-Graduiertenkolleg 814, April, 2012, Kaiserslautern, Germany

(3) International Conference on multiscale materials modelling, October, 2012, Singapore

Curriculum Vitae

Education background

2009	Diplom Ing., Material Science, university of Stuttgart, Germany
	Diplom thesis: Einbau von Zn^{2+} in Calcit durch Grünalgen
2005	Vordiplom, Material Science, university of Stuttgart, Germany
2002	German language course, University of Stuttgart, Germany
2001	Bachelor, Material Science and Engineer, University of Shanghai, China
	Bachelor thesis: Heat treatment of steel for cold extrusion

Scientific experience

November, 2009 - March, 2012:	Member of the DFG-Graduiertenkolleg 814
April, 2012 - present:	Member of the SFB 926

Working experience

· different kinds of student part time jobs during the studying in the university of Stuttgart

· Hiwi-job for Max-Planck-Institut für Metallforschung in Stuttgart

Research interests

· material science

· molecular modeling